AN ABSTRACT OF THE THESIS OF

Vassilis A. Zervakis for the degree of Doctor of Philosophy in Oceanography presented on November 18, 1993 .

Title : On the Propagation of Near-Inertial Motion from the Oceanic Mixed Layer.

Redacted for Privacy

Abstract approved : _____
Murray D. Levine

The radiation of wind-generated inertial currents from the mixed-layer in the form of near-inertial internal waves is the subject of this study. Particular attention is paid to the time scales characteristic of the energy exchange between mixed-layer and pycnocline. For this purpose, a three-dimensional, β-plane, linear model is developed. The numerical results are interpreted using analytical tools. The model is initialized by mixed-layer inertial oscillations set by a propagating atmospheric front. We demonstrate the importance of the propagation direction of the front in determining the decay of the mixed-layer inertial currents. The exchange of energy between mixed-layer and pycnocline is found to be due to modal interference and modal departure.

The model is assessed by comparison to observations of near-inertial oscillations from the OCEAN-STORMS experiment. A slab mixed-layer model, forced by a local wind time-series, is used to isolate three events of local generation for detailed analysis. The transfer of energy from the mixed-layer to the pycnocline occurs approximately at times predicted by analytical theory. However, while the observed waves propagate vertically as "beams", the modeled waves remain at the top of the pycnocline. The frequency of the modeled currents is similar to the observed, ranging from slightly subinertial to $1.05\,f$ with the phase propagating upwards.

Assuming linear dynamics we develop a time-dependent body friction coefficient simulating the loss of mixed-layer inertial energy to near-inertial internal gravity waves, for use in the traditional slab mixed-layer model. The new decay coefficient is a function of latitude, stratification, and horizontal wavenumber of forcing. Comparison of the slab model results with OCEAN-STORMS observations reveals a better agreement using the new parameterization, than the traditional method. This result suggests that the dominant sink of mixed-layer inertial energy during the experiment was inertial pumping, and that the horizontal scales of the forcing were large.

On the Propagation of Near-Inertial Motion from the Oceanic Mixed Layer

by

Vassilis A . Zervakis

A THESIS

submitted to

Oregon State University

in partial fulfillment of the
requirements for the
degree of

Doctor of Philosophy

Completed November 18, 1993

Commencement June 1994

APPROVED:

Redacted for Privacy

Associate Professor of Oceanography in charge of major

Redacted for Privacy

Dean of College of Oceanic and Atmospheric Sciences

Redacted for Privacy

Dean of Graduate School

Date thesis is presented November 18, 1993

Typed by researcher for Vassilis A. Zervakis

To my family

ACKNOWLEDGEMENTS

First and above all I need to express my special thanks to Murray Levine. For his solid support, sincere care and encouragement through six years I am grateful. This thesis is the final product of his tactful skepticism and questioning of my results, his patience with my inexperience and his investment of time and personal labor to account for my shortcomings. I consider this treatise as much his "child" as mine. I hope to have learned more than just fluid dynamics from him.

Many thanks to Bob Higdon; going to his lectures was always a pleasure to me (as well as to the rest of the audience...), and the discussions we had were very helpful in formulating the numerical part of the thesis. I also would like to thank Clayton Paulson, for graciously making his data available to me. Clayton, as well as Roland deSzoeke amd Jim Moum have always been readily available sources of advice and support. Their comments were critical in giving this work its final shape. Finally, I wish to thank André Weideman for being so helpful with the committee dealings.

Bob Miller and Leonard Walstad advised me on assessing the numerical methods; comments by Rien Chieh Lien on the first manuscript were very appreciated. I need to thank Steve Gard for his stalwart support: for six years he has been my genie: whenever a problem of technical nature emerged, I only had to rub the lantern, and Steve was there, with his tools and his eagerness to swear at my computer!

Andaeus was a mythical giant that had to fight with Hercules. Every time he was thrown to the ground by his opponent, he drew up new powers from the soil of his land. I need to thank my family in Greece for playing the role of the earth in my fight with my own weaknesses. Their patience and their humour in redefining the meaning of the word *soon* have helped me keep up my good spirits (sometimes they had to send me good 'spirits' too). I'm also grateful to the U.S. branch of my family, Fotini Zervaki and Yannis Kevrekidis, for their day-to-day support and encouragement. Visiting them has always been a very heart-warming experience and helped me to continue.

George Spanos and Dimitris Gerasopoulos initially, and later Elina Dretta and Vaggelis Metaxides gave me shots of my own culture and language whenever I needed them. That was more common at the beginning, less later, as it was very easy to get integrated and feel as a native in hospitable Corvallis.

Living for six years in such a small community one gets to know many people, and quite well. I hope the friendships I made in Corvallis will last over the large space that will separate us from now on. I have always felt very comfortable with Hemantha Wijesekera's friendship. It has been puzzling me how someone specialized in turbulence can radiate so much stability and reason, valuable to me at many times. I thoroughly enjoyed our evenings of tea and "I, Claudius". The company of Andy Juhl and Christopher Krembs has always been delightful and educating. The three musketeers, Marcelino Suzuki, Maurice McCarthy and Luca Tallini have been a fountain of animated discussions, not always so well founded but entertaining arguments, and a lot of multicultural excitement in my life. They also prepared the most memorable birthday dinner I ever had! Fred Bahr, Alberto Mestas-Nuñez, Ed Zaron, Julie McClean, Rodrigo Nuñez, Robin Tokmakian and Jorge Mesias have been good friends and companions throughout the various ups and downs of graduate student life. Many thanks to June Wilson, Ann Morey and Lawrie Padman for their company in Corvallis, and to Mike Neeley-Brown, Chaojiao Sun, Mary-Elena Carr, Pat Collier and Ed Llewellyn for their company on board the good ship WECOMA. Lately, Dylan Righi, Diana Greenslade and Kieran O'Driscoll have joined this list. Diana's violin and Kieran's voice have given me great pleasure at times when I did not need much more.

Discoursing with Irja Galvan over innumerable lunches has been a stimulant for my reflexes and an exercise in my English language skills (well, at least you tried, Irja!); her company has been a pleasure — most of the time! Jeff, Jaqueline and Jan Connor, have been good friends for long. The friends who comforted me through my first months in Corvallis should not be left out: Jim Sisley, Pern Vanapruk, Lek Choksombasay, and Julio Rodiño.

Lastly, I feel grateful to Susanne Szentandrasi, for offering me her valuable friendship, company and support through the last stages of completing this thesis.

That every body perseveres in its state of resting, or of moving uniformly in a right line, as far as it is not compelled to change that state by external forces impressed upon it.

Isaac Newton, 1776

TABLE OF CONTENTS

LIST OF FIGURES

LIST OF FIGURES (continued)

LIST OF FIGURES (continued)

LIST OF TABLES

ON THE PROPAGATION OF NEAR-INERTIAL MOTION FROM THE OCEANIC MIXED LAYER

I. GENERAL INTRODUCTION

This work is not a product of independent thinking. It all started when Isaac Newton restated what Galileo had first discovered, the *principle of inertia*: "*That every body perseveres in its state of resting, or of moving uniformly in a right line, as far as it is not compelled to change that state by external forces impressed upon it*" (Newton, 1776). If the above-mentioned object is a piece of ocean, an observer bound on the rotating surface of the Earth will describe the water's motion as circular, completing two rotations within one period of his own motion. Motions of water of this kind are commonly observed by oceanographers and have been baptized *near-inertial motions*, or *near-inertial oscillations*.

Current measurements in the surface mixed layer of the ocean very often reveal the presence of near-inertial oscillations: rotary currents on the horizontal plane, with frequency very near the local inertial frequency f (where f = sin(latitude) / 12 hours). Their magnitudes are very intermittent; however, they often persist for several inertial cycles. Mixed-layer inertial currents have been commonly observed to occur after the passage of atmospheric fronts (Day and Webster, 1965; Saelen, 1963; Hunkins, 1967), with coherence scales of tens of kilometers in the horizontal direction (Webster, 1968; Gonella, 1972).

Near inertial currents have also been observed in the pycnocline and the deeper ocean, propagating as internal waves. Measurements from the upper ocean often reveal upward phase propagation, suggesting downward propagation of energy (Leaman, 1975; Leaman and Sanford, 1975; Sanford, 1975; D'Asaro, 1984). The waves' horizontal scales are tens of kilometers; the vertical coherence is only tens of meters (Webster, 1968; Fu, 1981).

The interest of the scientific community in mixed layer and pycnocline near-inertial currents is well justified: they may play an important role in the energy balance of the ocean, transferring energy from the atmosphere to the internal wave continuum. D'Asaro (1985), assuming generation by the wind, estimated an annual average energy flux of 1.4 mW m^{-2} to mixed-layer inertial oscillations, a significant part of the 7 mW m^{-2} of dissipation it would

take to damp the global internal wave field in a week (Garrett and Munk, 1979; Munk, 1981). Inertial currents may play an important role in mixing and the erosion of a pycnocline, as low Richardson numbers and high vertical shears associated with their high vertical wavenumbers have been reported by observations and models (D'Asaro, 1985b; Marmorino et al., 1987; Eriksen, 1991; Krauss, 1981). As to the role inertial waves play in the internal wave energy balance, there is evidence from a number of modeling efforts that the high frequencies tend to extract energy from the near-inertial field (Flatté et al., 1986; Henyey et al., 1986; Broutman et al., 1986)

Numerous modeling efforts have been used to understand the generation (Pollard and Millard, 1970; Paduan et al., 1989) and propagation in the open ocean (Anderson and Gill, 1983; Pollard, 1970; Gill, 1984; Rubenstein, 1983; Price, 1983; Greatbatch, 1983, 1984; Kundu and Thompson, 1985; Kundu, 1986; Shay and Elsberry, 1987; Shay et al., 1989). There was a leap in the understanding of the wave-field evolution when D'Asaro (1989) showed the importance of the variation of the Coriolis parameter f with latitude on the radiation of near-inertial kinetic energy downwards from the mixed-layer (*inertial pumping*).

The purpose of this study is to improve the understanding of the characteristics of near-inertial wave evolution. For that reason, we improve existing numerical models, assess the models using observations collected during the OCEAN-STORMS experiment, and use linear wave theory to analyze and describe the observations and the model results. Special attention is paid to the rates of energy exchange between the mixed-layer and the pycnocline, as the waves propagate downward.

The thesis is structured into three distinct (but closely related) parts:

In Chapter II, titled "Near Inertial Energy Exchange between the Mixed-Layer and Pycnocline", we develop a semi-spectral numerical model describing the propagation of near-inertial waves generated by the propagation of an idealized atmospheric front over the β-plane. Also, we develop an analytical tool for making predictions about the characteristic time-scales of the wavefield's evolution based on the initial mixed-layer inertial horizontal structure and the oceanic background conditions. Finally, we introduce criteria that have to be met in order to use a two-dimensional model to approximate the evolution of a near-inertial wavefield.

In Chapter III, titled "Near Inertial Wave Propagation into the Pycnocline during OCEAN STORMS: Observations and Model Comparison", we analyze data collected during the OCEAN-STORMS experiment, and compare them with results from the model developed in chapter II. Wind-speed measurements were used to isolate events of local generation of near-inertial currents. Three major events are isolated, analyzed, and compared with corresponding model runs.

In Chapter IV, titled "Parameterizing the Decay of Mixed-Layer Inertial Oscillations generated by the Wind: A Modification of the Slab Model", we use conclusions drawn from chapter II to modify the slab model (Pollard and Millard, 1970). The constant body-friction coefficient used in the model to dissipate kinetic energy is replaced by a time-dependent coefficient, so that the rate of decay of mixed-layer kinetic energy is consistent with inertial pumping theory.

All the above chapters are composed as manuscripts and are being submitted for publication. My major professor, Dr. Murray Levine, is co-author in all of them.

II. NEAR-INERTIAL ENERGY EXCHANGE BETWEEN THE MIXED-LAYER AND PYCNOCLINE

II.1. Abstract

The radiation of wind-generated inertial currents away from the mixed-layer in the form of low-frequency internal gravity waves is the subject of this paper. Particular attention is paid to the energy exchange between the mixed-layer and the pycnocline, and the time-scales characteristic of the waves' evolution. For that purpose, a three-dimensional, β-plane, linear model is developed, making use of baroclinic modes to describe the velocity field. The numerical results are interpreted using analytical tools. The model is initialized by mixed-layer inertial oscillations set by a propagating atmospheric front. We demonstrate the importance of the propagation direction of the front in determining the decay of inertial currents from the mixed-layer. The exchange of energy between mixed-layer and pycnocline is found to be due to modal interference and modal departure. We analyze the effects of the initial structure of the mixed-layer as well as the background oceanic environment and make predictions about the wave field evolution at various latitudes.

II.2. Introduction

Near-inertial oscillations in the mixed layer are a commonly observed feature in the world's oceans. Nearly circular motions in a horizontal plane with a frequency near f (the local Coriolis parameter) are commonly observed after the passing of atmospheric fronts or hurricanes. Their generation has been quite successfully explained by simple models based on treating the mixed layer as a solid slab (e.g. Pollard and Millard, 1970; Kundu, 1976; D'Asaro, 1985; Paduan et al., 1989), where the velocity is uniform throughout the mixed layer. However, the decay of near-inertial energy in the mixed layer is not understood as well as the generation. Possible mechanisms responsible for the decrease in mixed-layer energy include turbulent dissipation and linear/nonlinear transfer of energy to the ocean below.

This paper focuses on the decay of mixed-layer near-inertial energy due to the radiation of linear, near-inertial waves. These internal gravity waves are generated by horizontal convergences and divergences in the mixed layer that force the fluid below--a process that is known as *inertial pumping*. Inertial pumping results from horizontal gradients in the mixed layer.

Theoretical considerations show that on an f-plane the horizontal gradients in the mixed layer are created by the nature of the wind stress forcing. Gill (1982) showed that a moving atmospheric front will generate inertial oscillations in its wake. The horizontal scale is a function of the speed of the front and its horizontal structure. A one-dimensional front moving at a speed C forces the mixed layer currents at a horizontal wavenumber of $\kappa = f/C$. Linear models developed by Pollard (1970) and Kundu (1985) used analytical forms of the wind stress and examined the internal waves created in the wake of the wind. Gill (1984) used another approach to force the waves; the model was solved as an initial-value problem. The mixed layer is initialized with inertial oscillations and the model tracks the subsequent wave propagation.

Other modeling efforts include models by Price (1983) (multi-layered in the vertical, hurricane scales), Rubenstein (1983) (multi-layered, eddy diffusivity and bottom porosity), Greatbatch (1983, 1984) (multi-level ocean, including non-linearities and entrainment), Kundu (1986) (vertical modes with eddy diffusivity), Shay and Elsberry (1987) (hurricane scales, use of vertical modes on a level or sloping bottom). In all cases, the models were two-dimensional and run on an *f*-plane. One common characteristic of the models is that the predicted time-scale for mixed-layer current decay agrees with observations at small horizontal scales (hurricanes), but not at large scales (atmospheric fronts and propagating storms). For large-scale forcing events the predicted decay time-scale is larger than observed.

D'Asaro (1989) demonstrated that the β-effect causes a reduction of horizontal scales in time, thus accelerating the rate of inertial pumping of energy out of the mixed-layer. He showed that the magnitude of the meridional wavenumber of the inertial currents will vary as $l = l_0 - \beta t$, where $l < 0$ denotes propagation to the south, and β is the rate of change of Coriolis parameter with latitude. As a result, the radiation of energy from the mixed layer increases the pycnocline horizontal kinetic energy (HKE) as t^6 compared with t^2 on an *f*-plane. Although some of the numerical experiments performed by Gill (1984) were on a β-plane, more attention was paid to the southward wave propagation than the significance of the effect of the waves on inertial pumping.

The purpose of this paper is to explore how the wind-generated energy radiates from the mixed layer by the vertical and horizontal propagation of near-inertial waves. Of particular interest is the time-scale of the decay of mixed layer energy and the magnitude of the energy transfers to the ocean below. Specifically we want to understand and quantify the energy transfer from the mixed layer as a function of the following initial conditions and background properties:

- initial horizontal wavenumber in the mixed layer (magnitude and direction),
- horizontal extent of the storm

- mixed layer depth (seasonal stratification), and
- deep stratification.

To study the radiation of energy from the mixed layer we use a linear, numerical model on a β-plane. The solution is analytical in depth using vertical modes and in x (zonal) using Fourier transforms; and numerical in y (meridional) and time. The results of the model are interpreted in terms of linear wave theory. This comparison of the numerical model with wave theory will permit us to use analytical expressions to predict the time scale and magnitude of the energy leaving the mixed layer as a function of the initial conditions and background properties. Hence the energy exchange between mixed layer and pycnocline can be described without having to run the numerical model.

We consider our analysis as revisiting the landmark study by Gill (1984; hereafter referred to as G84). As in G84, we distribute the inertial energy, initially concentrated within the mixed layer, into vertical modes, and then let the modes propagate horizontally as free waves. Phase-differences between the modes develop as each mode oscillates at a discrete frequency. The wavefield, which is the sum of all the modes, evolves from the initial condition and develops non-zero velocities below the mixed-layer. As a result, we have propagation of energy with depth. The horizontal propagation of each mode is treated numerically in the meridional direction and spectrally in the zonal.

The model in G84 has been modified in order to determine the effect of the initial conditions and background properties on the wave propagation. We have added the zonal dimension to the model and determined under what conditions this dimension is important. The initial condition of mixed-layer velocity has been altered to represent a velocity field consistent with a propagating front; the G84 initial conditions are not compatible with this forcing. The effect of different north-south extents of the forcing has been addressed explicitly in the numerical model.

The numerical model is presented in section 2. Linear wave dynamics are discussed in section 3 to provide a basis for interpreting the model results. The model results are shown in section 4 demonstrating the dependence of the decay time scale on the initial conditions and background properties; comparison is made with the behavior of analytical wave theory. A summary and conclusions are given in section 5.

II.3. Model Formulation

The model of near-inertial waves is patterned after the model developed by G84 with some important differences. The model is based on the momentum equations for a linear, inviscid, Boussinesq ocean given by:

$$\frac{\partial u}{\partial t} - fv = -\frac{\partial p}{\partial x} \tag{1}$$

$$\frac{\partial v}{\partial t} + fu = -\frac{\partial p}{\partial y} \tag{2}$$

$$0 = -\frac{\partial p}{\partial z} - g\frac{\rho'}{\rho_0} \tag{3}$$

where x, y, z denote the zonal, meridional and vertical axes, increasing to the north, east and upwards from the ocean bottom respectively; u, v, w are the components of the particle velocity in the x,y,z directions. f is the latitude-dependent Coriolis parameter, and the density has been decomposed into a constant ρ_0, a depth dependent component $\rho_1(z)$, and a perturbation density $\rho'(x,y,z,t)$. The pressure p has been normalized by ρ_0, consistent with G84. The hydrostatic approximation has been adopted in the vertical momentum balance. The ocean is assumed incompressible

$$\frac{\partial u}{\partial x} + \frac{\partial v}{\partial y} + \frac{\partial w}{\partial z} = 0 \tag{4}$$

and mass continuity is given by:

$$\frac{g}{\rho_0}\frac{\partial \rho'}{\partial t} - N^2 w = 0 \tag{5}$$

where N is the buoyancy frequency defined by $N^2 = -g/\rho_0(d\rho_1/dz)$, where g the acceleration of gravity.

Eliminating ρ' and w by substituting (3) and (5) into (4), we retrieve a system of three variables, u, v, p and three first order in time differential equations.

The initial condition of the model is assumed to be a current restricted in the mixed layer:

$$\begin{aligned} [u(x,y,z,t), v(x,y,z,t)]_{t=0} &= [u^i(x,y), v^i(x,y)]\, S(z) \\ [p(x,y,z,t)]_{t=0} &= p^i(x,y)\, S(z) \end{aligned} \tag{6}$$

where $S(z)$ is defined to limit the initial currents to the mixed layer :

$$S(z) \equiv \begin{cases} 1, & H - H_{mix} < z < H \\ 0, & 0 < z < H - H_{mix} \end{cases} \tag{7}$$

where H_{mix} is the mixed layer depth, $z = 0$ at the bottom of the ocean, and $z = H$ at the surface. The above formulation assumes that the mixed layer depth is a constant and the effect of the wind does not extend below the mixed layer.

The vertical dependence of u, v, w, and p is represented by an expansion into vertical modes:

$$(u, v, p) = \sum_{n=0}^{\infty} \sigma_n (\tilde{u}_n, \tilde{v}_n, \tilde{p}_n)\ \phi_n(z) \tag{8}$$

$$w = \sum_{n=1}^{\infty} \tilde{w}_n \psi_n(z) \tag{9}$$

where the wave functions ψ_n and ϕ_n are eigenfunctions of

$$\frac{d}{dz}\left(\frac{1}{N^2(z)}\frac{d\phi_n}{dz}\right) + \frac{1}{c_n^2}\phi_n = 0 \tag{10}$$

$$\frac{d^2\psi_n}{dz^2} + \frac{N^2(z)}{c_n^2}\psi_n = 0 \tag{11}$$

and c_n^{-2} are the eigenvalues; a rigid lid boundary condition [$\psi_n(0) = 0$, $\psi_n(H) = 0$] is assumed. We will refer to c_n as *modal eigenspeeds*, as they are not phase speeds. The eigenspeeds have units of velocity, are a function of stratification and ocean depth only, and define the minimum phase speed and maximum horizontal group speed of each vertical normal mode (Kundu, 1992).

For convenience we keep the normalization as in G84, so that

$$\phi_n(H) = 1, \tag{12}$$

and the weights σ_n are defined by the modal expansion of $S(z)$:

$$S(z) = \sum_{n=0}^{\infty} \sigma_n \phi_n(z) \tag{13}$$

Then, σ_n denotes the contribution of each mode to the initial velocity in the mixed layer, while the horizontal and temporal variation of the wavefield is controlled by the modal coefficients $\tilde{u}_n$, $\tilde{v}_n$, $\tilde{p}_n$, and $\tilde{w}_n$, which are functions of x, y and t. It is convenient to represent the zonal variations (x-dependence) of $\tilde{u}_n$, $\tilde{v}_n$, $\tilde{w}_n$, and $\tilde{p}_n$ by a Fourier transform:

$$(\hat{u}_n, \hat{v}_n, \hat{w}_n, \hat{p}_n) = \int_{-\infty}^{+\infty} (\tilde{u}_n, \tilde{v}_n, \tilde{w}_n, \tilde{p}_n) e^{-ikx} dx \qquad (14)$$

where the identifier $\hat{}$ denotes functions of (k, y, t). After substituting the modal expansions (8) and (9) into (1-5), Fourier transforming in x (14), and eliminating $\hat{w}_n$ and $\hat{p}_n$, we retrieve two coupled equations that govern the horizontal propagation of mode n :

$$\frac{\partial^2 \hat{u}_n}{\partial t^2} - f\frac{\partial \hat{v}_n}{\partial t} = -c_n^2 k^2 \hat{u}_n + ic_n^2 k \frac{\partial \hat{v}_n}{\partial y} \qquad (15)$$

$$\frac{\partial^2 \hat{v}_n}{\partial t^2} + f\frac{\partial \hat{u}_n}{\partial t} = +c_n^2 \frac{\partial^2 \hat{v}_n}{\partial y^2} + ic_n^2 k \frac{\partial \hat{u}_n}{\partial y} \qquad (16)$$

Having reduced the system variables from three, (u, v, p), to just two, (u, v), and converted to a fourth order system, we need to express the initial conditions (6) as a function only of (u, v) and their first order time derivatives. Applying the initial condition values (u^i, v^i, p^i) to the two horizontal momentum equations, we can estimate the current accelerations at time 0. The corresponding initial conditions (6) become:

$$[\hat{u}_n, \hat{v}_n]_{t=0} = \int_{-\infty}^{\infty} [u^i, v^i]_{t=0} e^{-ikx} dx$$

$$\left[\frac{\partial \hat{u}_n}{\partial t}, \frac{\partial \hat{v}_n}{\partial t}\right]_{t=0} = \int_{-\infty}^{\infty} \left[\frac{\partial u^i}{\partial t}, \frac{\partial v^i}{\partial t}\right]_{t=0} e^{-ikx} dx \qquad (17)$$

Note that these initial conditions are the same for each mode.

It is assumed that the horizontal structure of the initial condition is determined by the speed and direction of the atmospheric front; the model then tracks the oceanic response after the wind has imparted a velocity field into the mixed layer. The form of the initial condition is based on results from previous analyses of the mixed-layer response to an infinite front moving with a finite speed (e.g. Gill, 1982; Kundu and Thomson, 1985). The solution can be described for each baroclinic mode in terms of the advection speed C of the storm and the eigenspeed c_n of the mode. When $C < c_n$, the equation governing the horizontal radiation of the mode is elliptical, and the solution decays exponentially from the center of the storm. When the storm is fast, $C > c_n$, the equation is hyperbolic, and the solution is a wake of near-inertial oscillations propagating behind the forcing. In the latter case, the mixed layer inertial oscillations develop a horizontal wavenumber $\kappa = f_0/C$, where f_0 is the local inertial frequency. The quantity $2\pi/\kappa$ is called the "inertial wavelength" by Kundu (1985), and D'Asaro (1989) calls $1/\kappa$ the "advection scale" of the storm. We assume that the storm is fast relative to c_1, and since $c_1 > c_n$, the storm is faster than all modes. Therefore we choose the initial mixed-layer currents to have the form of pure inertial oscillations with horizontal wavenumber (k_0, l_0) given by

$$
\begin{aligned}
[u^i, v^i]_{t=0} &= U_0 L(y)\,[\cos(k_0 x + l_0 y - f_0 t), \sin(k_0 x + l_0 y - f_0 t)]\,|_{t=0} \\
\left[\frac{\partial u^i}{\partial t}, \frac{\partial v^i}{\partial t}\right]_{t=0} &= f U_0 L(y)\,[-\sin(k_0 x + l_0 y - f_0 t), \cos(k_0 x + l_0 y - f_0 t)]\,|_{t=0}
\end{aligned}
\qquad (18)
$$

where (k_0, l_0) is in the direction of C and $\kappa \equiv (k_0^2 + l_0^2)^{1/2}$. The function $L(y)$ is a smooth, slowly-varying function that limits the north-south extent of the initial disturbance (Fig. II.1). This function models either the weakening of a propagating front or the finite area of the ocean basin. No limit is yet specified in the east-west direction. The amplitude U_0 is left arbitrary at this point.

Equations (18) are equivalent to setting the pressure initial condition p^i to zero, consistently with a perfect inertial oscillation (no vertical displacement).

Note that the initial condition introduced above is considerably different than the one used by G84:

$$
\begin{aligned}
[u^i(y), v^i(y)]_{t=0} &= U_0 L(y)\,[\sin(l_0 y), 0] \\
\left[\frac{\partial u^i}{\partial t}, \frac{\partial v^i}{\partial t}\right]_{t=0} &= [0,0]
\end{aligned}
\qquad (19)
$$

In this formulation $k_0 = 0$, but the fundamental difference is that this initial condition is not consistent with inertial currents generated by a moving front. This velocity field has the structure of two waves: one propagating northward, one southward, i.e. a standing wave. Also, G84 adopted two values of horizontal extent: $L(y) = \infty$, and $L(y) = 2\pi l_0^{-1}$ (one wavelength). In the present study $L(y)$ is a parameter independent of l_0.

Using (18), the Fourier transformed initial conditions for mode n (17) will

$$\hat{u}_n|_{t=0} = \frac{U_0 L(y)}{2}\{[\delta(k-k_0)+\delta(k+k_0)]\cos(l_0 y - f_0 t)$$
$$+ i[\delta(k-k_0)-\delta(k+k_0)]\sin(l_o y - f_0 t)\}|_{t=0}$$
$$\hat{v}_n|_{t=0} = \frac{U_0 L(y)}{2}\{[\delta(k-k_0)+\delta(k+k_0)]\sin(l_0 y - f_0 t)$$
$$- i[\delta(k-k_0)-\delta(k+k_0)]\cos(l_o y - f_0 t)\}|_{t=0} \qquad (20)$$
$$\left.\frac{\partial \hat{u}_n}{\partial t}\right|_{t=0} = \frac{f U_0 L(y)}{2}\{[\delta(k-k_0)+\delta(k+k_0)]\sin(l_0 y - f_0 t)$$
$$+ i[\delta(k-k_0)-\delta(k+k_0)]\cos(l_o y - f_0 t)\}|_{t=0}$$
$$\left.\frac{\partial \hat{v}_n}{\partial t}\right|_{t=0} = \frac{-f U_0 L(y)}{2}\{[\delta(k-k_0)+\delta(k+k_0)]\cos(l_0 y - f_0 t)$$
$$- i[\delta(k-k_0)-\delta(k+k_0)]\sin(l_o y - f_0 t)\}|_{t=0}$$

become:where $\delta(k)$ is the Kronecker delta.

Equations (15) and (16) with the initial conditions (20) are solved numerically in y and t using finite-differences. The spatial resolution was 10 km and the time step was 10 minutes; typically 30 modes were used. The domain extended 2500 km north and south of the central latitude (y = 0). The extent to the north provides ample space for the initially northwards going waves to reach their turning latitude and turn to the south (Anderson and Gill, 1979); thus, no special boundary condition was needed on the northern limit of the domain. At the southern boundary, we incorporated a sponge layer; a body friction term was added to (15) and (16) with a friction coefficient $r_0(y)$ increasing linearly from 0 at y = -2000 km to a value determined by trial and error, at y = 2500 km. The slope dr_0/dy was determined by minimizing the waves reflected back from the southern boundary.

Without a sponge layer at the southern boundary Anderson and Gill (1979) demonstrated clearly that waves are reflected northward and create interference patterns with the southward propagating waves. The optimal solution would be the adoption of an absorbing boundary condition instead of a sponge layer. Such a condition has been proposed by Higdon (1992) for a wave equation similar to (15)-(16), however it requires an estimate of the phase speed of the waves. In the present case, the phase speed is time-varying and mode dependent, so the phase speed would have to be estimated at every time-step and for each mode, which could be quite complicated and computationally expensive.

II.4. Theoretical Considerations

Before solving the initial-value problem numerically, it is useful to consider the basic concepts of horizontal and vertical wave propagation expressed as a sum of vertical modes. These ideas will be valuable in interpreting the numerical solutions and will provide insight into the dependence of the evolution of the wavefield on the initial conditions (wavenumber and horizontal extent) and the background properties (mixed-layer depth and stratification).

II.4.*a. Dispersion relation.*

We can anticipate the numerical model results, by using ray theory to track the horizontal propagation of vertical modes. To apply ray theory we assume that the horizontal dependence of the amplitude of a mode can be expressed in the form $\exp[i(kx+ly-\omega t)]$; i.e. each mode can be expressed as a horizontally-propagating plane wave with slowly varying wavenumbers and frequency. Substitution into (15) and (16) yields a fourth order polynomial for the frequency ω; one root, $\omega=0$, is artificial, introduced by the rise of the system to fourth-order; the second root describes the vortical mode on an *f*-plane, or a Rossby planetary wave on a β-plane. the two remaining roots of the characteristic polynomial are the solutions to the dispersion relation for each mode

$$\omega_n^2 = f^2 + c_n^2(k^2 + l^2) \qquad (21)$$

The near-inertial internal gravity waves following (21), will have a much stronger response to the initial conditions (18), than the Rossby wave solution.

It proves convenient to define at this point a dimensionless parameter ε by

$$\epsilon \equiv \frac{c_n^2(k^2+l^2)}{f^2} \tag{22}$$

It can be shown that ε is equivalent to the square of the ratio of the Rossby radius to the horizontal scale (1/κ) of the waves when the Rossby radius is defined by the minimum phase speed, c_n , over f (Gill, 1984). Although ε is time and mode-dependent, it is in general less than 0.05 for typical mid-latitude conditions. Note that ε increases toward the equator.

Using the dispersion relation (21), the ray equations become (e.g. Lighthill,1978):

$$\begin{aligned} \frac{dx}{dt} &= \frac{\partial \omega_n}{\partial k} \qquad (\equiv C_{g_n}^x) \\ &= \frac{c_n^2 k}{f}(1+\epsilon)^{-1/2} \end{aligned} \tag{23}$$

$$\begin{aligned} \frac{dy}{dt} &= \frac{\partial \omega_n}{\partial t} \qquad (\equiv C_{g_n}^y) \\ &= \frac{c_n^2 l}{f}(1+\epsilon)^{-1/2} \end{aligned} \tag{24}$$

$$\frac{dk}{dt} = -\frac{\partial \omega_n}{\partial x} \qquad (25)$$
$$= 0$$

$$\frac{dl}{dt} = -\frac{\partial \omega_n}{\partial y} \qquad (26)$$
$$= -\beta (1+\epsilon)^{-1/2}$$

where $\beta \equiv df/dy$. These equations define the ray path along which the energy in each mode propagates as well as the wavenumber changes along that ray. Since the dispersion relation is not a function of t or x, then ω and k are invariant along a ray. Due to the β effect the north-south wavenumber varies as the wave propagates along the ray for small ε (26) as:

$$l(t) = l_0 - \beta t \qquad (27)$$

For an initial wavenumber $l_0 < 0$ (southward propagation), the *magnitude* of l increases linearly in time; for $l_0 > 0$ (northward propagation), the magnitude initially decreases, goes through zero, and finally increases, linearly in time. As a result of the time dependence of the meridional wavenumber, the rays are curved (Fig. II.2). A northward ray eventually reaches its turning latitude and turns to the south (Fig. II.2a), while a southward ray keeps turning more southward until it crosses the equator (Fig. II.2b).

Note that for small ε, the components of the group velocity, $C_{gn}{}^x$ and $C_{gn}{}^y$ are functions only of the wavenumber component that is in the same direction, k and l, respectively. Hence, for small ε, the meridional wavenumber does not have any effect on the zonal propagation of the waves, and vice versa. Also, for small values of ε, the dispersion relation can be written approximately in simpler form:

$$\omega_n = f\left(1 + \frac{\epsilon}{2} + \ldots\right) \approx f + \frac{c_n^2(k^2+l^2)}{2f} \tag{28}$$

II.4.*b. Modal interference (beating).*

G84 explains in detail how the vertical propagation of near-inertial energy is expressed as a sum of vertical modes. Initially the sum of the modes matches the function $S(z)$; a constant value in the mixed-layer and zero below. In this problem all modes have the same initial horizontal wavenumber (k_0, l_0). Also for all modes, $k = k_0$ is constant in time; l changes in time as given in (27) but the change is the same for all modes. Since $c_1 > c_2 > c_3 > \ldots$, the lower the mode the higher its frequency (21). The frequency of the high modes is very nearly f_0 because c_n goes to 0 as $n \rightarrow \infty$. Since each mode oscillates at a slightly different frequency, their relative phase is constantly changing in time. G84 defines as t_n the time when mode n will become out of phase with the high modes at frequencies near f_0:

$$t_n = \frac{\pi}{(\omega_n - f_0)} \tag{29}$$

At time t_1, mode 1 will add destructively to the other modes in the mixed layer, and the sum of the modes below the mixed layer will no longer be zero. Thus, we will observe some vertical propagation of energy from the mixed layer into the pycnocline. At time t_2 mode 2 will be out of phase with the high modes and more energy will have propagated into the pycnocline. However, this reasoning is oversimplified, since by time t_2 mode 1 may again be enforcing the mixed layer currents again. Thus, energy exchanges between the mixed layer and the pycnocline, called inertial beating, can be explained as a result of the interference of

vertical modes, and the time scales for these exchanges are determined by the frequency differences between the modes. On an f-plane the time scale t_n is easily calculated since ω_n is constant.

Here, we modify the formulation defining t_n to incorporate β-plane geometry; t_n from (29) is more complicated since ω_n is a function of time:

$$\omega_n \simeq f_0 + \frac{c_n^2[k_0^2 + (l_0 - \beta t)^2]}{2f_0} \tag{30}$$

Note that this frequency, observed at $y = 0$, changes in time, while the frequency following a ray is constant. This is because the waves observed at $y = 0$ continually come from different ray paths. For an Eulerian observer, $f = f_0$ (a constant) and ω_n varies; for an observer moving along a ray, $f = f(y)$ and ω_n is a constant. In the present context we analyze the model results from an Eulerian viewpoint, and thus we use f_0 in (21) and equations derived from it. Substituting (30) into (29), we get a cubic equation for t_n:

$$t_n^3 - \frac{2l_0}{\beta} t_n^2 + \frac{k_0^2 + l_0^2}{\beta^2} t_n - \frac{2f_0 \pi}{c_n^2 \beta^2} = 0 \tag{31}$$

which has three roots. The smallest, positive, real root defines the t_n of interest, i.e. the first time at which mode n will be out of phase with f_0. Fig. II.3a shows values for t_1 and t_2 as a function of k_0 and l_0 using $c_1 = 2.8$ m s^{-1} and $c_2 = 1.9$ m s^{-1}, for typical mid-latitude stratification and $H_{mix} = 150$ m. Note that the largest value of t_1 ~ 20 days, are found at $k_0 = 0$, $l_0 = 1.5 \times 10^{-5}$ m^{-1}, which correspond to a northward moving storm. Also note that at high wavenumbers the asymmetry between north and south-going waves due to the β-effect tends to decrease.

II.4.*c. Modal departure due to north-south propagation.*

Ray theory can be used to understand the effect of a finite north-south extent of the initial disturbance. The energy of each mode propagates meridionally at the group velocity given by:

$$C_{g_n}{}^{y} = \frac{c_n^2 l}{f_0} = \frac{c_n^2 (l_0 - \beta t)}{f_0} \tag{32}$$

for small ε. The group velocity can be used to compute the time it takes for the energy in a mode to propagate meridionally between two points. The time τ it takes for a mode to travel from $y = y_0$ to $y = 0$ is given by the integral

$$y_0 = -\int_0^{\tau} C_{g_n}{}^{y} dt \tag{33}$$

Substituting (32) into (33) , we can solve explicitly for τ:

$$\tau^2 - \frac{2l_0}{\beta}\tau + \frac{2fy_0}{c_n^2 \beta} = 0 \tag{34}$$

In the case of initially south-going waves ($l_0 < 0$) there is one positive root for $y_0 > 0$; there are no real roots for $y_0 < 0$, as the wave never reaches $y = 0$ (Fig. II.2b). For north-going waves ($l_0 > 0$) there are 2 positive roots when

$$y_0 > -d_{crit} \equiv -\frac{c_n^2 l_0^2}{2f_0 \beta} \tag{35}$$

(where d_{crit} is the northward distance a ray travels before turning) representing the 2 times the ray crosses $y = 0$ (Fig. II.2a). At the first crossing the wave is going northward and at the second it is going southward after reflecting at the turning latitude. Waves starting at $y_0 < -d_{crit}$ never reach $y = 0$. Based on the above modal propagation estimates, we can determine the duration for which a mode will be present at $y = 0$. We define τ_n^{NS} as the time when all the energy at mode n initially to the north or south of $y = 0$ will have propagated away and will no longer contribute to the wave field at $y = 0$. Fig. II.2 clearly demonstrates that it is always the ray that starts from the northernmost point that is the last to leave the point $y = 0$, independent of the propagation direction of the initial wave. By replacing y_0 by L_N in (34), we can calculate the time τ_n^{NS} after which all the energy of mode n will have propagated away from $y = 0$, never to return.

Clearly, τ_n^{NS} is a function of l_0 and the northern extent L_N. As an example, the time τ_n^{NS} is contoured in units of days as a function of initial wavenumber l_0 and northern extent L_N for typical mid-latitude stratification with $H_{mix} = 150$ m and $k_0 = 0$ (Fig. II.3b). The shadowed areas in the same figure represent the parameter range where $t_n > \tau_n^{NS}$; there, the evolution of the wave field is determined by modal departures rather than modal interference.

II.4.*d. Modal departure due to east-west propagation.*

The effect of an initial finite east-west extent is simpler than considering north-south propagation, since C_{gn}^{x} is constant in time for small ε. Let the initial east-west extent from $x = 0$ be L_E and L_W respectively. For an eastward propagating wave ($k_0 > 0$), the propagation time τ_n^{EW} for a mode to go from $x = L_W$ to $x = 0$ is given by:

$$\tau_n^{EW} \equiv \frac{L_w}{C_{g_n}^x} = \frac{f_0 L_w}{c_n^2 k_0} \qquad (36)$$

After time τ_n^{EW} mode n will no longer contribute to the solution at $x = 0$. For a westward propagating wave, τ_n^{EW} is also given by (36) after replacing L_W by L_E.

II.4.*e. Comparing the time scales.*

The time scales of inertial beating t_n and the time scales of propagation τ_n^{NS} and τ_n^{EW} are useful concepts that help in understanding the results of the numerical model. Both of these time scales are functions of the modal eigenspeed c_n that depends on the stratification and ocean depth. If τ_n^{NS} or τ_n^{EW} are smaller than t_n, then mode n will have propagated away horizontally before the effect of inertial beating involving that mode would be observed. The darkened areas of Fig. II.3b represent the initial condition parameter range where $\tau_n^{NS} < t_n$.

To summarize the meridional propagation of the modes and their relative phase difference, we introduce Fig. II.4. The phase difference $(\Delta\phi_n = (\omega_n - f)\, t)$ between the seven lowest modes and a perfect inertial current, representative of high modes, is plotted as a function of time. Solid horizontal lines are drawn at π and 3π where the low modes add destructively to the high modes; a dashed line is drawn at 2π and 4π, where the modes interfere constructively. The times when the phase line of each mode intersects the line $\Delta\phi_n = \pi$ define t_n. Superimposed on the phase plots, are the estimated times τ_n^{NS} where all the energy of a mode will have departed, for various values of L_N. All the estimates were made for $l_0 = 2\text{x}10^{-6}\text{m}^{-1}$ and $k_0 = 0$. For example for a small northern extent of 250 km, we expect that the first two modes will propagate away before they beat with f_0, while the third mode will barely have

time to beat before leaving. On the contrary, for a large northern extent of 1500 km, the time at which mode 1 leaves the area $\tau_1^{NS} \approx 19.5$ days is greater than $t_1 \approx 10.5$ days--thus, the first mode will "beat" before leaving. In fact since mode 1 is still present near day 17, both mode 1 and 2 will again be in phase, i.e. $\Delta\phi_1 \approx 3\pi$ and $\Delta\phi_2 \approx \pi$. Hence, the first 2 modes will add constructively and interfere destructively with the other modes; so, we expect much of the energy to have propagated into the pycnocline.

II.5. Model Results

The numerical model was run to determine the radiation of near-inertial motion from the mixed layer for a range of values of the initial conditions (horizontal wavenumber, north-south extent) of the wavefield, and background properties (stratification, mixed-layer depth). The effect of one factor on the near-inertial propagation is not independent of the others; however some idea of the model behavior can be obtained from a small number of model runs. The model results are interpreted with the aid of the wave concepts discussed in section 3. This promotes a physical understanding of the model and will permit us to predict model results without actually running the numerical model.

We chose a stratification profile used in G84 given by

$$N(z)=\begin{cases} \dfrac{s_0}{H+H_{vir}-z}\,, & z<H-H_{mix} \\ 0\,, & z\geq H-H_{mix} \end{cases} \qquad (35)$$

where s_0 = 2.5 ms^{-1}, and $H_{vir} \equiv s_0/N_0 - H_{mix}$. This profile has a peak N_0 at the base of the mixed layer, and s_0 is chosen to fit a typical ocean profile. This idealized $N(z)$ is compared with historical data from the Pacific and Atlantic Oceans in Fig. II.5. Profiles of the idealized $N(z)$ for a variety of mixed layer depths are shown in Fig. II.6 with the corresponding values of σ_n and c_n. The dependence of the wave propagation on the seasonal (mixed-layer depth) and deep stratification are considered below.

II.5.*a. Model runs: f versus β-plane.*

Sample results of model runs on an f-plane and β-plane are shown in Fig. II.7. In these runs L = 3000 km and H_{mix} = 100 m. The initial wavenumber is consistent with a storm front moving southward at 20 m/s, that is $l_0 \simeq -5\times10^{-6}$ m^{-1} =

(-200 km)$^{-1}$, and $k_0 = 0$. At $y = 0$, the vertically-integrated horizontal kinetic energy (HKE) over the entire depth E_T (0 to 4000 m), the mixed layer E_{ML} (0 to H_{mix}) and the pycnocline E_{PC} (H_{mix} to H_{mix}+200 m) are shown in the upper panels (Fig. II.7). The middle panels display the u component of velocity in the mixed layer as a function of latitude and time. The modeled currents were complex-demodulated around f_0, using a boxcar window four inertial periods long. The phase was backrotated in time at the local inertial frequency f_0.

On an f-plane, the initial wavenumber l_0 is too small for effective inertial pumping (Fig. II.7a). Hence E_{ML} decreases slowly during the first 30 days while l remains constant. The decrease in E_{ML} is primarily due to the vertical propagation into the pycnocline as E_T remains relatively constant. The theoretical time scale t_1 = 35 days for inertial beating is consistent with the numerical model decrease in E_{ML}. The fact that the north-south extent is finite is not important in this case as τ_1^{NS} is much greater than t_1--the waves propagate southward, but very slowly.

On the β-plane (Fig. II.7b) smaller scales develop in time as suggested by theory (27). Note that inertial pumping increases as the horizontal scale decreases. By day 10 the horizontal scale has decreased to 100 km (wavelength of 600 km) and much of the energy has left the mixed layer. This decrease in E_{ML} occurs at time t_1 and can be explained by the beating (destructive interference) of mode 1 with the other modes. By day 13 E_{ML} increases; at this time mode 1 is again in-phase with most of the other modes. E_T remains about the same until day 17; the decrease in E_T occurs at time τ_1^{NS} when mode 1 has propagated away from $y = 0$, never to return.

The bottom panels of Fig. II.7 display the inertial currents at $y = 0$ (50^{0}N) as they evolve with depth and time; contours of amplitude are superimposed on the current vectors at selected depths, backrotated at f_0. Although the currents propagate vertically from the mixed-layer downwards, E_{PC} is concentrated within the top 40 meters of the pycnocline (100-140 m) in both the f and β-planes. However, in the β-plane a larger fraction of the HKE penetrates into the deep ocean by day 30. In

fact at times when $E_{ML} \simeq 0$, the HKE is approximately equally divided between E_{PC} and the deep water.

As the current vectors have been inertially backrotated, a change in slope denotes a frequency different from f_0. On an f-plane at a constant depth, the current vectors rotate very slowly and monotonically clockwise in time, which indicates that the frequency is slightly superinertial. However, on a β-plane the current vectors rotate faster (mostly clockwise), denoting a higher frequency. The current in the mixed-layer is homogeneous; there is a significant phase jump across the base of the mixed-layer. At times when the amplitude is a minimum in the mixed-layer, sub-inertial frequencies can be identified for a couple of inertial periods. In the β-plane the currents between 140 and 1000 m depth are mostly in phase, while the phase seems to change sign below 2000 m; this pattern suggests the dominance of the first mode in determining the deep wave-field.

II.5.*b. Understanding the model results: comparison with analytical predictions.*

The model results of vertically integrated HKE as a function of depth and time for L_N = 250, 500 and 1000 km and H_{mix} of 25, 50, 100 and 150 m are shown in Fig. II.8. The initial HKE in J m^{-2} per meter of mixed layer is the same for each value of H_{mix}. The initial wavenumber in the top four rows is consistent with a storm front moving southward at 15 m s^{-1} ($k_0 = 0$, l_0= -0.75 x 10^{-5} m^{-1}). In the last row, the initial wavenumber is set by a storm propagating northward at the same speed ($k_0 = 0$, l_0 = +0.75x 10^{-5} m^{-2}). The corresponding relative phases, backrotated at frequency f_0 are shown as a function of time at various depths (Fig. II.9).

The decrease in E_T can be attributed to horizontal propagation (Fig. II.8). The larger the northern extent L_N, the longer the time a given mode will contribute at $y = 0$. The analytical predictions of time-scales τ_1^{NS} as calculated from (34) are also indicated in Fig. II.8. For a given H_{mix}, the decay of the total HKE is faster when the northern extent L_N is smaller. The first decrease in E_T is coincident with τ_1^{NS}; this is consistent with the idea that mode 1 has left $y = 0$ heading south. For

the smaller extents mode 2 may also leave within the first 30 days causing an additional decrease in E_T. Note that the waves initially going northward (last row, Fig. II.8) persist for a longer time before finally propagating away to the south.

The decrease in E_{ML} that is in excess of the decrease in E_T is the result of vertical propagation. Hence, E_{PC} increases as E_{ML} decreases. The time scale of this vertical propagation is denoted by the inertial beating time t_n. For the case of L_N= 1000 km the effect of inertial beating is clearly evident for mode 1 at t_1 and mode 2 at t_2. When L_N= 250 km the time scale t_1 is not relevant as $\tau_1^{NS} < t_1$ --hence mode 1 has left and therefore cannot beat with other modes. However, there is still vertical propagation of energy, but it cannot be explained by beating. In this case the vertical propagation can be understood in terms of the sum of modes. Initially, the sum of modes below the mixed layer was zero. After mode 1 leaves, the sum cannot be zero any more. In the mixed layer the amplitude of the inertial oscillation was due to the sum of modes, all in phase. When a mode leaves, the sum has to be smaller. Thus, the departure of the low modes results in a downward propagation of energy. For southward going initial conditions, the analytically predicted values of t_n and τ_n^{NS} are in good agreement with the changes of HKE due to vertical and horizontal propagation respectively. This fact suggests that the plane wave arguments (section 3) can be used for making predictions about the evolution of the HKE in near-inertial wavefields. Similar time-scale arguments for northward propagating initial conditions are reasonable, but t_n and τ_n^{NS} seem to be underestimated by a few days. This could be because l reaches $l = 0$ before turning negative, a region where ray theory does not apply.

The detailed phase structure is quite complicated (Fig. II.9). The slope of each phase line defines the local frequency at a certain depth; as the currents are backrotated by f_0, horizontal lines denote perfectly inertial currents. Positive slopes represent super-inertial frequencies, while negative slopes correspond to sub-inertial currents. The distance between phase lines denotes the phase difference with depth, a quantity related to vertical wavenumber; the temporal change of phase difference

between two depths reveals the change of vertical structure in time.

The overall frequency changes in time can be understood somewhat by examining the frequency changes of each mode. However, the frequency is the complicated result of adding the contribution from each mode and depends on both the frequency and magnitude of each mode. The frequency of mode n is given by (21) or (30)--at a fixed location y=0 the frequency increases in time. High modes are initially at a lower frequency than low modes. Also the rate of change of frequency at higher modes is slower; this is because the rate of change of frequency is proportional to c_n^2. In general the mixed layer frequency is about 1.005 f_0, and the frequency increases with increasing depth, resulting in significant phase changes with depth.

II.5.*c. Effects of mixed-layer depth on the evolution of the wavefield.*

The quantitative changes in HKE that are associated with the time scales t_n and τ_n^{NS} depend on the modal decomposition of the initial condition, that is upon σ_n. The values of σ_n and c_n for the cases shown in Fig. II.5 are presented in Table II.1 for the five lowest modes.

The fraction of energy initially in mode 1, that is σ_1, increases dramatically with mixed layer depth. This fact can explain much of the model dependence on H_{mix}. As was seen in Fig. II.8, at time $\tau^{NS}{}_1$ mode 1 energy leaves y = 0 causing a decrease in E_T. The magnitude of the decrease is expected to be related to σ_n. Specifically from Table II.1 for H_{mix} = 25 m, it is expected that E_T would decrease by 7% by $\tau^{NS}{}_1$; for H_{mix} = 150 m the decrease would be a substantial 42%. These expectations are verified in Fig. II.8.

The magnitude of the decrease in E_{ML} due to inertial beating can also be anticipated from the σ_n values. By time t_1 when mode 1 is out of phase with nearly all other modes (destructive interference), it is anticipated that the current speed in the mixed layer would be reduced by $2\sigma_1$, very significantly reducing E_{ML}. Hence, this beating effect is expected to be more dramatic for larger H_{mix} as can be seen in

Fig. II.8. The beating effect is almost absent in the cases of small L_N where $\tau^{NS}_1 < t_1$ -- mode 1 has left before significant beating occurred.

Note that while changes in the seasonal stratification have a profound effect on σ_n, the effect on c_n is rather small (Fig. II.6, Table II.1). Mixed layer variation from 25 to 150 m results in changes of c_1 of 20% and less than 5% for higher modes. This is a significant result because it means that the time-scale of the wave evolution is not a strong function of mixed layer depth, while the magnitude of the decrease is. As a corollary, one can use historical hydrographic data to make a first estimate for energy propagation time-scales.

Investigating the phase structure of the modelled currents (Fig. II.9), we observe the largest variations in frequency for the case where H_{mix} = 150 and L_N = 1000 km. These changes, occurring at times t_1 and t_2, are the result of the inertial beating of first mode 1 and then mode 2 with the other modes. When the beating is most significant the amplitude is small and the phase jumps. By 25 m below the mixed layer the currents are nearly 180° out of phase with the mixed layer currents. In general the frequency increases with depth. The amount of increase is determined by the dominance of the low modes at that depth. Hence when H_{mix} is large and the low modes dominate the solution, the frequency increase with depth is great. When H_{mix} = 25 m, the modal distribution is more uniform, and the frequency change with depth is weaker.

II.5.*d. Effects of deep stratification on the wave evolution.*

In addition to the mixed layer depth (seasonal stratification) the variations in the deep stratification affect wave propagation. Since we have found that many of the features of the numerical model results can be explained by analytical wave propagation, we will assess the role of deep stratification without explicitly solving the numerical model.

Vertical profiles of zonally-averaged temperature and salinity for the Atlantic and Pacific Oceans were obtained from Levitus (1982). Assuming a 50 m mixed layer in all cases, $N(z)$ was calculated and values of c_n and σ_n were estimated by modal decomposition for various latitude bands (Table II.2 and II.3, Fig. II.10).

In most of these profiles σ_n has a maximum at a mode greater than 1. At 47.5^0 N in the Atlantic modes 4 & 5 are more energetic than modes 1, 2 and 3 combined. This behavior of σ_n is not found in the idealized $N(z)$ profile (35). A different idealized profile might model this feature of the stratification better, but this is not critical to the present discussion. For waves propagating in these average stratifications, the model will behave as discussed above, but mode 1 will have proportionately less impact on the solution than with the idealized $N(z)$, since the relative importance of each mode is given by σ_n.

The values of c_n also vary with stratification. The weaker deep stratification toward the poles leads to lower values of c_n. However, the dependence of c_n on mode remains nearly proportional to n^{-1}.

Both the frequency and the group velocity of the waves are functions of $c_n^2 f_0^{-1}$. At high latitudes, weaker stratification and high f_0 cause the vertical and horizontal propagation of energy to be much slower than the idealized mid-latitude case examined above. This is seen in the estimates of t_1 and τ_1^{NS} (Fig. II.11a). In contrast at low latitudes, stronger stratification and smaller f_0 result in faster wave propagation and shorter time scales (Fig. II.11b). Estimating the time-scales t_n and τ_n^{NS} for the idealized profile at high and low latitudes, we arrived at the conclusion that, in general, both stratification and latitude can be equally responsible in determining the evolution time-scales of the wavefield.

II.5.*e. Conditions for a two-dimensional approximation.*

It has been a common practice in past modelling efforts to consider only two-dimensions: depth and one horizontal dimension. The reasons for using a two-dimensional model are obvious: both the analytical and the numerical relations are simpler and the numerical schemes are easier to run. Price (1983) and Kundu (1985) used *f*-planes, and aligned the *x*-axis with the direction of propagation of the atmospheric front. This simplification is always possible and exact in an *f*-plane.

In a β-plane the 2-dimensional assumption is made by neglecting the zonal component of the wavenumber (k) (G84; D'Asaro, 1989). This is often reasonable since k_0 is often small and k is constant in time. In contrast l increases as βt; so no matter how small l_0 , l will eventually be large enough to generate significant vertical propagation.

To determine the conditions for which k can be neglected we first consider the effect of k on the frequency given by the dispersion relation (21). We compare the frequency ω_{n0} for $k = 0$, with the frequency ω_{nk} for $k = k_0$. These two frequencies will be considered to be sufficiently close for times less than $\bar{t}_n$, where $\bar{t}_n$ is defined when the phase difference between the two frequencies reaches $\pi/4$, that is, where $(\omega_{n0} - \omega_{nk})\, \bar{t}_n = \pi/4$. Since we are in the parameter range where k is small, we assume ε is small and use (30) to estimate $\bar{t}_n$ explicitly as:

$$\bar{t}_n = \frac{\pi}{2} \frac{f_0}{c_n^2 k_0^2} \qquad (38)$$

Note that $\bar{t}_n$ is independent of l_0, and depends only on k_0, stratification and f_0. If we consider the full dispersion relation (21) ($\varepsilon \neq 0$), $\bar{t}_n$ varies slowly with l_0. Since mode 1 always has the highest frequency, for a given k_0, the zonal dependence can be neglected in the model for times less than $\bar{t}_1$. Fig. II.12 shows $\bar{t}_1$ as a function of k_0 for the idealized $N(z)$ profile at mid-latitudes (50°N), as well as the extreme cases of zonal averages of $N(z)$ at low-latitudes (27.5^0 N) and high latitudes (67.5^0

S). To verify that ε small is a reasonable approximation, estimates of $\bar{t}_1$ were made using the full dispersion relation for $l_0 = 0$ and for $l_0 = \pm 10^{-5}$ m^{-1}. For the mid-latitude case, at $k_0 = 10^{-5}$ m^{-1} (a scale of 100 km), $\bar{t}_1 = 3$ days, while for larger scale $k_0 = 0.5 \times 10^{-5}$ m^{-1} (scale of 200 km), $\bar{t}_1 = 10$ days.

II.5.*f. Conditions for neglecting* β.

For sufficiently small times the β effect will not be important and an *f*-plane model can be used. We can determine this time scale, in analogy with the previous section, by considering the effect of β on the frequency. Let ω_{nf} be the frequency for $\beta = 0$ and $\omega_{n\beta}$ be the frequency including β. These two frequencies will be considered to be sufficiently close for times less than $\hat{t}_n$, where $(\omega_{nf} - \omega_{n\beta})\, \hat{t}_n = \pi/4$. Again, we only need to estimate $\hat{t}_1$, since it is shorter than all other $\hat{t}_n$. For the case of small ε, $\hat{t}_1$ is independent of k_0 and is a function of l_0, stratification and latitude given by

$$\hat{t}_1^3 - \frac{2l_0}{\beta}\hat{t}_1^2 - \frac{\pi f_0}{2c_1^2\beta^2} = 0 \qquad (39)$$

For significant ε, $\hat{t}_1$ becomes a slowly-varying function of k_0. Fig. II.13 shows $\hat{t}_1$, as calculated by assuming small ε and the full dispersion relation. For a given k_0 and l_0, the β-effect can be neglected in the model for times less than $\hat{t}_1$.

II.6. Summary and Conclusions

Time-varying wind stress generates near-inertial oscillations in the upper ocean. Significant generation often occurs after the passing of a storm, and locally lasts for a few hours; over large areas, the generation lasts for a few days, the time it takes for an atmospheric front to travel over the ocean. After the storm event, the disturbance created in the upper ocean radiates vertically and horizontally as near-inertial gravity waves.

In this paper we consider the radiation of the wavefield that is consistent with linear, inviscid dynamics on a β-plane (section 2). The wave evolution is calculated using a numerical model patterned after the initial-value problem introduced by G84. The numerical model differs from the one developed in G84 by:

- adding the third spatial dimension, permitting zonal gradients,
- limiting the horizontal extent of the storm to an arbitrary scale, and
- setting the initial condition in the mixed layer to be consistent with the passing of a fast moving front.

The model results are interpreted in the framework of analytical linear wave theory (section 3) on a β-plane. The association of the numerical model and analytical theory permits predictions of many features of the wave evolution without the need to run the numerical model. Based on the agreement of numerical and analytical results, we also develop a set of criteria enabling the reduction of the geometry of the problem to two dimensions (sections 4e, f).

The horizontal propagation of modes at distinct speeds causes vertical propagation of energy through two mechanisms: Modal interference and modal departure.

When the initial mixed-layer currents have a large horizontal extent ($L_N >$ 500 km), the vertical propagation of energy is caused by the interference of modes characterized by different frequencies (inertial beating). The time scale t_n is the time

of inertial beating of mode n, and the beating of mode 1 at t_1 marks the first time of effective vertical propagation of energy. The value of t_n depends greatly on the initial wavenumber of the currents in the mixed layer. The β-effect causes a great difference in t_n between an initially northward or southward propagating front--inertial beating occurs sooner for a southward going front (Fig. II.3a).

For initial conditions of short horizontal extent (L_N < 250 km), the dominant cause of vertical propagation of energy is the successive departure of modes from the generation area. To describe this process, we have defined the time scales τ_n^{NS} and τ_n^{EW}, representing the times when mode n leaves $y = 0$ due to horizontal propagation. These time scales are a function of the horizontal extent of the storm as well as the initial wavenumber (Fig. II.3b).

Beside the initial wavenumber all the time scales are affected by the modal eigenspeeds c_n and the value of f_0. Hence, variations in stratification and latitude will affect the absolute time scale. We estimated that the evolution of the near-inertial waves varies from a few days at low latitudes to several weeks at high (Fig. II.11).

In addition to the time scales the modal decomposition of the wavefield is needed to determine the quantitative effect of the inertial beating and horizontal propagation. For example, if mode 1 is a large fraction of the total energy (σ_1 large), then the vertical propagation at t_1 will be significant. The modal composition is set by the stratification. The deeper the mixed layer the larger the mode 1 contribution. Hence the energy transfers at times t_1 and τ_1^{NS} are more dramatic for deeper mixed layer (Fig. II.8).

From the two processes described by the model, it is modal interference that can be associated with the frequently observed intermittency of the near-inertial waves. When the modal departure is the dominant mechanism of downward propagation of enegry, there is no intermittency ("beating") observed (Fig. II.8). The intermittency can also be traced in the currents' phase, as short periods of sub-inertial frequencies, coincident with amplitude minima (Fig. II.9).

The three-dimensional model developed in this chapter provided us with confidence on the ability of analytical theory to describe the evolution of the inertial wavefield generated by a large, fast storm propagating at any direction. However, in order to assess the validity of either model or theory, a comparison with oceanic observations is needed. The validity of the present analysis can also be tested by the development of a simple model forced by wind-stress, where the decay of the mixed-layer oscillations is consistent with the predictions developed here. Chapters III and IV of this thesis are both steps to that direction.

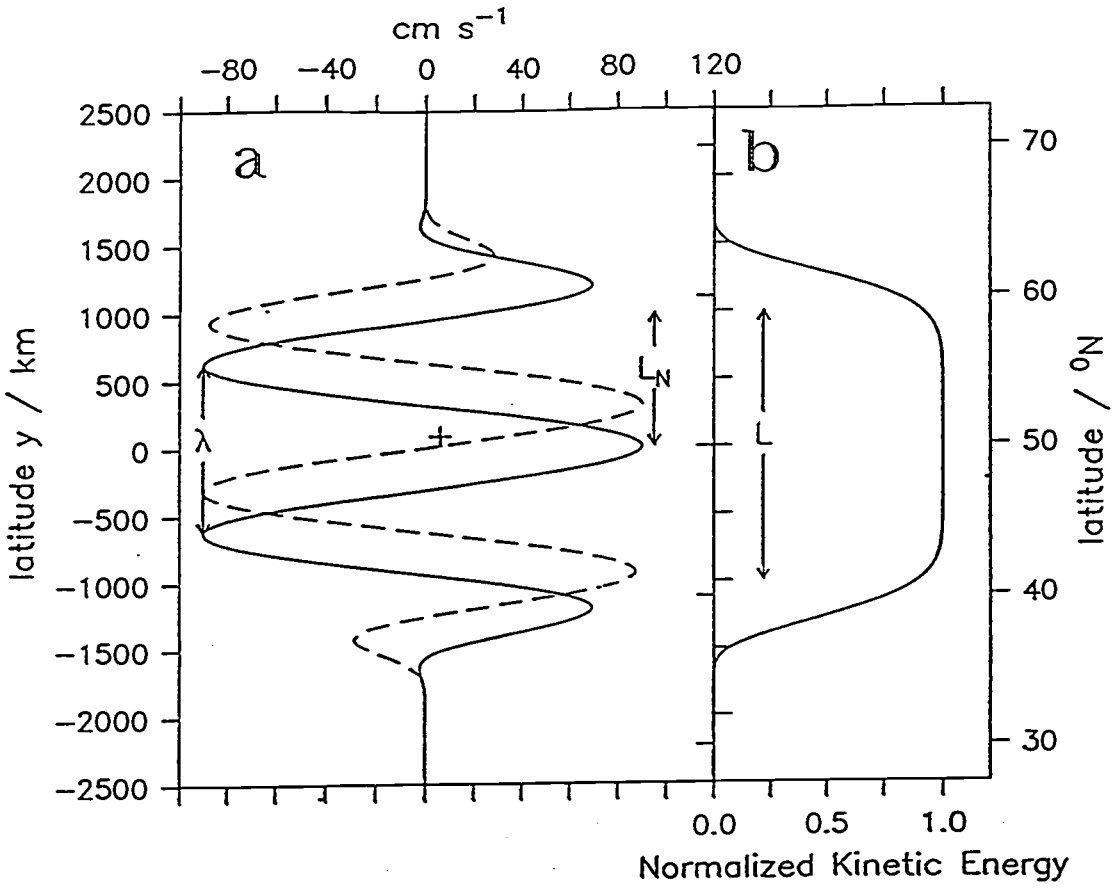

Fig. II.1. (a) Example of initial conditions u^i (solid line), v^i (dashed line) as a function of latitude, with a meridional wavelength $\lambda = 2\pi l_o^{-1} \simeq 628$ km, and a northern extent $L_N = 1000$ km. (b) The normalized HKE of the initial condition, as a function of latitude. Latitude scale is given in both degrees and kilometers.

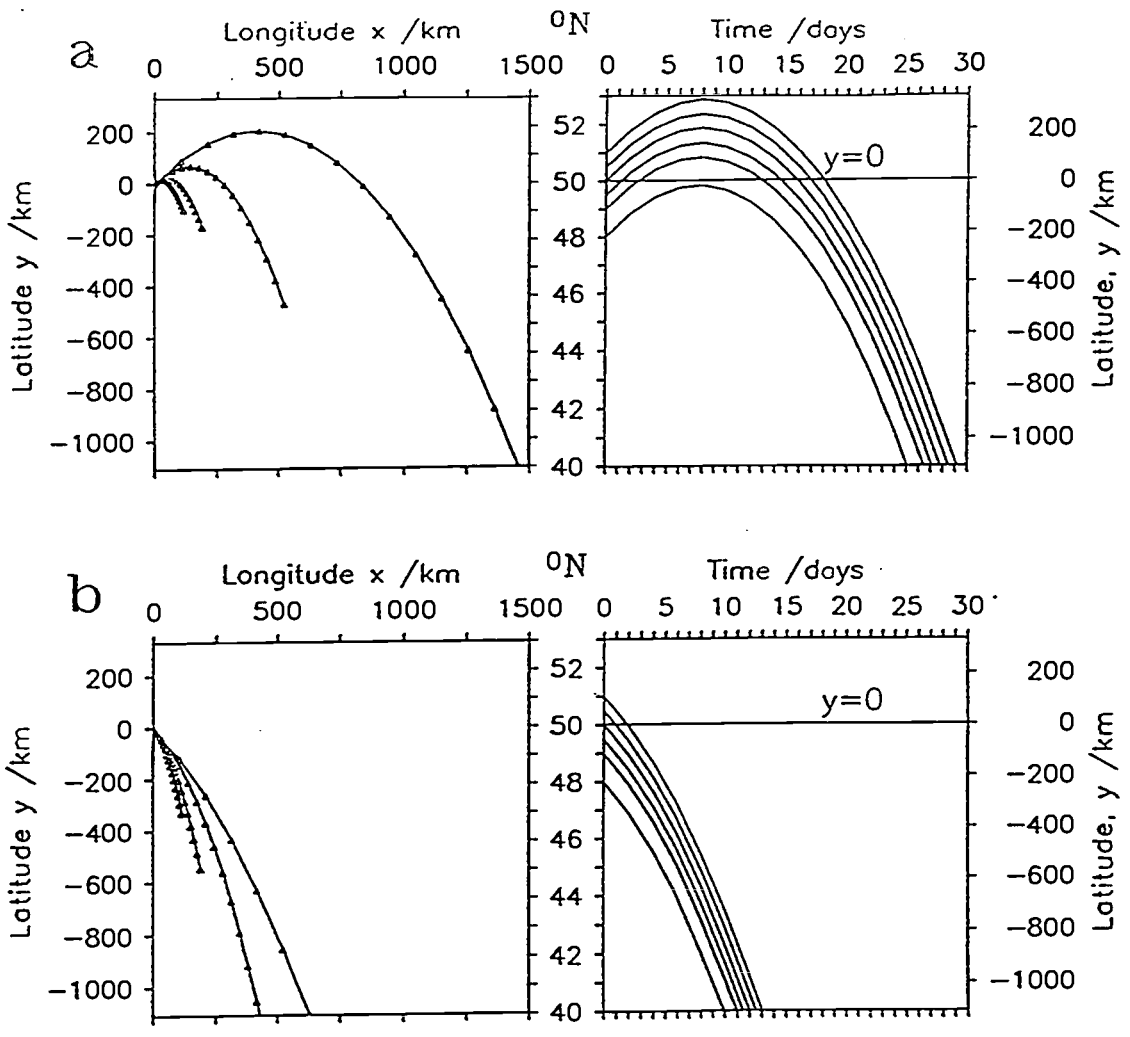

Fig. II.2. Example of ray paths for initial wavenumber (k_0, l_0) of (a) a northward-going wave (0.01, 0.01), and (b) a southward-going wave (0.01, -0.01). The panels on the left display the ray-paths of the lowest four modes, starting at y = 0, as a function of latitude and longitude. Paths are plotted for no more than 30 days; a mark is plotted on the ray every two days. Note that the very low modes travel very fast and soon leave generation area; the higher modes effectively remain where they were forced. The right panels display the ray paths on a latitude-time plane of a single mode (the lowest one) that starts from different values of y. Note that it is always the northernmost ray that is the last to leave the observation point y = 0 (in this case, 50^0N).

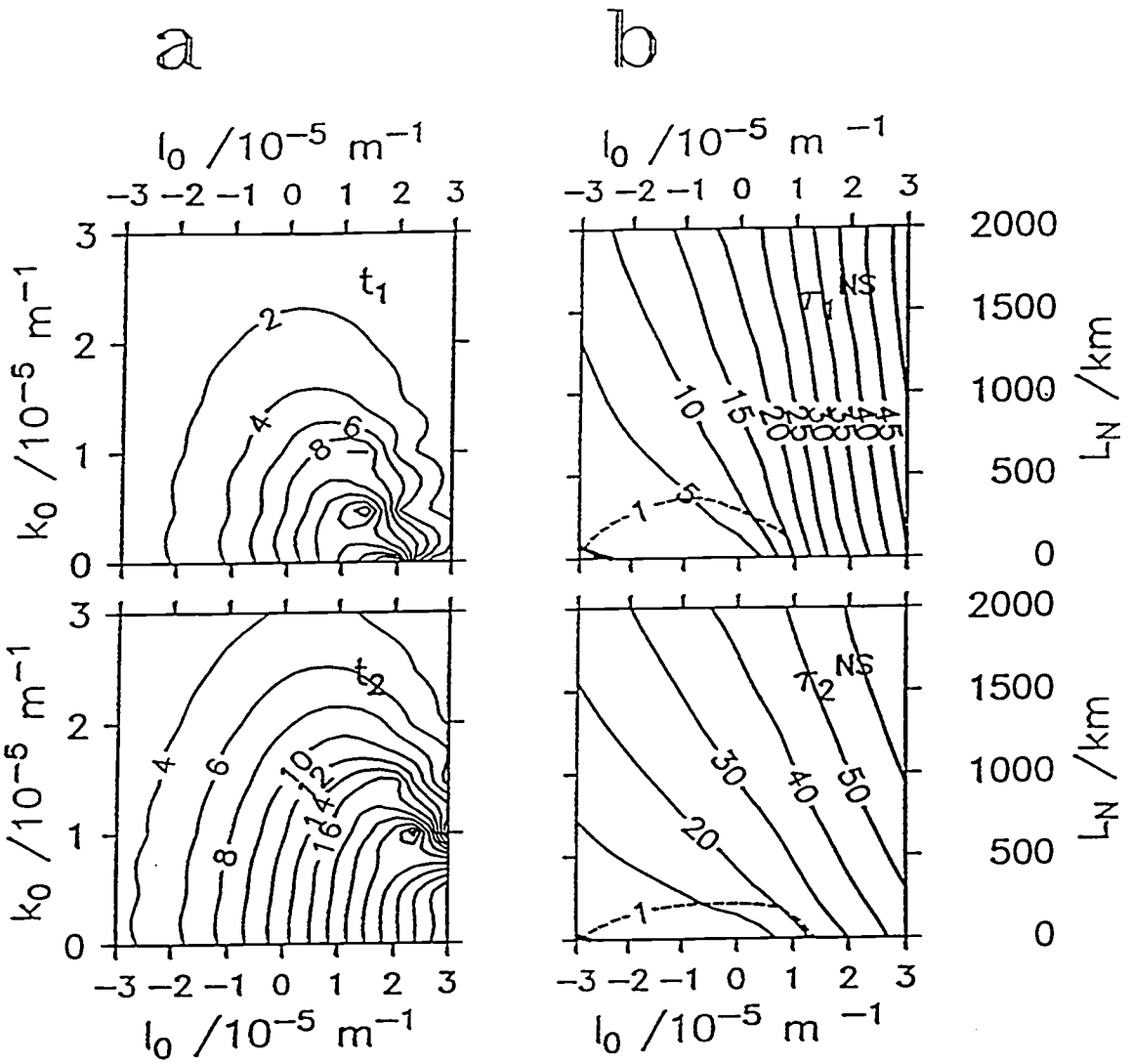

Fig. II.3. Contours of the time scales (a) t_n, and (b) τ_n^{NS}, for n = 1 and 2, for the stratification profile defined by equation (35), with H_{mix}= 150 m. at 50^{0}N. Note τ_n^{NS} is plotted as a function of initial wavenumber l_0 and northern extent L_N; t_n is plotted as a function of initial wavenumber (k_0, l_0).

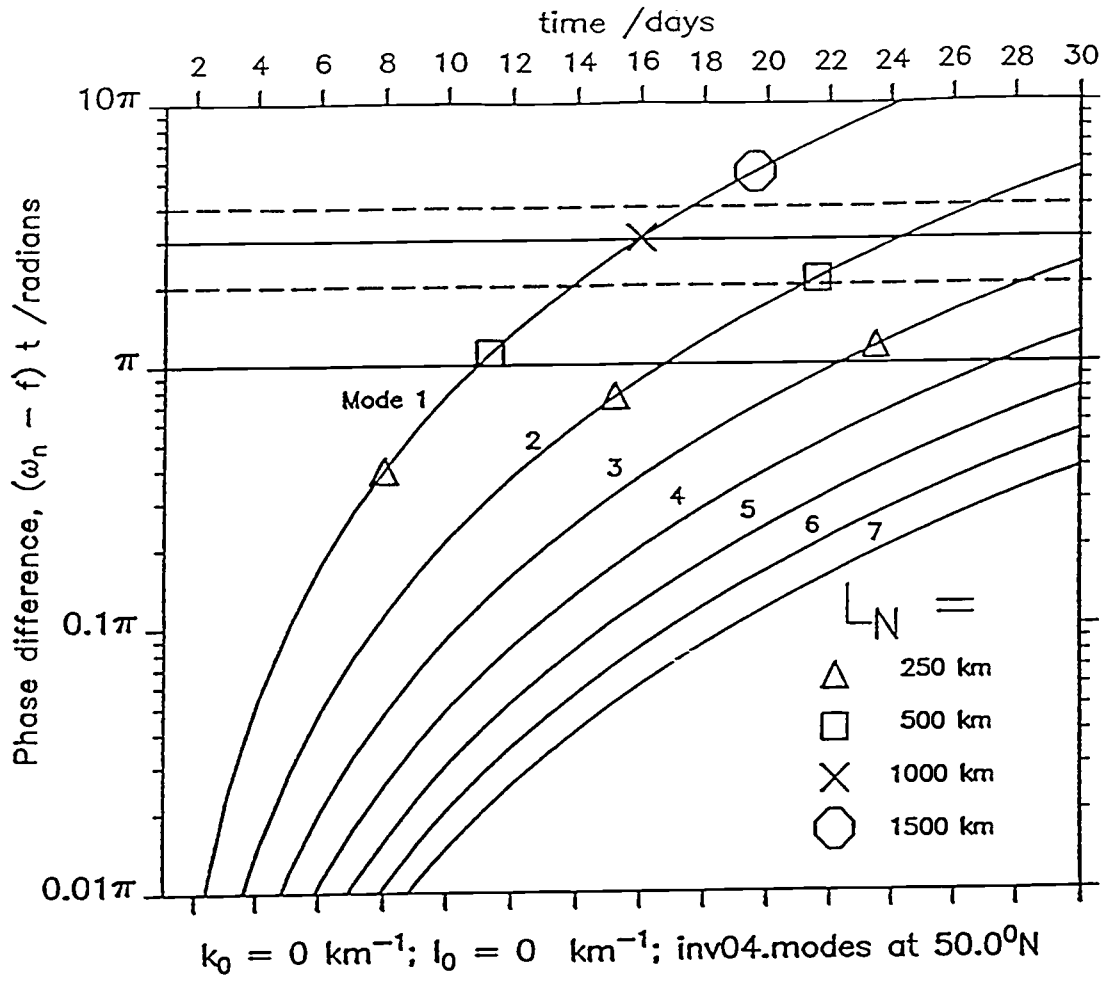

Fig. II.4. Phase difference of the seven lowest modes with a perfectly inertial current, as a function of time. In this example, $(k_0, l_0) = (0, 0)$. The horizontal solid lines denote phase differences of π and 3π, while the dashed lines denote 2π and 4π. Note that while all modes start in phase (phase difference = 0), significant phase differences develop. The intersection with the line denoting a phase difference π defines the time scales t_n. Overlaid on the phase plots are estimates of the time scale τ_n^{NS}, when a mode will have left the area, for different values of northern extent L_N.

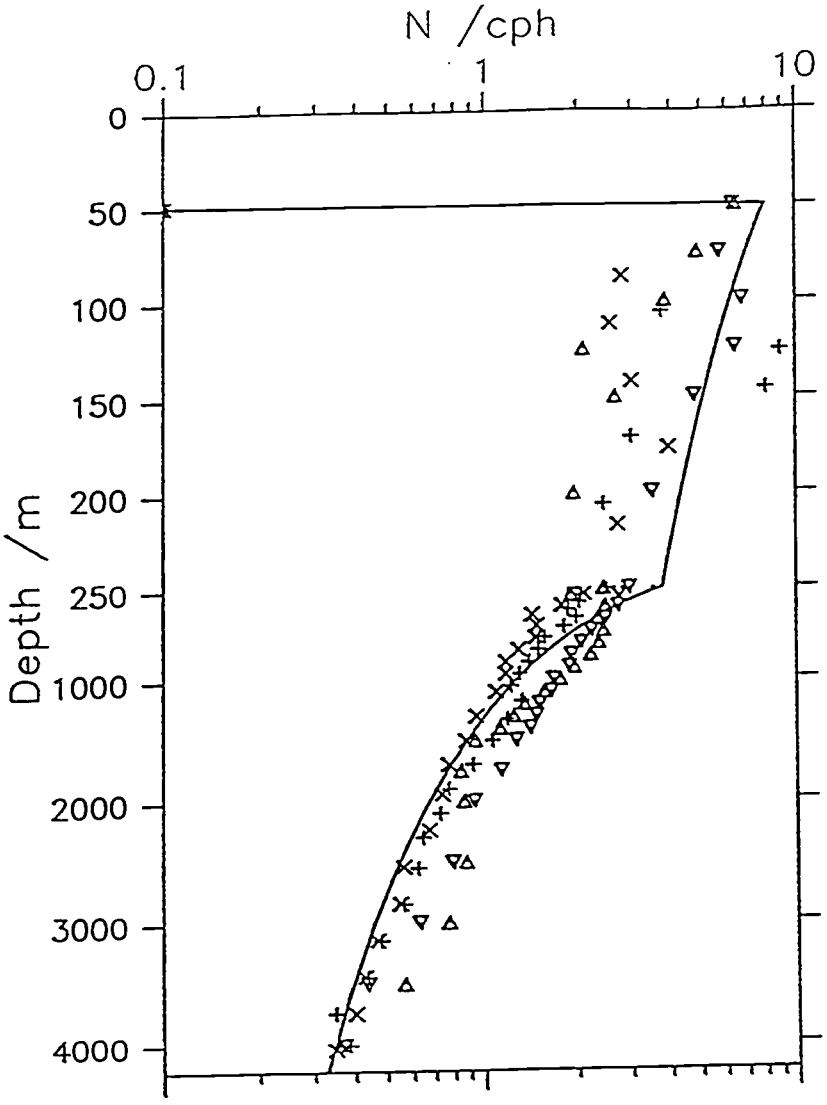

Fig. II.5. The idealized buoyancy frequency profile (solid line) defined by equation (35). For comparison, two zonally averaged profiles (Levitus, 1982) from the North Atlantic (△) and the Pacific (▽) Oceans, as well as two individual CTD casts, both from the North Pacific Ocean (+, from 47.0 ^{0}N, 135.7 ^{0}W, and ×, from 47.0 ^{0}N, 171.6 ^{0}E). Note the change of scale of the vertical axis at 250 m depth.

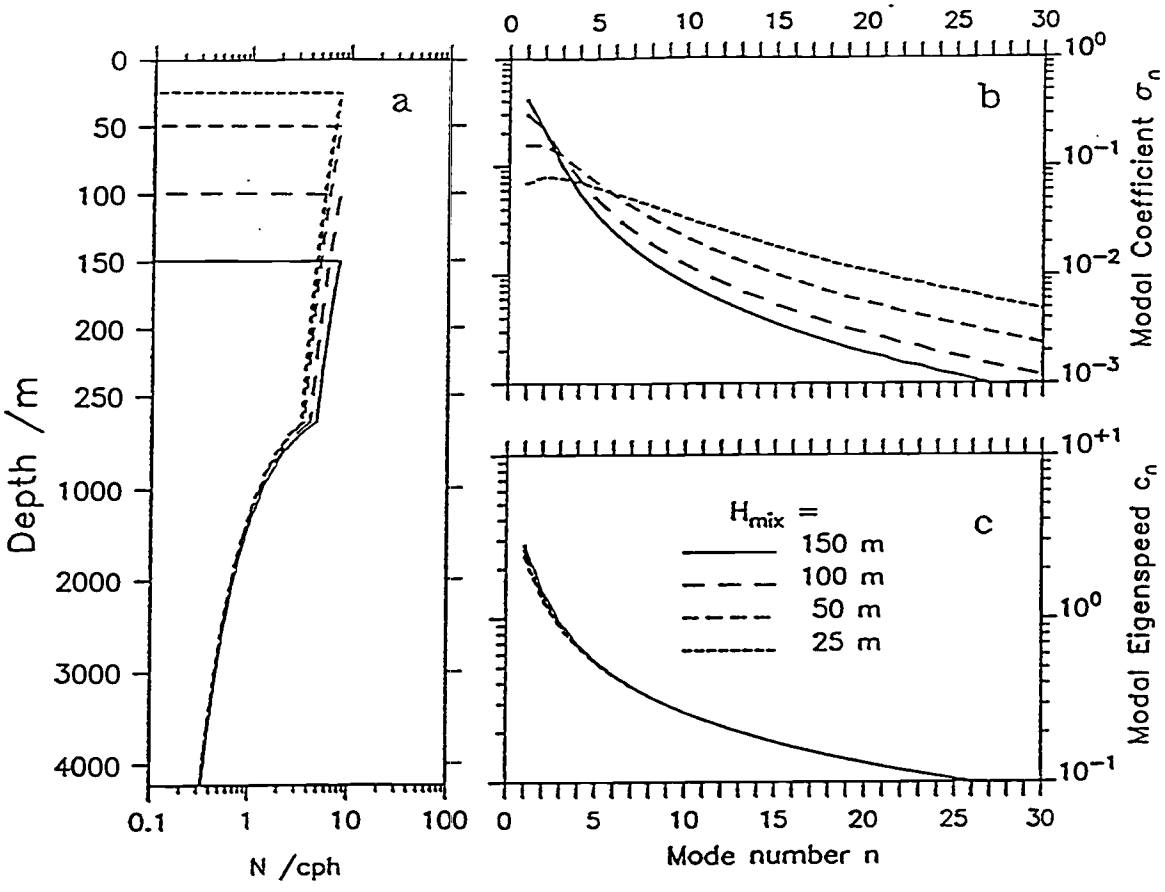

Fig. II.6. (a) Idealized profiles of buoyancy frequency as defined by equation (35) for various mixed layer depths. The corresponding values of (b) modal coefficient σ_n and (c) modal eigenspeed c_n are plotted as a function of mode number. Note that while variations in the mixed-layer depth have a strong effect on σ_n, values of c_n are virtually unchanged.

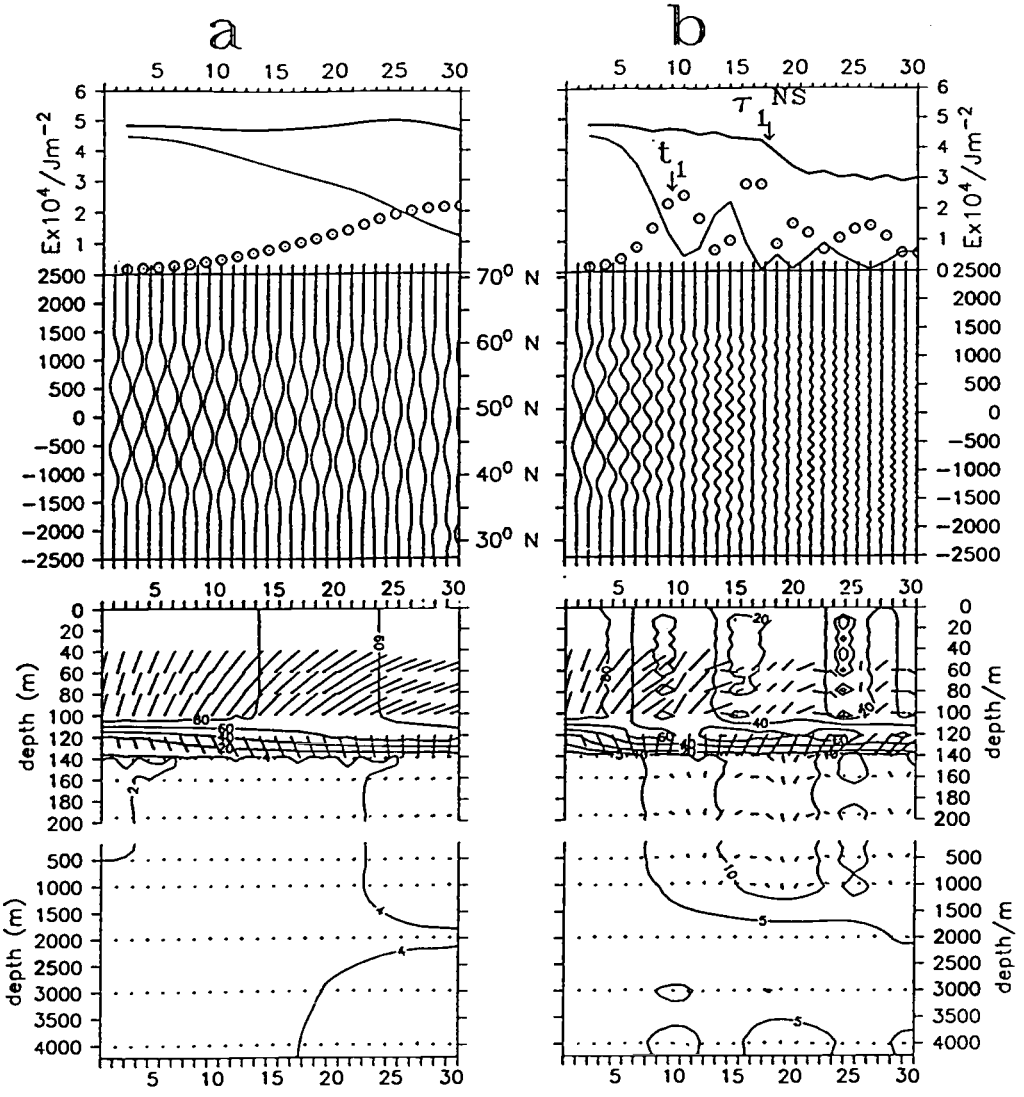

Fig. II.7. Example of model results using (a) an *f*-plane and (b) a β-plane. Both runs were initialized identically with a small southward-going meridional wavenumber l_0 = (-200 km)$^{-1}$. The top panels display E_T (heavy line), E_{ML} (light line), and E_{PC} (dotted line), at y = 0, as a function of time. The middle panels display the u component of mixed-layer current as a function of latitude and time. The bottom panel displays inertially backrotated current vectors sampled at y = 0 as a function of depth and time. Superimposed on the stick-diagrams are contours of the current speed in cm s^{-1}.

Fig. II.8. HKE as a function of time for various model runs at $y = 0$. Shown are E_T (heavy line), E_{ML} (light line) and E_{PC} (dotted line). The initial wavenumber (k_0, l_0) in the top four rows was (0, -0.75×10^{-5} m^{-1}) (southward going) and in the bottom row was (0, $+0.75 \times 10^{-5}$ m^{-1}) (northward going). The value of H_{mix} varies for each row from 25 to 150 m; the northern extent L_N,varies for each column from 250 to 1000 km. The time-scales t_n and τ_n^{NS} (section 3) are shown for modes 1 and 2. (Note the superscript "NS" has been dropped for clarity.)

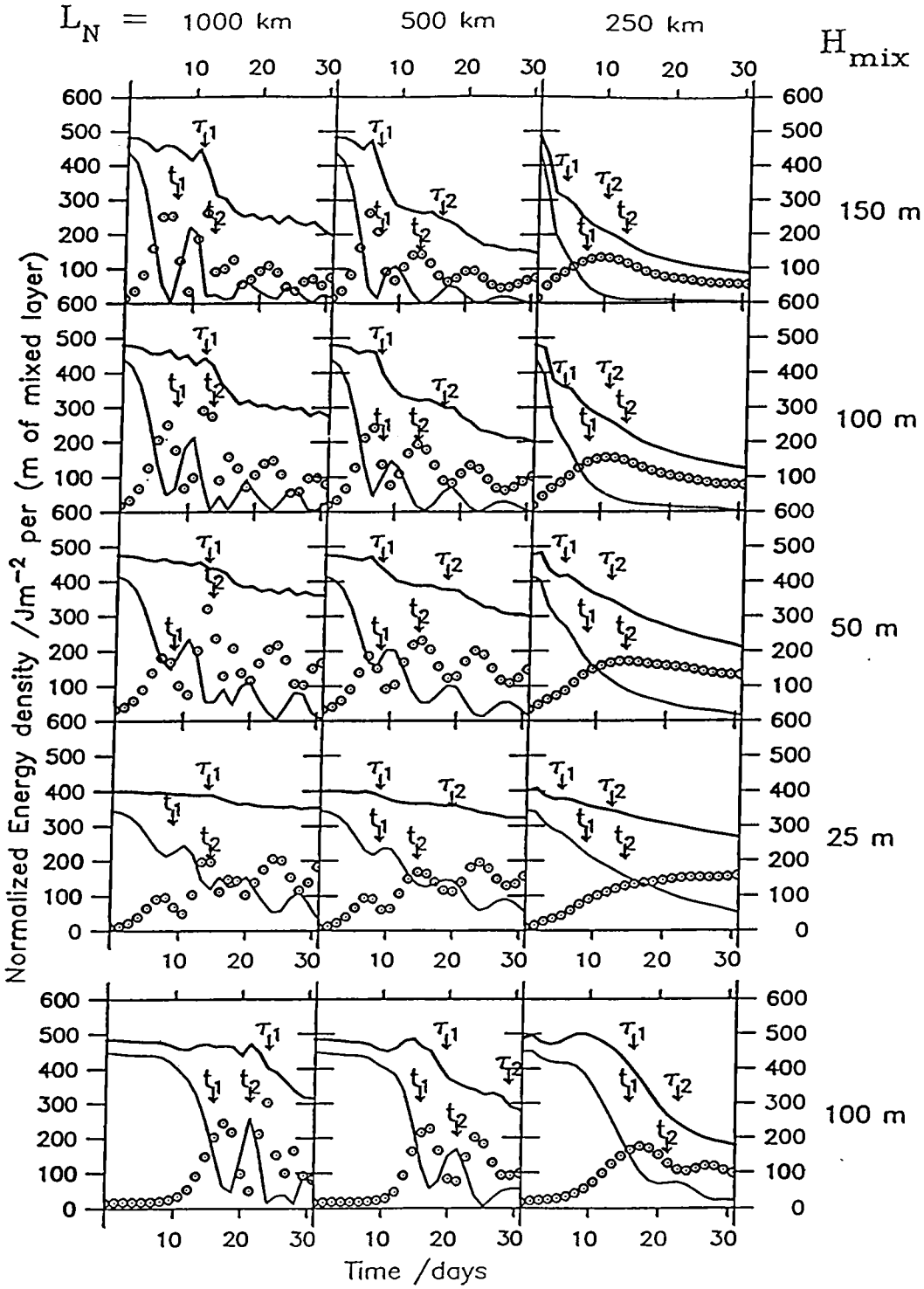
L_N = 1000 km
500 km
250 km
H_{mix} =
150 m
100 m
50 m
25 m
100 m
Normalized Energy density /Jm^{-2} per (m of mixed layer)
Time /days

Fig. II.9. Backrotated relative phases at selected depths, computed from the same model-runs displayed in Fig. II8, shown in the same order. The mixed-layer phase is shown with a solid line, and the phase at regular intervals below the mixed-layer is shown by different symbols. Displayed are estimates of the current vector's phase at the mixed layer (solid line), and approximately 10 meters (+), 20 meters (△), and 50 meters (⊙) below the base of the mixed-layer. A horizontal line denotes a perfectly inertial frequency, a positive slope denotes superinertial frequency. A key for the frequencies is provided on the bottom left corner.

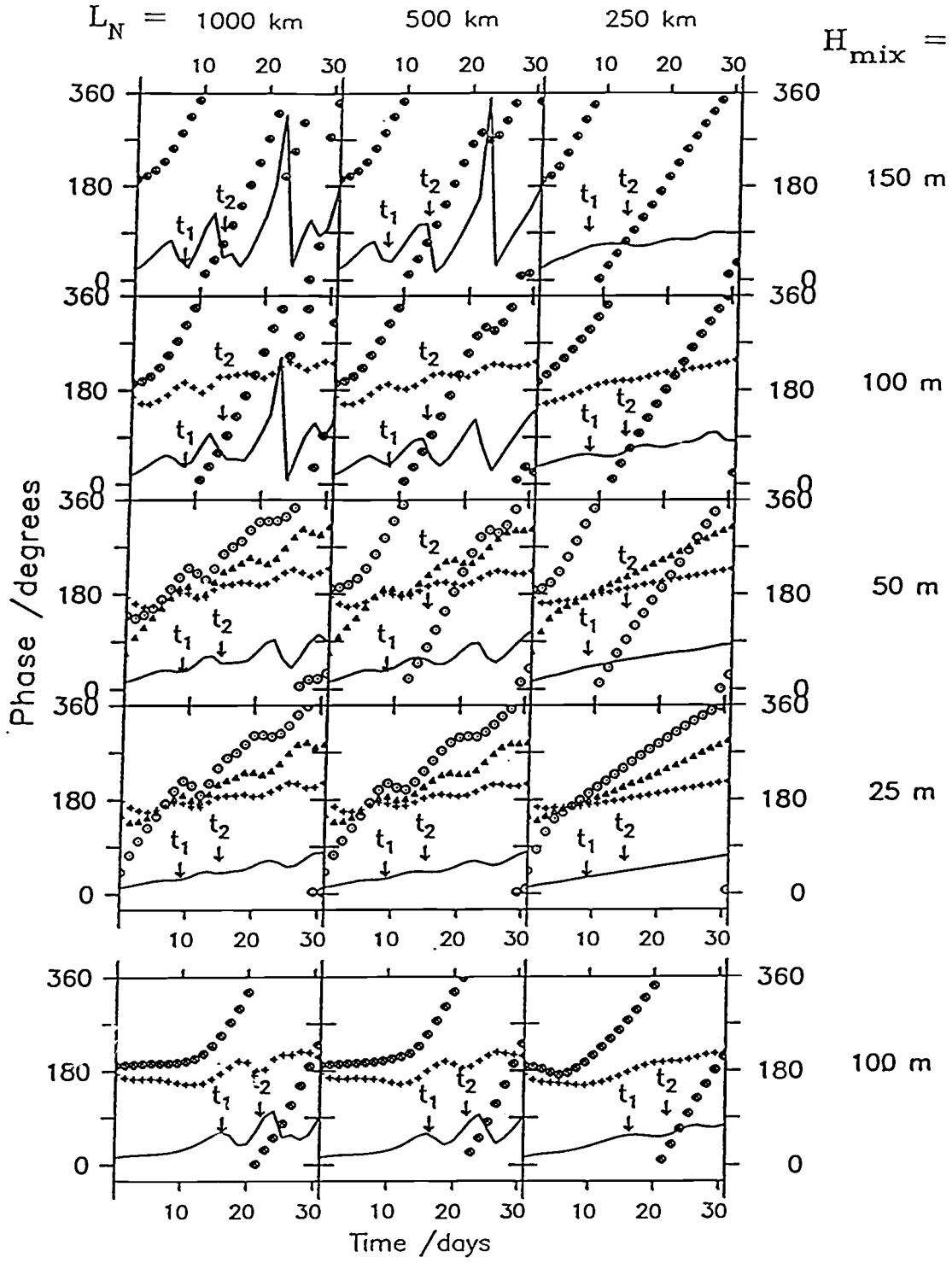
L_N = 1000 km
500 km
250 km
H_{mix} =
150 m
100 m
50 m
25 m
100 m
Phase /degrees
Time /days
t_1
t_2

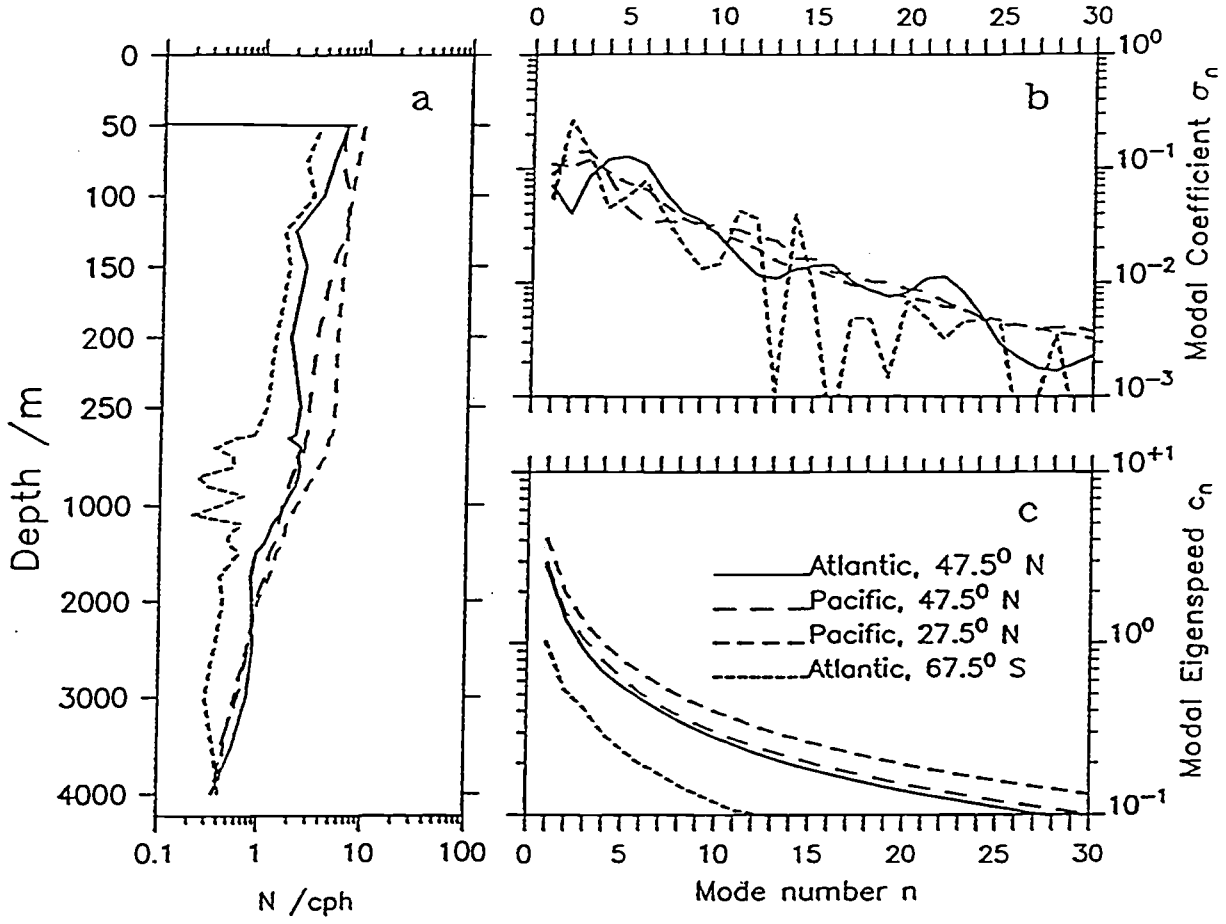

Fig. II.10. As in Fig. II6, but for historical hydrographic profiles. Note that the structure of the stratification profiles affect the modal coefficients σ_n, but not the eigenspeeds. Significant eigenspeed changes are correlated with the overall strength of the stratification--high stratification results in high eigenspeeds.

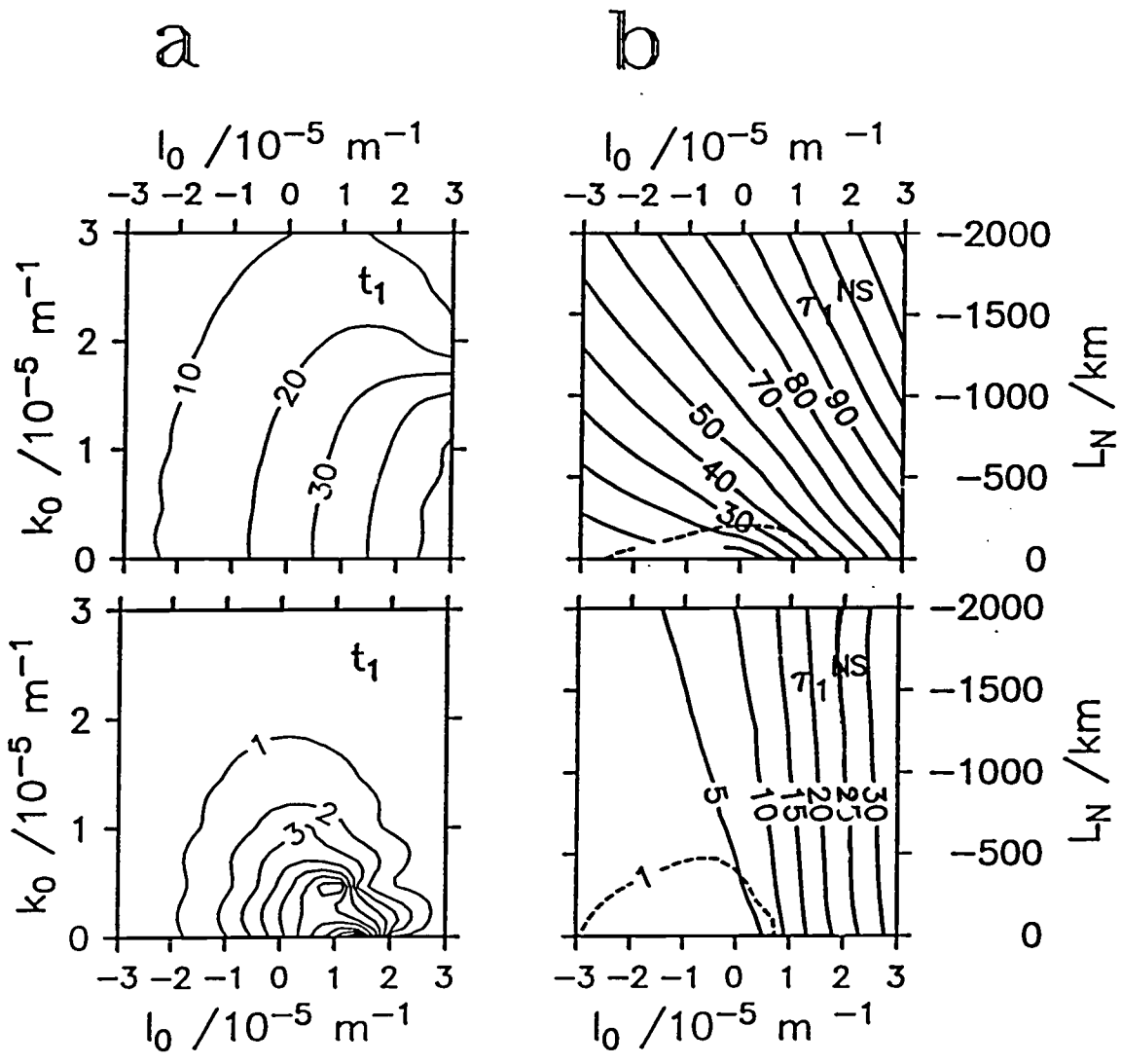

Fig. II.11. Contours of time scales t_1 and τ_1^{NS} in days, calculated for the extreme stratification profiles at 67.5^{0}S (top panels) and at 27.5^{0}N (bottom panels). The format of this figure is as in Fig. II.3.

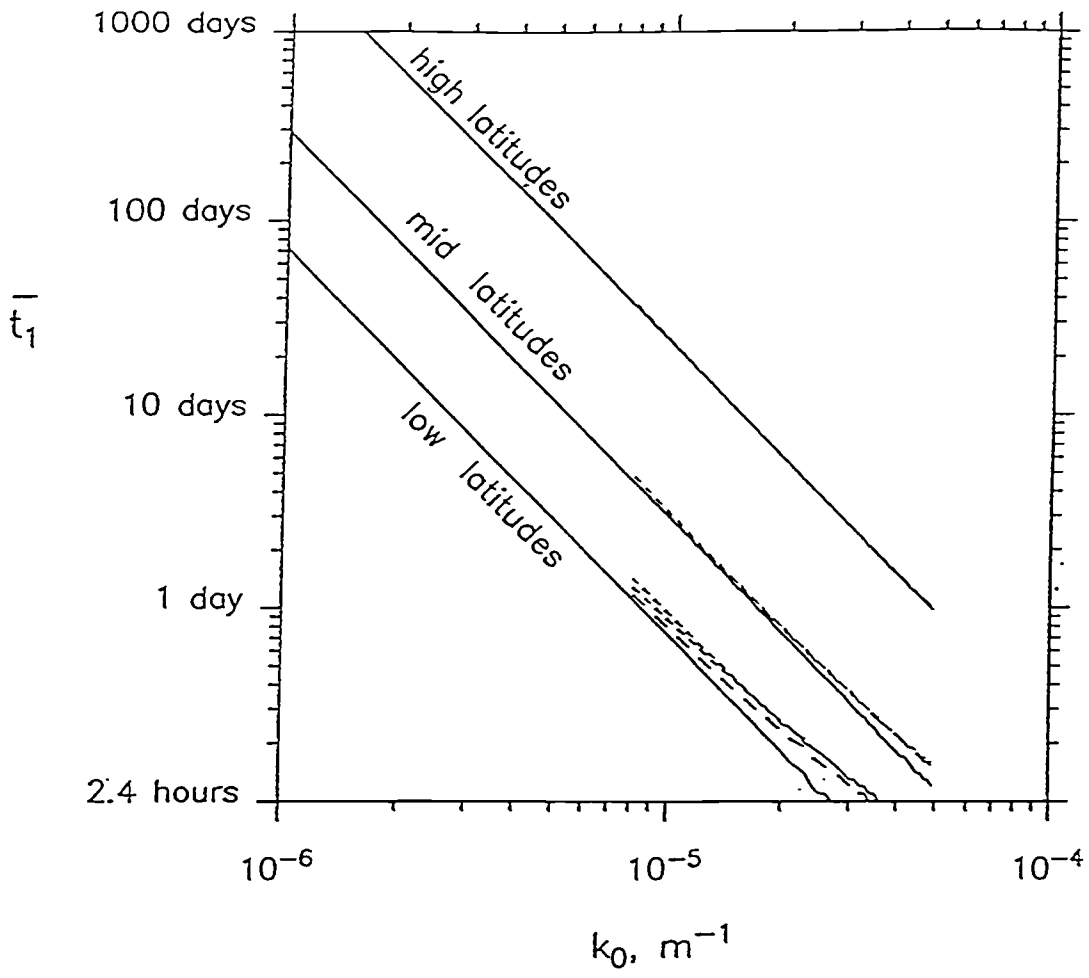

Fig. II.12. Time scale $\bar{t}_1$ (threshold for needing to use a three-dimensional model) as a function of initial meridional wavenumber k_0. Solid line represents the small ε approximation. Dashed lines are computations using the full dispersion relation, where the solution becomes a function of l_0. Three cases , for $l_0 = 0$ (long dashes) and for $l_0 = \pm 1 \times 10^{-5}$ m^{-1} (short dashes) are displayed. The difference between positive and negative l_0 are miniscule.

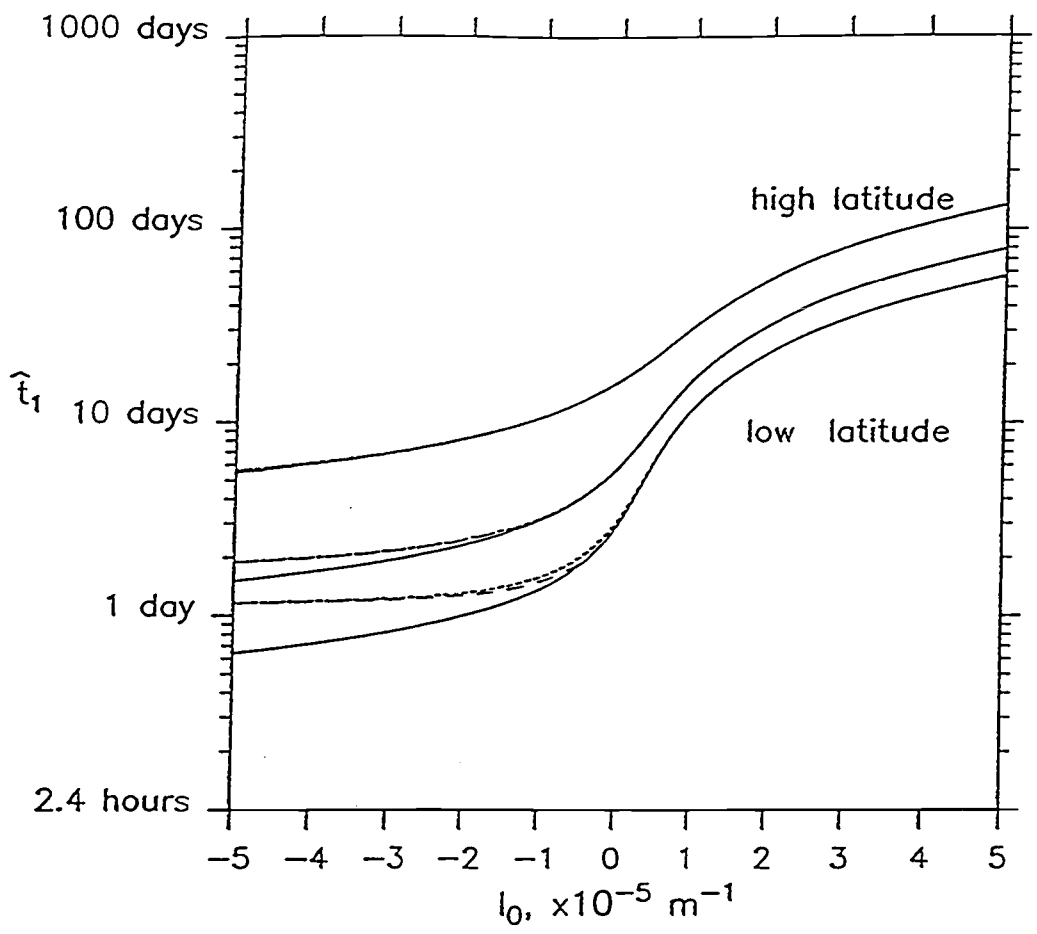

Fig. II.13. Time scale $\hat{t}_1$ (threshold for having to use a β-plane model) as a function of initial meridional wavenumber l_0 . Solid line represents the small ε approximation. Dashed lines are computations using the full dispersion relation, where the solution becomes a function of k_0. Two cases , for $k_0 = 0$ (long dashes) and for $k_0 = 1\text{x}10^{-5}$ m^{-1} (short dashes) are displayed.

Table II.1. Values of eigenspeed c_n and modal coefficient σ_n of the first five modes, calculated for the idealized stratification profiles shown in Fig. II.6

	H_{mix} = 25 m		H_{mix} = 50 m		H_{mix} = 100 m		H_{mix} = 150 m	
Mode	$c_n(ms^{-1})$	σ_n	$c_n(ms^{-1})$	σ_n	$c_n(ms^{-1})$	σ_n	$c_n(ms^{-1})$	σ_n
1	2.35	0.07	2.45	0.15	2.63	0.30	2.82	0.42
2	1.28	0.08	1.34	0.15	1.42	0.21	1.47	0.21
3	0.87	0.08	0.90	0.12	0.94	0.12	0.95	0.10
4	0.66	0.07	0.67	0.09	0.69	0.07	0.70	0.06
5	0.53	0.06	0.54	0.07	0.54	0.05	0.55	0.03

Table II.2. Values of eigenspeed c_n and modal coefficient σ_n of the first five modes, calculated for the a number of zonally averaged stratification profiles from the Atlantic Ocean.

Lat.	47.5^{0}N		27.5^{0}N		32.5^{0}S		67.5^{0}S	
Mode	$c_n(ms^{-1})$	σ_n	$c_n(ms^{-1})$	σ_n	$c_n(ms^{-1})$	σ_n	$c_n(ms^{-1})$	σ_n
1	2.79	0.07	3.78	0.09	3.61	0.07	1.02	0.05
2	1.40	0.05	1.65	0.11	1.76	0.08	0.53	0.26
3	0.92	0.08	1.20	0.17	1.19	0.07	0.30	0.14
4	0.68	0.12	0.94	0.12	0.93	0.13	0.24	0.04
5	0.56	0.13	0.74	0.06	0.75	0.11	0.20	0.06

Table II.3. Values of eigenspeed c_n and modal coefficient σ_n of the first five modes, calculated for the a number of zonally averaged stratification profiles from the Pacific Ocean.

	47.5°N		27.5°N		32.5°S		57.5°S	
Mode	$c_n(ms^{-1})$	σ_n	$c_n(ms^{-1})$	σ_n	$c_n(ms^{-1})$	σ_n	$c_n(ms^{-1})$	σ_n
1	2.94	0.09	4.11	0.11	3.66	0.08	2.56	0.06
2	1.52	0.14	1.98	0.11	1.80	0.14	1.26	0.04
3	1.05	0.14	1.34	0.12	1.26	0.06	0.84	0.06
4	0.80	0.08	1.01	0.09	0.93	0.06	0.64	0.06
5	0.63	0.04	0.81	0.07	0.75	0.09	0.51	0.08

II.7. References

Anderson, D. L., and A. E. Gill, 1979: Beta Dispersion of Inertial Waves. *J. Geophys. Res.*, **84**, 1836-1842.

Bell, T., 1978: Radiation damping of inertial oscillations in the upper ocean. *J. Fluid Mech.*, **88**, 2, 289-308.

Day, C. G. and F. Webster, 1965: Some current measurements in the Sargasso Sea. *Deep-Sea Res.*, **12**, 805-814.

D'Asaro, E., 1985: The Energy Flux From the Wind to Near-Inertial Motions in the Surface Mixed Layer. *J. Phys. Oceanogr.*, **15**,1043-1059.

D'Asaro, E., 1989: The Decay of Wind-Forced Mixed Layer Inertial Oscillations Due to the Beta Effect. *J. Geophys. Res.*, **94**, 2045-2056.

Gill, A. E., 1984: On the Behavior of Internal Waves in the Wakes of Storms. *J. Phys. Oceanogr.*, **14**, 1129-1151.

Gill, A. E., 1982: Atmosphere-Ocean Dynamics, Academic Press, 346-353.

Greatbatch, R. J., 1983: On the response of the ocean to a moving storm: The non-linear dynamics. *J. Phys. Oceanogr.*, **13**, pp. 357-367.

Greatbatch, R. J., 1984: On the response of the Ocean to a moving storm: Parameters and Scales. *J. Phys. Oceanogr.*, **14**, pp. 59-78.

Higdon, R., L., 1993: Radiation Boundary Conditions for Dispersive Waves. to appear in *SIAM J. Numerical Analysis.*

Hunkins, K., 1967: Inertial Oscillations of Fletcher's Ice Island (T-3). *J. Geophys. Res.*, **72**, 1165-1174.

Kundu, P. K., 1976: An Analysis of Inertial Oscillations Observed Near Oregon Coast. *J. Phys. Oceanogr.*, **6**, 879-893.

Kundu, P. K., 1986: A Two-Dimensional Model of Inertial Oscillations Generated by a Propagating Wind-Field. *J. Phys. Oceanogr.*, **16**, 1399-1411.

Kundu, P. K., 1992: On Internal Waves Generated by Propagating Wind-Stress. *(Submitted for publication, 30 Sept. 1992).*

Kundu, P. K., and R. E. Thomson, 1985: Inertial Oscillations Due to a Moving Front. *J. Phys. Oceanogr.*, **15**, 1076-1084.

Lacombe, H., and J. Gonella, 1964: Oscillations d'inertie des masses d' eau en Mediterranée occidentale. *C. r. hebd. Séanc. Acad. Sci.,Paris,* **259**, 2487-2490.

Levitus, S., 1982: Climatological Atlas of the World Ocean. *Professional Paper 13*, National Oceanic and Atmospheric Administration, U.S. Department of Commerce, Rockville, Md.

Lighthill, J., 1978: Waves in Fluids. *Cambridge University Press*, 317-325.

Paduan, J., R. A. de Szoeke, and R. A Weller, 1989: Inertial Oscillations in the Upper Ocean During the Mixed Layer Dynamics of the Upper Ocean Experiment. *J. Geophys. Res.*, **94**, C4, 4835-4842.

Pollard, R. T., 1970: On the Generation by Winds of Inertial Waves in the Ocean. *Deep-Sea Res.*, **17**, 795-812.

Pollard, R. T., and R. C. Millard, 1970: Comparison Between Observed and Simulated Wind-Generated Inertial Oscillations. *Deep-Sea Res.*, **17**, 813-821.

Price, J. G., 1983: Internal Wave Wake of a Moving Storm. *J. Phys. Oceanog.*, **13**, 949-965.

Rubenstein, D. M., 1983: Vertical Dispersion of Inertial Waves in the Upper Ocean. *J. Geophys. Res.*, **88**, 4368-4380.

Shay, L., K., and R. L. Elsberry, 1987: Near-Inertial Ocean Current Response to Hurricane Frederic. *J. Phys. Oceanogr.*, **17**, 1249-1269.

Webster F., 1968: Observations of inertial-period motions in the deep-sea. *Rev. Geophys.*, **6**, 473-490.

III. NEAR-INERTIAL WAVE PROPAGATION INTO THE PYCNOCLINE DURING OCEAN STORMS : OBSERVATIONS AND MODEL COMPARISON

III.1. Abstract

Observations of near-inertial oscillations collected during the OCEAN-STORMS experiment, are compared with results from a three-dimensional, linear model (developed in chapter II). A slab mixed-layer model, forced by a local wind time-series, is used to isolate events of local generation; the events of October 4, 1987, January 13, 1988, and March 1988 are selected for analysis. Climatological storm-track maps are used to determine the initial horizonal wavenumbers. The comparison of the observed and current data reveals some agreement in the coarser features of the wave fields; the transfer of energy from the mixed-layer to the pycnocline occurs at time scales predicted by analytical theory. However, the amount of energy exchanged between mixed-layer and pycnocline at the predicted times is different between model and data. As for the vertical and temporal structure of the wavefields, the observed waves propagate vertically as "beams", while the modeled waves remain at the top of the pycnocline. The frequency of the modeled currents is in general the same as observed, ranging from slightly subinertial to $1.05\,f$, and the phase propagates upwards, but more detailed comparison reveals disagreements between model and data. The results are discussed in respect with the failures of the model.

III.2. Introduction

Near-inertial oscillations, characterized by circular hodographs on the horizontal plane, are a common feature in observations of horizontal velocity in the mixed layer with amplitudes that sometimes exceed 1 m s^{-1}. They commonly occur after the passage of a storm or hurricane, a fact suggesting they are wind generated. The transfer function between wind-stress and mixed-layer velocity peaks at the inertial frequency (Pollard and Millard, 1970, Paduan et al., 1989); this explains their frequent occurrence as well as their high amplitudes. Their wind generation can be successfully modeled by assuming that the mixed-layer responds to wind-stress as a solid slab (Pollard and Millard, 1970). Since the pycnocline appears to be the most probable sink of their energy, mixed-layer inertial currents may constitute a major link of kinetic energy and momentum transfer from the atmosphere to the deeper ocean. However, their generation is better understood than their decay.

After a storm, the mixed-layer inertial currents decay over a period ranging from days to weeks. There are a number of processes that have been proposed as sinks of their energy. Near-inertial waves can generate high vertical shear, thus generating turbulence that could be a major factor in dissipating the wavefield (Eriksen, 1991, Hebert and Moum, 1993). Broutman and Young (1986) and Henyey et al. (1986) have shown that high-frequency internal waves can extract energy from near-inertial waves. Bell (1978), proposed a process of generation of high frequency, high wavenumber internal gravity waves where mixed-layer currents advect undulations of the base of the mixed-layer over a stratified ocean. The mixed-layer base undulations are assumed to be created by vertical advection processes, such as turbulent eddies or Langmuir circulation.

However, most investigations have focused on the generation and radiation of near-inertial internal gravity waves as the primary process for extracting energy from the mixed-layer oscillations; a process called *inertial pumping*. A finite horizontal structure is necessary for efficient *inertial pumping* to occur. Horizontal gradients of the mixed-layer currents cause convergences and divergences in the mixed-layer vertically displacing its base; the resulting pressure gradients generate internal waves in a process that might be described as time-dependent Ekman pumping. A multitude of models have been used to describe the process. Pollard (1970) and Kundu and Thomson (1985) have advected idealized wind-stress distributions over the surface of the ocean and assumed linear dynamics; the above models made use of vertical normal modes. Gill (1984) also used vertical modes to describe the response of the ocean to mixed-layer currents; Rubenstein (1983) used a multi-layered model, with eddy diffusivity and bottom porosity; Price (1983) also used a multi-layered ocean, and looked at the response to hurricanes; Greatbatch (1983, 1984) included non-linear dynamics and investigated the effect of entrainment; Kundu (1986) included the presence of a coast, using vertical modes with vertical eddy diffusivity; Shay and Elsberry (1987) and Shay et al., 1989) concentrated on oceanic response to hurricanes. In a comprehensive analysis of his linear, two dimensional model, Gill (1984) showed that the energy transfer from the mixed-layer to the pycnocline is dependent on the horizontal wavenumber of the wind-forced mixed-layer oscillations.

Inconsistencies between the observed time scales for mixed layer inertial oscillation decay and the expected ones based on the scales of the atmospheric forcing, were resolved by consideration of meridional variation of the Coriolis parameter f due to the Earth's curvature (D' Asaro, 1989). In the previous chapter, we have modified Gill's model to incorporate a three-dimensional, β-plane geometry and initial conditions consistent with mixed layer inertial oscillations as set by a travelling atmospheric disturbance (Gill, 1982; Price, 1983; Kundu and Thomson, 1985). The model describes the generation and propagation of near-inertial internal

gravity waves from an initial condition of mixed-layer inertial oscillations. In a careful analysis of the model results, we showed that the evolution of the near-inertial currents, as measured by an Eulerian observer, can be predicted knowing the initial horizontal structure of the inertial oscillations and making use of the dispersion relation governing the propagation of each mode horizontally (chapter II).

There have been few comparisons between open ocean inertial currents and model results. Price (1983) compared observations of inertial currents in the wake of Hurricane Eloise with model results on a constant f-plane and found very good agreement. Other comparisons of model results with data at hurricane scales (Shay and Elsberry, 1987; Shay et al., 1989) were also quite satisfactory. There have been fewer model and data comparisons for cases forced by the advection of large atmospheric fronts (Krauss, 1981, Millot and Crépon, 1981, De Young and Tang, 1990) and many of them were near a coast. However, while hurricane scales are small enough to force effective inertial pumping; at large scales, associated with large fronts and storms, the β-effect is predicted to be the essential factor in generating small enough scales (D'Asaro, 1989). Comparisons at all scales seem to converge to the conclusion that while models predict reasonably well the mixed-layer inertial oscillations, they underestimate the amplitude of the pycnocline inertial waves. Is this due to the f-plane assumption of the older modelling efforts, which leads to an overestimation of the horizontal scales and inhibits pumping, or to some other physical process not well understood?

In this chapter we compare results from the β-plane model developed in chapter II, with observations of near-inertial waves collected in the North-East Pacific through 1987-1988 as part of the **OCEAN-STORMS** experiment. We evaluate the model's performance in explaining the observations. When there are discrepancies, we suggest other physical mechanisms that should be included in the model for a better reproduction of the observed wave-fields.

The OCEAN-STORMS observations and their analysis are described in section 2 of this paper. Section 3 describes the wind-forced model of slab-mixed-layer, that was used to identify strong inertial events of local generation. Estimates of the horizontal structure of the inertial oscillations set up by the selected events are presented in section 4. A short description of the model we are using is presented at section 5, and the comparison of the OCEAN-STORMS observation with the model results is made in section 6. We summarize and conclude in section 7.

III.3. Observations

III.3.*a. The C1 mooring*

The following analysis is based primarily on data collected from a single mooring deployed in the NE Pacific from August 1987 to June 1988 as a part of the OCEAN-STORMS experiment. The mooring was positioned at 47^0 25.4' N, 139^0 17.8'W, in a total water depth of 4225 m in an area chosen specifically to be far from major topographic features; the bathymetry can be considered flat for all practical purposes. The mooring contained 7 Vector Measuring Current Meters (VMCM; Inter-Ocean) in the upper ocean at 60, 80, 100, 120, 140, 160 and 195 m and 5 Aanderaa RCM-5 current meters in the deep ocean at 500, 1000, 2000, 3000 and 4000 m. The sampling rate was 15 minutes for the VMCMs and 1 hour for the Aanderaas. Besides current speed and direction the current meters recorded temperature. Five Seacats (Sea-Bird Electronics) measured temperature and conductivity at 70, 89, 109, 128 and 150 m. The two shallowest Seacats were also equipped with Digiquartz pressure sensors (Paroscientific). Three Aanderaa TR-1 thermistor chains covering the depths 206-236, 250-260, and 375-425 meters, sampled every two hours.

III.3.*b. Supporting measurements*

Other relevant meteorological and oceanographic measurements were made near the mooring by other investigators. A time-series of wind velocity was recorded at the C0 mooring (47.3°N, 139.1°W; near 18 km northwest of C1) deployed by R. Davis (Scripps Institution of Oceanography) and was kindly shared with us. The anemometer was located at a height of 4 meters, and the wind stress at the sea surface was estimated assuming a neutrally-stratified atmosphere (Smith, 1983) (Fig. III.1a).

Additional meteorological observations from ships of opportunity, the P-3 Orion aircraft, permanent buoys, other OCEAN-STORMS moorings , and ARGOS-tracked surface drifters, were compiled and combined with synoptic weather maps by Lindsay (1988). The most intense sampling was in the period from September to December 1987.

The evolution of the mixed-layer depth was tracked with an Aanderaa TR-1 thermistor chain that was attached on the W mooring located 50 km to the west of C1 (Fig. III.1c). The chain consisted of thermistors at 10 meter intervals between 9 and 109 meters from the surface. We used the temperature measured at W because the shallowest sensor on C1 was located at 60 meters, which remained below the mixed-layer until mid-November. After November an intercomparison reveals that the base of the mixed-layer was at the same depth at W and C1 (Levine et al., 1990).

Profiles of buoyancy frequency, N, were calculated for the top 500 meters using CTD casts from two cruises of the R/V *Parizeau* during September 22 to October 16, and November 24 to December 9, 1987 (Tabata, 1988). The N profiles were extended to the ocean bottom using historical data (Levitus, 1982). To approximate the time-varying stratification, the mixed-layer depth estimates at W were incorporated into the N profiles.

III.3.c. *Complex Demodulation*

The technique of complex demodulation (Perkins, 1970) was used to isolate the near-inertial signal in the velocity data. This method was combined with rotary decomposition (Gonella, 1972), to separate near-inertial signal U_- (clockwise-rotating component) from the noise U_+ (counterclockwise rotating component). If u(t) and v(t) are the zonal and meridional components of velocity respectively, then:

$$U_+(t) = \frac{1}{4T}\int_{t-2T}^{t+2T} [u(\tau) + iv(\tau)]\ e^{-i\omega_0\tau} d\tau \qquad (1)$$

$$U_{-}(t) = \frac{1}{4T}\int_{t-2T}^{t+2T} [u(\tau) + iv(\tau)]\ e^{+i\omega_0\tau} d\tau \qquad (2)$$

Both U_+ and U_- are vectors, having both amplitude and phase information. We use a boxcar window (T=64 h) to separate the local inertial peak (at 0.0614 cph) from the peak in the semidiurnal tidal band (0.08 to 0.083 cph). Since the local inertial period is not an even multiple of the sampling intervals of the current meters, we chose a demodulation frequency $\omega_0 = 0.0625$ cph that is very near the inertial frequency. The width of the main lobe of the response of the filter (0.0312 cph) is sufficient to include the local inertial frequency without significant loss of spectral power (Fig. III.2). The demodulation was applied every 32 hours, so every other record of the demodulated time-series is independent.

The frequency can be estimated from the slope in time of the demodulated phase. This is most clearly seen if the phase is first backrotated in time at the frequency difference between the demodulation and local inertial frequency, ω_0 - f, and then plotted with time. The phase of a perfectly inertial current would result in a line parallel to the time axis; a frequency higher than f would have a positive slope.

The analysis of near-inertial frequencies requires resolving frequency differences of 0.01 f. To achieve such high resolutions, conventional Fourier transform analysis would require very long record lengths, on the order of ten months. Then all the information about individual events would be lost. But complex demodulation allows us to trace these frequencies using record lengths of only a few inertial periods. None of the principles of time-series analysis is violated; the frequency resolution is the same for both a complex demodulation filter and a conventional Fourier transform. However, by assuming that each spectral band represents a single wave, complex demodulation can be used to estimate the time-varying amplitude and phase of the wave. The change of the phase with time

would accurately estimate the frequency of the wave under the single wave assumption. For example, assume a wave with a frequency $\omega = 1.01$ f. Actual resolution of the ω and f_0 peaks would demand a record length of at least 200 hours. But if we assume that there is only one wave in that band, we can determine its exact frequency by demodulating with a record length of only 4 hours.

III.3.*d. Near-inertial currents*

The observed amplitude of the near-inertial currents ($|U_I|$) in the upper ocean from 60 to 195 m depth is plotted in Fig. III.1f. A general trend readily obvious from the data is that the currents decrease in magnitude as they propagate downwards, a trend suggesting generation at the surface. The vertical propagation of waves is evident through a number of events. Note (Fig. III.1c) that no instruments were in the mixed-layer until mid-November. At each event, the mixed-layer, near-inertial currents have the largest amplitudes and are vertically homogeneous; through stratified water, the waves propagate downwards slowly as "packets" on timescales of days. In April and May, although the temperature data show clear signs of restratification, the observed currents seem to be homogeneous over the top 100 m.

III.4. The slab mixed-layer model

The near-inertial wave field observed in the ocean is a sum of waves generated locally and waves that have radiated from distant sources. In the analysis of observations at OCEAN STORMS it is important to distinguish between the two. The slab mixed-layer model (Pollard and Millard, 1970) provides a valuable tool for that purpose. It requires only a time series of wind stress and mixed-layer depth H_{mix} to provide a first order description of the local mixed-layer inertial response to wind forcing. The model assumes that the wind-stress is distributed uniformly over a horizontally-infinite, homogeneous surface layer of constant thickness H_{mix}. Since the mixed-layer is assumed to be unstratified, the only natural frequency of the system is the local value of f. Having assumed horizontal homogeneity, there are no horizontal pressure gradients that cause inertial pumping which would lead to the vertical propagation of energy out of the mixed-layer. Hence, except for destructive interference by other storm events, there is no mechanism for the decay of the inertial oscillations. To compensate for that, Pollard and Millard (1970) introduced a body (Rayleigh) friction term, so that the oscillations are damped exponentially in time; a typical e-folding time of 4 days is used here. Since its introduction, the model has been used by many investigators attempting to simulate the mixed-layer's near-inertial response to local wind forcing (e.g. Paduan et al., 1988; D' Asaro, 1989).

The results of the slab model using the wind-stress and H_{mix} observed at OCEAN STORMS are shown in Fig. III.1. The modeled speed of the inertial response in the mixed-layer is shown in Fig. III.1b; the energy flux into the mixed-layer and its integral with time were also calculated (Figs. III.1d,1e).

The model predicts several strong generation events, especially the three starting on October 4, January 13 and March 5, that will be the focus of this paper. Each of these events is also displayed on an expanded scale in Figs. III.3, 4, and 5.

The model shows that the strong (0.8 N m^{-2}), sudden wind event of 4

October forced large inertial oscillations in the mixed-layer increasing the energy abruptly by 5000 J m^{-2} (Fig. III.3d). This event seems to be an ideal candidate for study as no additional significant forcing occurred for 25 days.

The strong currents expected in December by the slab model are just an artifact of the numerical method. To produce figure III.1, we used a numerical method of solving the traditional slab model, introduced by D' Asaro (1985). One of the assumptions of the method is that the mixed layer depth varies much slower than the wind. On December 4 there is a spike on the estimate of H_{mix}, possibly due to a brief restratification period. Comparing Fig. III.1 to Fig. IV.4a (where we have not used the D'Asaro 1985 method) reveals that the strong December currents are just an artifact of the integration method.

The event beginning on 12 January is not as isolated as the October storm (Fig. III.4). From January 12 through 26 and then again starting on February 4 there were a series of forcing events which affected the mixed-layer oscillations. Looking in detail at the slab model, the January 12-13 storm infused about 5000 J m^{-2} of kinetic energy into the mixed-layer (Fig. III.4d). Then the series of storms from January 17 to 24 slowly added another 5000 J m^{-2} into the mixed-layer. The observations agree with the model, showing an increase of the amplitude of the mixed-layer oscillations between January 18 and 21 from 28 cm s^{-1} to 40 cm s^{-1}, corresponding to a jump in vertically integrated mixed-layer kinetic energy by 4000 J m^{-2} (Fig. III.4e).

However, the slab model results after the 13th of January cannot be totally trusted. The slab model solution is constructed by adding the response of each successive event. Hence, slight variations in the phase of pre-existing oscillations will significantly affect how the energy is added--constructively or destructively. The slab model assumes the frequency at a fixed location does not vary in time, but on a more realistic β-plane the frequency will vary. To determine which of the multiple forcings after 13 January significantly changed the mixed-layer energy, we examine the current meters in the mixed-layer (60 and 80 m) (Fig. III.4e). We

observe a decay of inertial oscillation amplitude by ~8 cm s^{-1} (the corresponding mixed-layer HKE decrease is 3000 J m^{-2}) on the 15 to 17 of January, followed by an amplitude increase of ~13 cm s^{-1} (an HKE increase by 5000 J m^{-2} over the next few days). Inspection of the corresponding mixed-layer phase observations (shown in next section) does not reveal any significant phase jump, so the additional forcing on those days was either in or out of phase. Thus, modeling the January event might only need the superposition of the solution of the two additional events, assuming linear dynamics; however, we will only model the response to a single forcing event of January 13.

Although March 1988 was quite a windy month, the slab model indicates that only the event of March 5 generated considerable inertial oscillations (Fig. III.5). The model indicates that about 4000 J m^{-2} was added to the mixed-layer. Another, weaker event on March 18 injected less than 1000 J m^{-2} additional energy into the mixed-layer. The event of March 24 is of small magnitude and does not seem to have an effect on the mixed-layer currents. It should be noted that the decay of the slab model energy is not expected to accurately follow the observations.

Finally, on April 2, there is a packet of inertial currents, homogeneous over 60 to 100 meters. A mixed-layer response is also predicted by the slab model. Since H_{mix} is very variable and often less than 60 m in April (restratification period), we cannot directly compare the modeled mixed-layer currents with the currents observed at 60 m. The model also predicts accurately the generation of inertial currents on May 1st, but not on May 18. Note however that on May 1 the observed mixed-layer depth is 40-60 meters, while the current meter response suggests a mixed-layer depth of more than 100 meters. Lacking any information on the actual stratification profiles, we will defer modeling the April and May events.

The near-inertial response observed during OCEAN STORMS were compared with the 10-year climatological data analyzed by D'Asaro (1985) at Ocean Weather Station P (50^0 N, 145^0 W). Both the October and March events can be considered typical of North Pacific fronts, each injecting about 5000 J m^{-2} of kinetic

energy into the mixed-layer, with impulses of energy fluxes of the order of 100 mW m^{-2}. The January forcing event, being a series of forcings injecting a total of 10000 J m^{-2} into the mixed-layer is stronger than average. The fall period (October-Dec 1987) had an average kinetic energy flux of 0.95 mW m^{-2}--less than the climatological average at station P of about 3 mW m^{-2}. The winter period (January-March 1988) was more active than average with an observed flux of 2.2 mW m^{-2} in contrast to the climatological average of about 1.8 mW m^{-2}. Overall the observed average inertial kinetic energy flux from September to May (Fig. III.1) was 1.9 mW m^{-2}. D'Asaro (1985) estimated the average flux from September to March to be ~2.0-2.5 mW m^{-2}. So, the OCEAN STORMS experiment appears to have occurred during a year in which the near-inertial forcing was typical.

III.5. Numerical Model

III.5.*a. Description*

The observed propagation of near-inertial energy at OCEAN STORMS is studied in the context of the model developed by in chapter II. This model, patterned after Gill (1984), is not directly forced by the wind stress, but is set in motion by the initial conditions. The model then tracks the horizontal and vertical propagation of near-inertial waves that result from the initial disturbance.

The model uses linear dynamics on a β-plane. The solution is analytical in depth, using vertical modes, and in x (zonal), using Fourier transforms. The propagation of each mode is solved numerically using finite differences in both y (meridional) and time. Velocity profiles are constructed by adding all the modes used, typically 20.

We assume the initial condition in the mixed-layer is set by the passage of a fast-moving atmospheric front; below the mixed-layer there is no motion initially. The oceanic response to a moving front can be described separately for each vertical mode as a function of the advection speed C of the front and the *eigenspeed* c_n of the mode (Gill, 1982; ch. 9.11). When $C < c_n$, the equation governing the horizontal radiation of the mode is elliptical, and the solution decays exponentially from the center of the storm. When $C > c_n$, the equation is hyperbolic, and the solution is a wake of near-inertial oscillations propagating behind the forcing. In this analysis we assume that $C > c_1$, and hence the equation is hyperbolic for all the modes, since $c_1 > c_n$ for all $n > 1$. The mixed-layer response occurs at a horizontal wavenumber $\kappa = f/C$ and is consistent with a near-inertial wave propagating in the direction of the storm track. Note that the quantity $2\pi/\kappa$ is called the "inertial wavelength" by Kundu (1985), while D' Asaro (1989) calls $1/\kappa$ the "advection scale" of the storm.

The model behavior is determined by the initial conditions. We consider an initial disturbance dominated by a single horizontal wavenumber of finite horizontal extent (Fig. II.1). The horizontal pattern of the initial currents is consistent with a fast moving front, which differs from the initial condition used by Gill (1984). A thorough discussion of the model as a function of initial conditions is presented in chapter II--some of the results of this study are summarized below.

The initial vertical structure, that is, constant velocity in the mixed-layer and zero velocity below, is satisfied by the summation of vertical modes. Therefore, the percent contribution of each mode to the initial velocity profile, σ_n, depends on N(z). It can be shown that σ_n also represents the percent contribution of each mode to the kinetic energy of the whole water column (Gill, 1984). The various N(z) profiles we used to calculate the mode shapes are shown in Fig. III.6a. The modal coefficients σ_n, and the modal eigenspeeds c_n are shown as function of mode numbers in Fig. III.6b and 6c respectively. Note that the shallow mixed layer in October (solid line) results in smaller relative weights σ_n for the low modes, and larger weights for the high modes, than the January and March profiles (dashed lines). The eigenspeeds of the modes however do not exhibit significant differences among the various profiles.

After t = 0, each mode begins to oscillate at a different frequency, with the lower modes having higher frequencies. The modes also begin to propagate horizontally. To a reasonable approximation, the meridional wavenumber varies in time as

$$l(t) = l_0 - \beta t \tag{3}$$

due to the β-effect. For small enough initial wavenumber l_0 (reflecting large fronts propagating fast), the term βt soon becomes larger and $|l(t)|$ starts growing. Therefore, due to the dispersion relation (equation 21 in chapter II), locally the frequency of each mode increases in time.

III.5.*b. Modal interference (beating)*

Vertical propagation of energy in the model can be explained by the differential frequency of each mode (Gill, 1984). Since each mode oscillates at a different frequency, their sum will no longer be zero below the mixed-layer after t = 0--hence, vertical propagation of energy. We define the "beating" time scale t_n when mode n will become out of phase with the high modes at frequencies near f by

$$t_n = \frac{\pi}{(\omega_n - f)} \tag{4}$$

At this time mode n will contribute to the energy below the mixed-layer. Although the details of the energy exchange cannot be explained by this simple argument, it provides a framework for interpreting the model results.

The parameters that affect these time scales are fully explored in chapter II; a few of the most relevant results are presented here. The adoption of a β-plane makes the eigenfrequency ω_n of each mode a function of time. Then, as we have describe in chapter II, the time-scales t_n become dependent on the initial wavenumbers. Smaller scale disturbances (high wavenumbers) propagate faster vertically. In an initially southward-going storm, $l_0 < 0$ the local magnitude of (l) increases rapidly in time and results in a smaller t_n than for an initial northward-going storm ($l_0 > 0$) whose local $|l|$ goes through zero before finally increasing. Hence, the timing of vertical propagation is a strong function of initial wavenumber and is an important point to consider in comparing model and observations.

III.5.*c. Horizontal departure of modes.*

After t=0 the modes propagate horizontally. If the initial condition is of finite horizontal extent, the modes will eventually propagate out of the region; lower modes propagating faster. Initially northward-going waves will refract at the turning latitude and propagate southward before leaving the area. Locally we define the time scales for mode n to leave due to meridional or zonal propagation by τ_n^{NS} and τ_n^{EW} respectively.

The propagation time scales τ_n^{NS} and τ_n^{EW} are a strong function of the initial north-south and east-west extents respectively. In general the smaller the extent of the storm, the faster the modes leave. When mode 1 leaves, the energy in the mixed-layer will decrease; the amount of the decay depends on the stratification. On the other hand the energy below the mixed-layer will often increase, as the contribution from mode 1 that was needed to set the initial velocity below the mixed-layer to zero will be absent.

III.5.*d. Initial conditions at Ocean Storms*

The initial horizontal wavenumbers generated in the mixed-layer during OCEAN STORMS were estimated from the advection velocity of the atmospheric fronts. The speed C and direction ϑ of the storm were estimated from plots of storm tracks showing the daily position of each front (Lindsay, 1988). Crude estimates of the initial wavenumber vector (k_0, l_0) were made for each of the 3 storm events, where k_0 = (f /C) cos ϑ, l_0 = (f /C) sin ϑ (Table III.1). In all 3 events the storms were propagating to the NE with speeds exceeding 10 m s^{-1}, resulting in initial wavelengths significantly larger than 500 km. Two additional storm tracks from the series of storms from January 15 to 19 indicated fast fronts moving at 20 and 35 m/s to the NE with a corresponding small horizontal wavenumber.

Other estimates of horizontal wavenumber were made for the OCEAN-STORMS experiment. D' Asaro (1993) used surface drifter data to estimate the horizontal structure of the mixed-layer near-inertial currents throughout the October event. His estimates of both k_0 and l_0 ranged near 0.0025 km^{-1}, both positive, suggesting northeast propagation of the generating storm. Qi et al. (1993) combined mooring data with a ray-tracing method to estimate wavenumber. Our estimates are consistent with those of the above investigators. The initial amplitude of the currents in the mixed-layer was set in the model to fit the observations.

III.6. Observations and Model Comparison

We compare the observations with the modeled response for a variety of initial conditions. All 3 events are shown together to emphasize differences and similarities. To be consistent in comparing the model results with the observations, the model was sampled at 47.5^0 N at the same depths where the current meters were positioned. The modeled data underwent exactly the same analysis as the moored observations. First we present a general picture of the response by looking at the temporal change of the vertically integrated energy in the mixed-layer, pycnocline and deep ocean. This permits an overall comparison of observations with the model and clearly demonstrates the effect of different initial conditions on the model behavior. Next the detailed vertical structure is examined; at each depth the amplitude and phase of the observations and model are compared.

III.6.*a. Energy Comparison*

The observed horizontal kinetic energy (HKE) is shown in the top panels of Fig. III.7 for the 3 events. The HKE of the whole water column (E_T), of the mixed-layer (E_{ML}), and of the pycnocline (E_{PC}) are plotted. Here the pycnocline is defined as the layer from below the mixed-layer to 500 m for all events. This definition is based primarily on availability of observations. The mixed-layer energy is estimated assuming a constant velocity throughout the mixed-layer. The October estimate of E_{ML} from the surface to 35 m is based on nearby surface drifters (D' Asaro, 1993) as there were no current meters in the mixed-layer at this time. In January and March the mixed-layer extended to 95 and 110 m respectively and contained at least 2 current meters.

After the storm of 4 October the mixed-layer energy began to decrease very soon, at least by 8 October when the first mixed-layer data are available (Fig. III.7a_i). The decrease was steady until 22 October when virtually no energy

remained. Coincident with this decrease was an increase in the E_{PC} that began to rise almost immediately after the storm, reaching a peak on 18 October before decreasing to very low levels by 30 October. In estimating E_{PC} we did not include the current meter at 60 m; the near inertial oscillations at that depth could be contaminated by vertical advection of the wavefield by the internal tide.

The multiple forcing event of the January storm resulted in a more complicated mixed-layer response. E_{ML} increased initially due to the 12 January event (Fig. III.7b_i). The rapid decay on 15-16 January was due to additional forcing that added destructively to the existing currents. The large increase during the following few days was apparently due to a forcing event that was in phase with existing currents and added constructively. Unlike the October event, E_{PC} did not increase initially; it took about 7 days before the increase began and 8 more days until reaching its maximum value. The variability of E_T after January 13 follows very closely the variability of E_{ML}.

After the March 5 event, E_{ML} remained constant for about 7 days before beginning to decrease (Fig. III.c_i). Similar to the January response the increase in E_{PC} is coincident with the decrease of E_{ML}. E_{PC} peaks 16 days after the event, reaching a maximum of 2500 Jm^{-2}, which is 50-60% of the initial E_{ML} injected by the wind. E_T, on the other hand, remains constant until March 20, and then decays progressively to reach background levels by the end of the month.

During the January and March events, E_T is approximately equal to the sum of E_{ML} and E_{PC}, since nearly all the energy is concentrated in the upper ocean. In contrast, in October there is a significant amount of energy below the pycnocline even before the wind-event (Fig. III.7a_i).

The model results for the 3 events are also shown in Fig. III.7. The initial horizontal wavenumber of the mixed-layer currents was determined from the storm front velocity as presented in Table III.1. The horizontal extent of the storm was assumed to be infinite in east-west extent and extend 500 km to the north; there was no straightforward way to determine these parameters *a priori* from observations.

The main features of the model results are similar for the 3 events, since all events were forced by fronts propagating to the NE. However, the magnitude of the responses differed in proportion to the forcing of each event. The mixed-layer energy remained relatively constant for about 8 days before decreasing. The decrease can be explained by the "beating" of modes 1 (highest frequency) and 2 with the other modes closer to *f*. The time scale characterizing the first significant exchange of energy between mixed-layer and pycnocline is t_1; however, a greater change occurs when mode 2 beats at time t_2 (Fig. III.7.a_{ii},b_{ii},c_{ii}).

The magnitude of the decrease of E_{ML} in the model at time t_n depends on the relative contribution of mode n to the total solution. At time t_1, E_{ML} will decrease to $(1-2\sigma_1)^2$ of its initial value (Gill, 1984). The contribution of mode 1 to the initial mixed-layer velocity is $\sigma_1 \approx 10$ % for October, compared to 20% for January and March (Fig. III.6). The difference is due to differences in N(z); there was a shallower mixed-layer in October. Thus, we expect E_{ML} to decay by 36% at time t_1 during the October event, and by 64% for the other two events, a prediction certified by the model runs (Fig. III.7a_{ii},b_{ii},c_{ii}). However, the maximum increase of E_{PC} and decrease of E_{ML} occurs after time t_2, since mode 2 is more energetic than mode 1 for all three stratification profiles ($\sigma_2 \approx 2\sigma_1$)(Fig. III.6).

The 7-day delay for the coincident E_{ML} decrease and E_{PC} increase observed during the January and March events is reproduced by the model, discounting the more complicated forcing in January. The timing of the October response clearly does not follow the model, with the observed energy propagating from the mixed-layer into the pycnocline almost immediately after the forcing event. However, the energy levels predicted for E_{PC} are in general similar to the observed for all three events, including October. Furthermore, the analytically estimated time scales t_1 and t_2 seem to characterize the propagation of energy from the mixed-layer to the pycnocline, *for all three events*. The observed decrease in E_T , occurs at time-scales predicted by the model, but the magnitude of the decreases are larger in the observations.

To explore possible reasons for the differences between the modelled results and observations, a series of additional model runs were made to examine the effect of initial wavenumbers and horizontal extent on the solution. The time scales t_1 and t_2 are sensitive to the initial meridional wavenumber l_0; smaller scale disturbances propagate faster in the vertical resulting in smaller t_1 and t_2. To examine the effect of the initial wavenumber on the model results, the sign of l_0 was reversed--mimicking a storm front propagating to the SE (Fig. III.7, a_{iii},b_{iii},c_{iii}). In these cases the time scale of the "beating" t_1 is much reduced, resulting in faster propagation from the mixed-layer into the pycnocline. This is because the magnitude of l increases faster if l_0 is negative (1). Clearly the modeled October storm now looks more like the observations. However, SE propagation is not consistent with realistic initial conditions (D'Asaro, 1993, Qi, 1993, section 5b of this chapter). The timing of the observed energy exchange between mixed layer and pycnocline for the January and March events is consistent with storms propagating to the NE (cases b_{ii}, c_{ii}).

The effect of a finite north-south extent used in these model runs is to reduce the total energy in the water column as modes propagate away. Model runs with northern extents of L_N = 250, 500 and 1000 km are displayed in Fig. III.8. The results are as expected from chapter II. Note that the time-scales t_1 and t_2 are not functions of extent, and only the time scale τ_1^{NS} grows with increasing extent. The mixed-layer decays smoothly for L_N = 250, the lower modes propagating away before beating with the high modes. For L_N = 1000 km, the beating at t_1 is more pronounced than for L_N = 500 km, and the time-scale τ_1^{NS} seems to be longer than the observed by the decay of the total kinetic energy E_T (Fig. III.8a_i,b_i,c_i). If we assume that the first major decrease in the observed E_T occurs at τ_1^{NS}, the second decrease at τ_2^{NS} etc., then we can treat the northern extent as a parameter and find a value that is consistent with the observations. For both October and March events, the decay of E_T seem to take place in two stages. The observed decay time scales suggest that the directly wind-forced mixed-layer oscillations extended between 500

and 1000 km to the north of C1. The January picture is not so clear, due to the multiple forcing of the mixed layer; however, a northern extent of 250 km is in the range of possibilities.

These estimates of L_N are based only on comparing the time-scales of the observed E_T decay to the model predictions. However, considering the amount of E_T decay reveals discrepancies between the model and the data. The observed E_T decay is much greater than would be expected if the decay were attributed to horizontal propagation of modes away from the area. The modelled E_T decays by σ_n when mode n leaves. The observed large decays in all three events, suggests that we underestimated the magnitude of the low modes in the solution.

A finite zonal extent will also affect the solution. For the NE moving front in the 3 events examined here a finite western extent L_W of greater than 900 km would hardly affect the solution at all during the first 30 days. If a smaller extent were used, then mode 1, the fastest, would leave sooner and reduce the total energy E_T. The absence of mode 1 would also result in reapportioning the energy--decreasing E_{ML} while increasing E_{PC}. The model was run for various values of L_W. The results, in terms of energy radiated into the pycnocline, look very much like Fig. III.8a_{ii},b_{ii}, c_{ii}: E_{PC} never increases enough to improve the agreement with the observations. The reason is that since the low modes leave early, they never come into constructive interference with the higher modes into the pycnocline, so as to produce high E_{PC} values. Quantitatively, we show in appendix I that while the decrease of E_{ML} associated with mode 1 beating is by a factor of $(1-2\sigma_1)^2$, the E_{ML} decrease associated with mode 1 departing is only $1-\sigma_1(2-\sigma_1)$ (we follow the convention of chapter II where σ_1 is the percent contribution of mode 1 to the initial mixed-layer velocity). As a result, we don't expect finite extent to be the reason for the fast pumping observed during the October event. The magnitude of modeled E_{PC} suggests that modal interference and not departure is the major mechanism of vertical propagation of energy for the January and March events also.

III.6.*b. Possible scenarios*

In the previous section the comparison between the observed and modelled HKE revealed some similarities and differences in the three events. The observed time-scales characterizing the evolution of the wave fields agree with the analytically estimated t_1 and t_2, based on estimates of the initial wavenumber. The events of January and March show considerable agreement between model and data, although the model slightly underestimates E_{PC} at t_1 and overestimates it at t_2. Also, the amount of decay of E_T is underestimated by the model. The October event offers the major discrepancy between model and data, as the inertial pumping seems to begin too quickly and E_{PC} peaks too soon. Assuming the relative weighing of the modes in the model is correct and linear dynamics dominate, southward initial propagation seem to explain better the observed evolution for October. However,other investigations (Qi, 1993; D'Asaro, 1993), as well as our estimation of $l_{0,}$, suggest northward propagation. We explored several hypotheses to determine the reason for the difference observed between data and model for the October event.

One possibility is the effect of the mesoscale horizontal shear on the near-inertial wavefield. Investigating that possibility, D' Asaro et al. (1993) compared the spatial scales of the near-inertial field with the low-frequency relative vorticity field, both derived from surface drifter observations. The vertical component of relative vorticity ζ has an order of magnitude of $0.02\,f$, high enough to affect the horizontal propagation of the near-inertial waves (Kunze,1985) and inertial pumping (Wang,1991). However, D'Asaro et al. (1993) argues that since the near-inertial wave field does not have same spatial scales as ζ, the evolution of the waves was not dominated by the relative vorticity field. Thus, the interactions of the near-inertial field with the background mean flow does not appear to explain the discrepancy between observations and model in the timing of the inertial pumping.

Another possibility is that the model underestimates the relative weight of the first and second modes. For both the January and March events, the observed energy pumped into the pycnocline peaks at time t_1 and is larger than predicted by the model. The modeled E_{PC} does not reach the observed levels until time t_2. The fact that the model peak at t_1 is not as large as observed suggests that the model underestimates the contribution of mode 1, i.e. σ_1, to the wavefield. This hypothesis is further enforced by the large decrease of E_T (Fig. III.c_i) at time τ_1 during the March event (Fig. III.c_{ii}). The underestimation of σ_1, may also explain the discrepancy observed in October. Note that the peak in the observed E_{PC} as well as the decay of E_{ML} (Fig. III.7a_i) take place at time t_1 rather than t_2, as predicted by the model for a NE propagating front (Fig. III.7a_i, 7a_{ii}). Also, the observed total energy E_T decays near time τ_1 by 20-30% of the initial value. Hence, the discrepancy between model and observations for all three events might be explained if mode 1 were 2-3 times more heavily weighted.

What would affect the relative weight of mode 1? The value of σ_1 is determined by assuming that the initial condition is a current confined in the mixed layer. If the stress penetrates into the pycnocline, the initial current would extend below the mixed-layer and might increase σ_1. We performed numerical experiments extending the initial condition below the mixed-layer, but in all of them mode 2 was still more heavily weighted than mode 1, and hence the resulting modelled wave-field still looked more like Fig. III.7a_{ii} than the observations (Fig. III.7a_i). Furthermore, the observed E_{PC} just before the October 4 storm was very near zero, so the directly forced inertial waves did not extent deeper than 60 m. It is interesting to notice that the observed E_T in the beginning of the October event is significantly larger than the observed E_{ML}, a situation that is not repeated in the January and March events. Pre-existing, small amplitude inertial waves between 500 and 4000 meters during the October event may have affected the relative weighing of the vertical modes resulting in a very strong first mode. For the January and March events the observed near-inertial currents were indeed limited to the mixed

layer as assumed by the model. This may explain the better agreement between model and data for these events, as the relative weight of mode 1 would not be much different between observations and model. We performed some numerical experiments adding deep ocean background inertial currents below the mixed layer to the initial condition in order to further enhance σ_1, but without dramatic effects. An increase of σ_1 to 17% caused by quite strong initial pre-existing currents in the water column generated a significant E_{PC} peak at time t_1 as expected, but not high enough to explain the observations. We could not get further increase of σ_1 without using unrealistic initial velocity profile.

III.6.*c. Detailed comparison*

The integrated energy provides a useful overall measure to compare model and observations; we now present the complete depth dependence of the observations and model. The detailed observations of the near-inertial response to the 3 events are shown in Figs. III.10a, 11a, 12a. Vectors indicate amplitude (length) and phase (angle) of the near-inertial oscillations relative to local f_0; contours of amplitude are also drawn. An estimate of the wave frequency at each instrument was obtained from the change of phase of U_- in time; constant phase indicates a pure inertial frequency f_0. The absolute value of phase is of no importance; however, vertical phase differences are significant.

The vertical propagation of energy from the October event (Fig. III.10a) appears as a well-defined beam of energy that radiates into the pycnocline. As seen in the integrated HKE, the increase of E_{PC} begins immediately after the storm (Fig. III. $7a_i$). During the first 10 days the energy increases throughout the pycnocline--after 14 October the energy begins to decrease in the upper pycnocline creating an energy maximum at 100 m. The maximum weakens as it deepens to 140 m by early November. The wave amplitude does not appear to be modulated by the stratification, as would be expected if the WKB approximation were valid in the vertical. The near-inertial signature of the event is traceable down to at least 1000

meters. The observed frequencies are between 1.02-1.05 f_0 (Fig. III.9a$_i$) with short periods (2-5 days) of sub-inertial frequencies. The average frequency increases slowly with depth, resulting in a phase difference between 60 and 195 meters that grows in time as the beam propagates deeper. After the amplitude at the beam maximum begins to decrease after October 17, the currents at 60 and 195 meters have a phase difference of about 120 ^{0}.

Both the January and March responses appear qualitatively different from the October beam. In contrast to October the energy generated by the storms did not penetrate into the pycnocline for 7-8 days. When finally entering the pycnocline, the near-inertial energy did not appear as a well-defined beam; that is, there was no pronounced energy maximum with depth as was found in October.

In both January and March the observed mixed-layer frequency remained quite close to inertial, 1.00-1.01 f_0 most of the time (Fig. III.9). The vertical structure of the observed phase is consistent with the downward propagation of energy -- constant values of phase propagating upwards with time. The phase difference between 195 m and the mixed-layer varied from 90^0 to 150^0, with a rather constant increase of phase with depth in-between. In both events there are short periods of sub-inertial frequency followed by periods of high-frequency currents (1.03-1.05 f_0) in the mixed-layer. The frequency of the pycnocline currents is high, near 1.05 f_0 when the amplitude is increasing (compare Fig. III.11, top panel, and Fig. III.8). When the amplitude stops increasing the frequency drops to 1.00-1.01 f_0. The phase difference between the mixed-layer and the 195 meter currents after the beam's evolution is around 120^0 .

The detailed vertical structure of the model for the 3 storm events is shown in Fig. III.10b, 11b, 12b. Since all 3 storms were propagating to the NE, the modeled responses bear many similarities. One characteristic common to all model runs is that the peak of the wave amplitude propagates very slowly vertically. The energy appears to "stick" to the top of the pycnocline. The modeled phases for each event are shown if Fig. III.9. The waves have increasing frequencies with increasing

depth in the upper pycnocline, resulting in phase differences increasing with time between depths. Both frequency and vertical phase differences are comparable to the observations. Again, the October event is an exception: the modelled waves at 160 and 195 meters have exceptionally high frequency of 1.05 f_0 and so in a month they develop 360^0 phase difference from 60 meters, while the observed phase difference after the beam passes is near 150^0.

III.6.*d. Modal elimination*

The failure of the model to form a downwards propagating beam of waves, is attributed to the high modes: The low modes, having higher group velocities, soon propagate southward and leave (Fig. II.2). The velocity profile then is determined by the remaining higher modes, whose shapes have maxima below the mixed layer, and strong vertical shears (Fig. III.13).

The observed currents propagate vertically as a beam, and don't stick below the mixed-layer. Thus, either the high modes have smaller magnitudes, or they lose strength by some dissipative process. The magnitude of each mode is definitely determined by the initial condition; lower coefficients for the high modes do not give satisfactory initial profiles. We made some numerical experiments gradually reducing the coefficients of the high modes, with encouraging results, as the waves had a tendency to form a beam of downward propagation (Fig. III.14). A method of eliminating the higher modes would be consistent with results by Fjeldstad (1963), McCreary (1981) and Kundu (1984): They showed that the computation of vertical modes is possible for an eddy viscocity coefficient ν that is inversely proportional to $N^2(z)$. Then, the equations describing the horizontal propagation of each mode are similar to (15)-(16) in chapter II, but also have a body friction-like term with a friction coefficient inversely proportional to the square of the modal eigenspeed, c_n^{-2}. For a viscocity like this, the higher modes would soon be dissipated, having higher friction coefficients, with the life time of each mode increasing with decreasing n.

III.7. Summary and conclusions

This paper compares three relatively distinct events of inertial current generation during the OCEAN-STORMS experiment with results from a linear numerical model. We focused our attention on the characteristic time-scales of energy exchange between the mixed-layer and the pycnocline.

A slab model, forced by a local wind time-series, was used to isolate the wind forcing events of local generation. Three events of strong local forcing were selected for analysis: October 4, 1987, January 13, 1988, and March 5, 1988.

Current meter data were complex demodulated to isolate the near-inertial response. The observations from each of the selected events were described in terms of energy exchange between mixed-layer, pycnocline and deeper ocean, as well as in terms of temporal and vertical structure of the waves.

The three-dimensional, linear model developed in chapter II, was run for each of the three selected events. To that purpose, the model's stratification and mixed-layer depths were adjusted to fit the conditions during the events; the amplitude and horizontal structure of the mixed-layer oscillations immediately after the forcing had also to be determined as initial conditions. The modeled amplitude of the initial mixed-layer currents was set to fit observations; the horizontal wavenumbers were estimated using monthly North Pacific storm-track maps. We also used initial wavenumbers of different directions, as well as a range of horizontal extents of the initial conditions, in order to built a framework for assessing the model's ability to reproduce observed features of the wavefields.

The modeled currents were processed and analyzed exactly like the observations. We compared model and data in terms of energy exchange between mixed-layer and pycnocline, as well as structure of the wavefields.

Finally, we proposed physical processes – not described by the model – that could be responsible for the areas of failure of the model, to accurately reproduce the observed wave field.

The observed near-inertial response of the ocean demonstrated some characteristics common to all cases, and some differences among them:

- The time-scale for the energy propagation from the mixed-layer to the pycnocline, defined as the time for E_{PC} to reach its maximum, was 13-15 days for all three events. However, the increase started immediately after the October event, while it was delayed by about a week in the other two events.

- The time for E_{PC} to return to background levels was 13-15 days for the October and March events. The decay of E_{PC} was not clearly defined during January, due to the multiple atmospheric forcing.

- The observed mixed-layer frequencies were 1.00-1.01 f_0 for 14-20 days, then fluctuated between 0.08 f_0 and 1.03 f_0 (January, March) (Fig. III.9a_i,b_i,c_i). No estimates of frequency were available for the mixed-layer in October.

- The waves propagated into the pycnocline as a beam (Fig. III.10a, 11a, 12a). The beam maximum propagated vertically from 60 to 100 m in a week (October); the distance between 100 and 195 m depth was covered by the beam maximum in 11 days in January and 6 days in March.

- The frequencies recorded in the pycnocline are higher inside the "beam", ranging from 1.03 to 1.05 f_0, at all events. After the beam is gone, the frequencies fall to 1.00-1.02 f_0. The higher frequencies are associated with the vertical propagation of the beam.

- In all three events, the near-inertial waves of the pycnocline develop higher frequencies than the mixed layer currents during the passage of the beam; as a result, vertical phase differences develop that increase in time as the beam propagates vertically. The resulting phase difference after the propagation of the beam between 60 and 195 meters is usually 120 ± 30^0. The phase propagates upward, consistent with downward propagation of energy.

We compared the observations with both the numerical model and the analytical predictions based on linear theory, developed in chapter II. The main conclusions from the comparison were:

- The overall amount of energy observed radiating from the mixed-layer to the pycnocline, is reproduced by the model. The magnitude of the pycnocline energy, E_{PC}, of the modeled currents, is comparable to the observed E_{PC}, for all three events.

- The changes of the observed pycnocline energy E_{PC} occur near the analytically predicted times t_1 and t_2 (beating of modes 1 and 2 respectively), calculated using our initial wavenumber estimates for each event.

- There is a trend of the model to slightly underestimate the peak of E_{PC} at t_1 and overestimate it at t_2 for the January and March events. This disagreement is greatest during the October event; while the model shows E_{PC} peaking at time t_2 , the observed peaks at t_1..

- The features of the energy exchange between mixed-layer and pycnocline for the October and March events suggest that the pumping is due to modal interference and not due to modal departure. Modal departure may be important during January.

- The detailed vertical structure of the observed currents is different than the modeled. The modeled currents do not propagate vertically as a beam, but rather stick to the top 40-50 m of the pycnocline.

- The modeled currents have frequencies ranging from slightly sub-inertial to 1.05 f, and their phase propagates upward, both characteristics of the observed currents. However, the model fails to reproduce the detailed temporal and spatial structure of the phase of the observed currents.

We propose some possible explanations for the areas of disagreement between the model and the data:

- The different E_{PC} values at the predicted time-scales t_1 and t_2 could be explained by reapportioning energy to the vertical modes. All events seem to suggest that the model either greatly (October event) or slightly (January and March events) underestimates the weight of the first mode. A more heavily weighted first mode would cause more energy to propagate to the pycnocline at time t_1 . Experiments, like extending the initial currents below the mixed-layer, or introducing some pre-existing currents throughout the water column, gave encouraging results, strengthening mode 1 and enhancing the peak of E_{PC} at t_1, but none reproduced as high a peak as observed during the October event.

- The relative vorticity field of the background currents could also be a factor of causing the faster-than-expected inertial pumping observed during the October event.

- A method of gradual elimination of the higher modes would generate a more beam-like vertical propagation of waves. The modal elimination method is based on dissipating the modes by a body friction caused by vertical eddy diffusivity.

In this chapter we exhausted the possibilities of a linear model to explain the structure of the near-inertial waves in the upper ocean. The various numerical experiments we performed suggested possible explanations for the areas of disagreement between model and data. The faster-than-predicted inertial pumping in October might be explained by a very heavily weighted first mode; although we could not account for such a mode 1 using realistic initial conditions, we cannot exclude this possibility. Also, a beam-like wave propagation could be reproduced by a method of gradually eliminating modes. Such a method is consistent with eddy diffusion dissipating the higher modes; however, further investigation of such questions would require use of a more flexible model, one that could include non-linear terms and incorporate mixing.

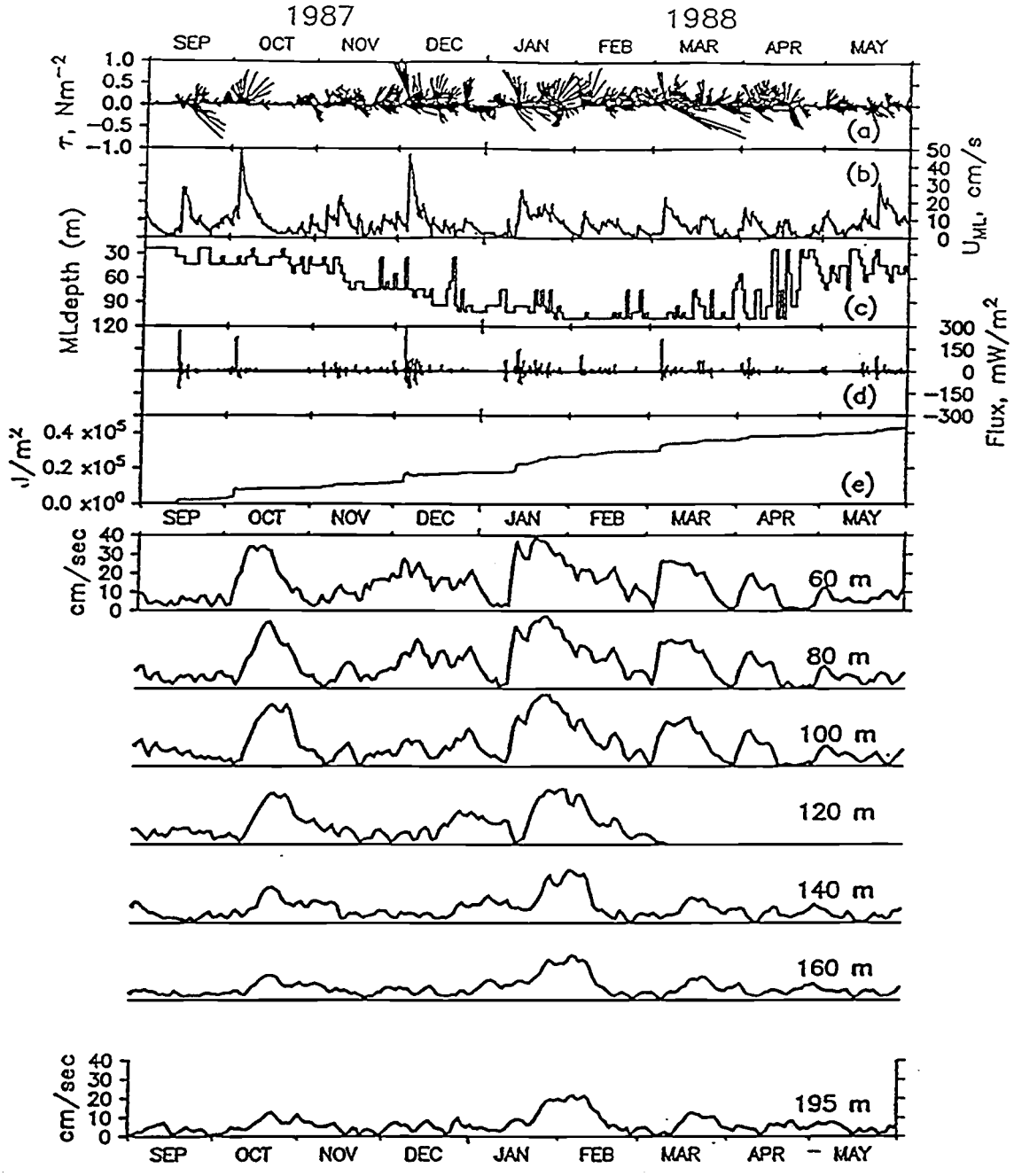

Fig. III.1. Observed (a) wind-stress from anemometer data; (b) mixed-layer inertial currents generated by the above time-series using the slab model; (c) mixed-layer depth; (d) energy flux into the mixed-layer from the wind (slab model); (e) energy input into the mixed-layer from the wind (slab model); observed data at 60, 80 100, 120, 140, 160 and 195 meters.

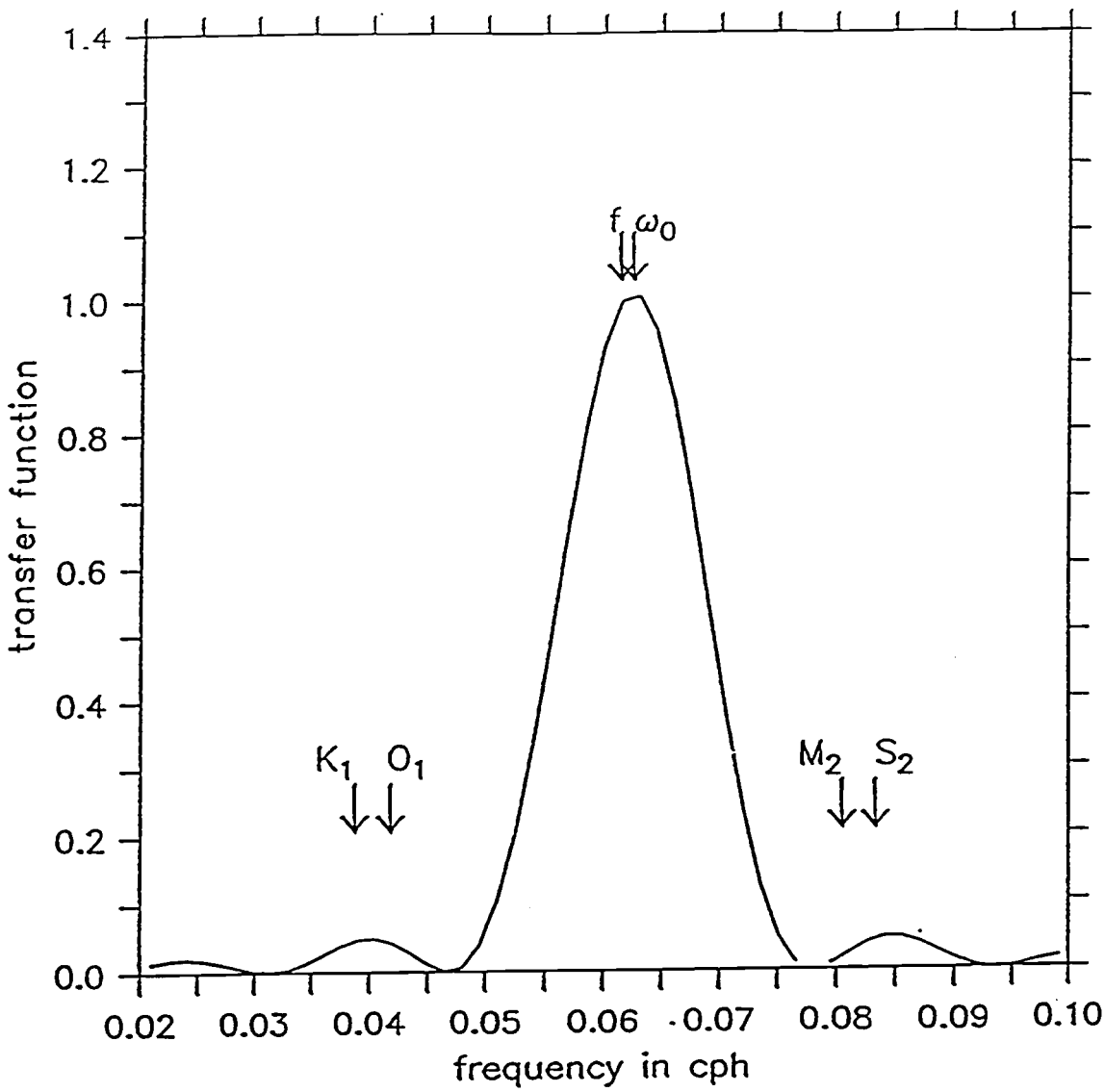

Fig. III.2. The transfer function for the complex demodulation method we are using. The demodulation is around ω_0, the local inertial frequency is f. Also shown are the frequencies of dominant astronomical forcing.

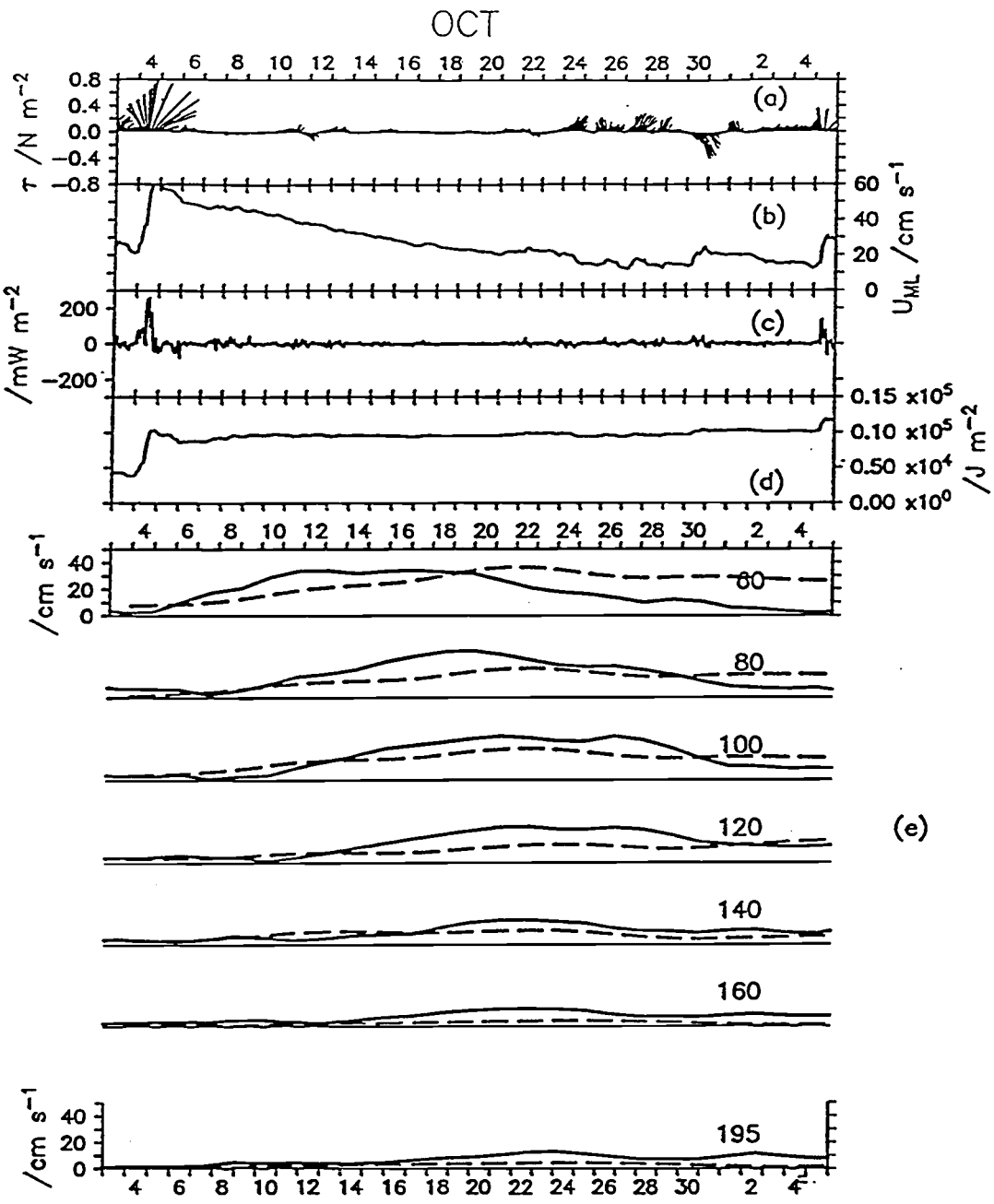

Fig. III.3. October Event: From top to bottom: Wind Stress (a), Slab-model's mixed-layer inertial currents (b), energy flux (c) and its time-integral (d). For an initial value problem to be applicable, (c) should approximate a δ function and (d) a step function. Panel (e) displays the observed (solid) and the modelled (dashed) data at all upper ocean current meter depths.

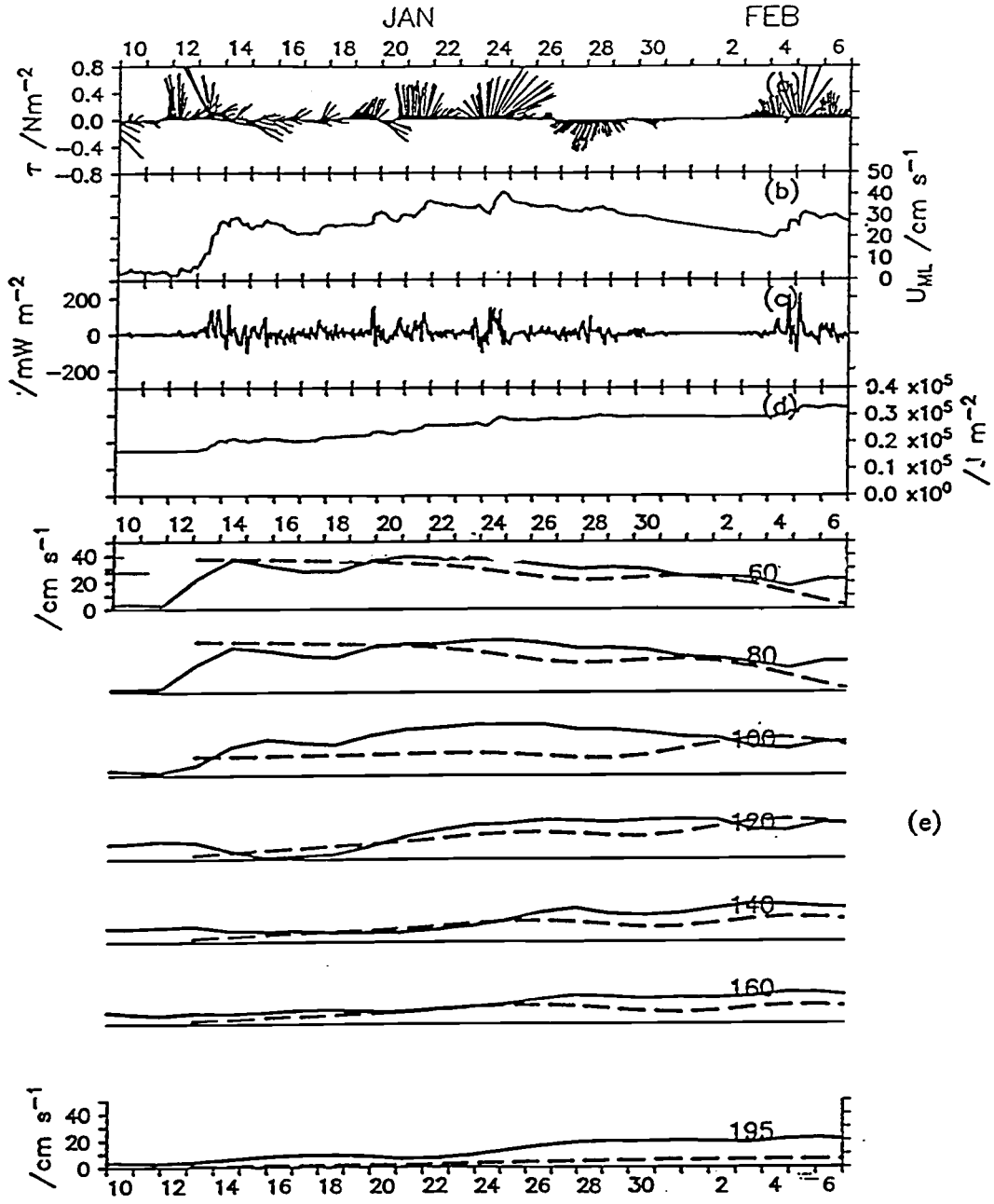

Fig. III.4. January Event : As in Fig. III.3. Note the continuous forcing events in (c) are not like a δ function, while the injected kinetic energy density (d) keeps increasing until the 24 of January.

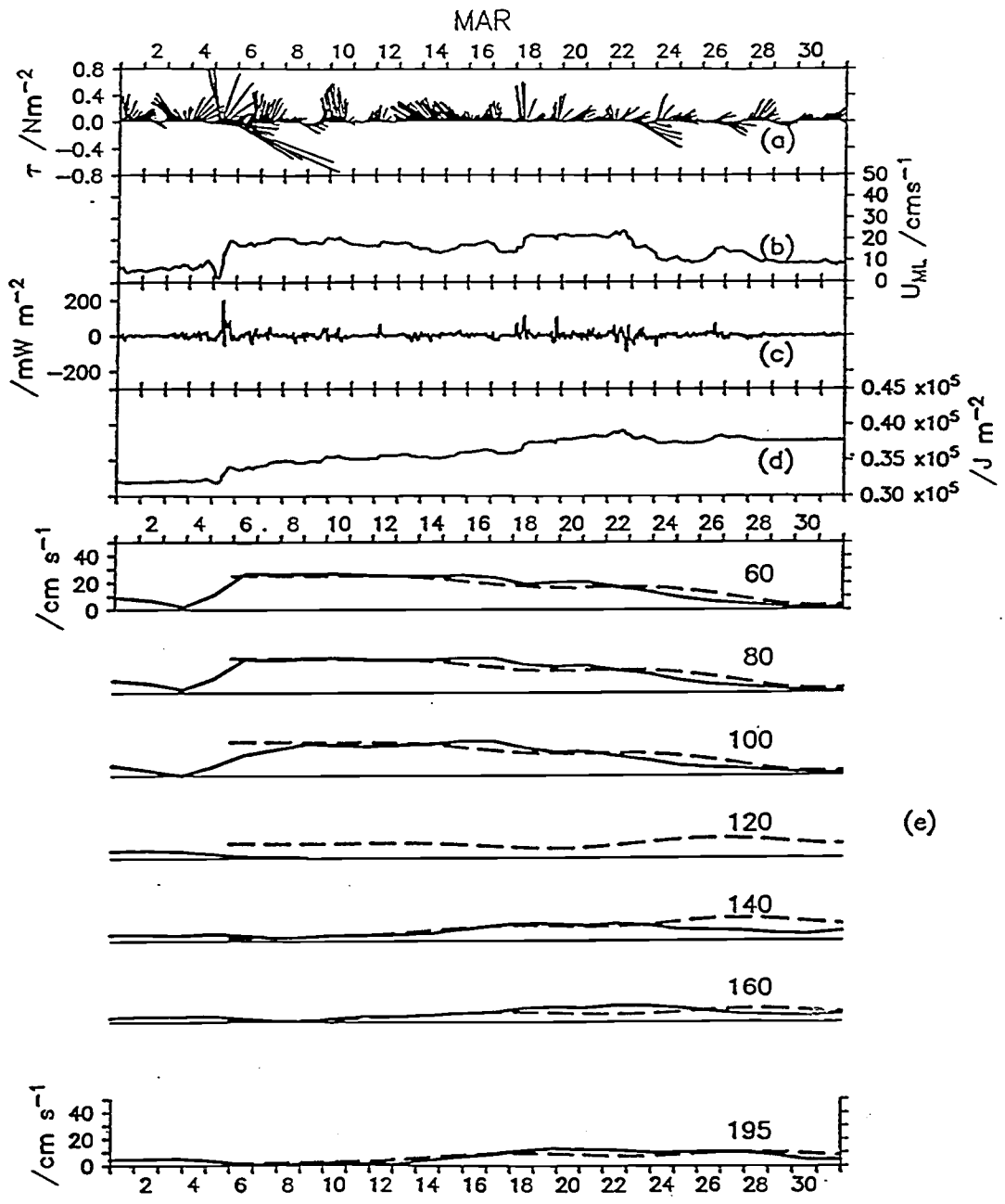

Fig. III.5. March Event : As in Fig. III.3.

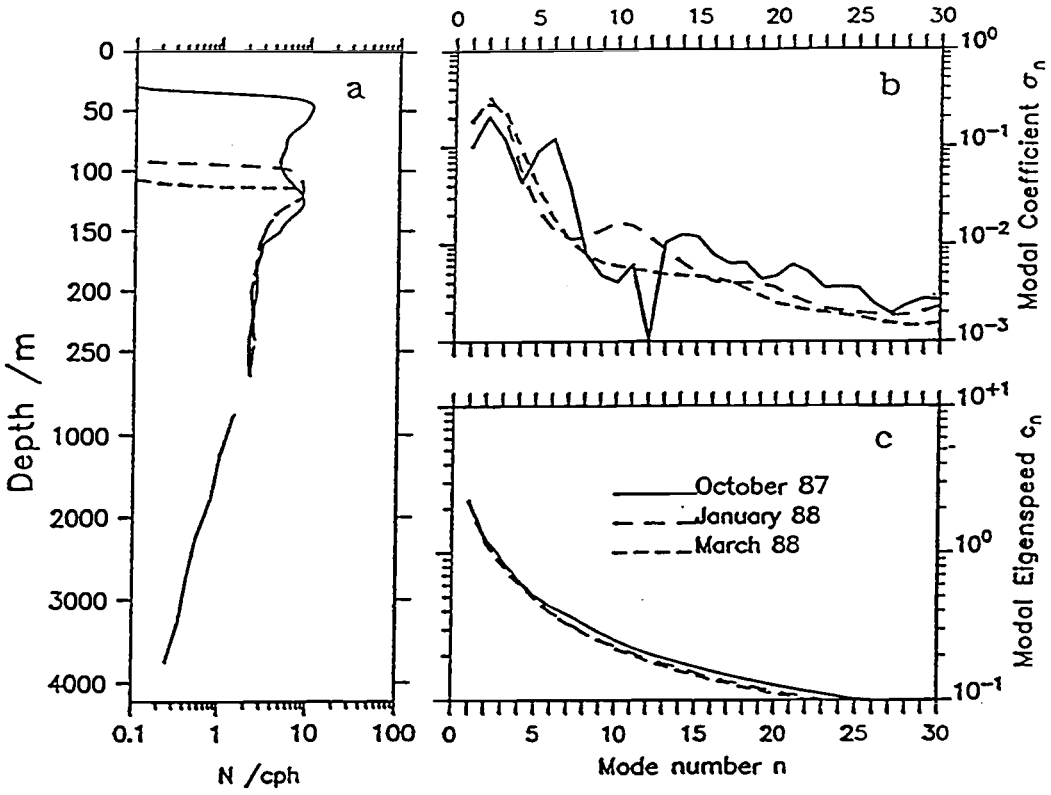

Fig. III.6. (a) The N-profiles used in this analysis, corresponding to the three events; (b) the relative weights of the modes (contribution of each mode to the initial mixed-layer velocity) σ_n, as functions of wavenumber, for the three distinct events; (c) the *modal eigenspeeds*, determining the propagation of each mode, as a function of mode number. Note that the eigenspeeds remain essentially the same for all three events.

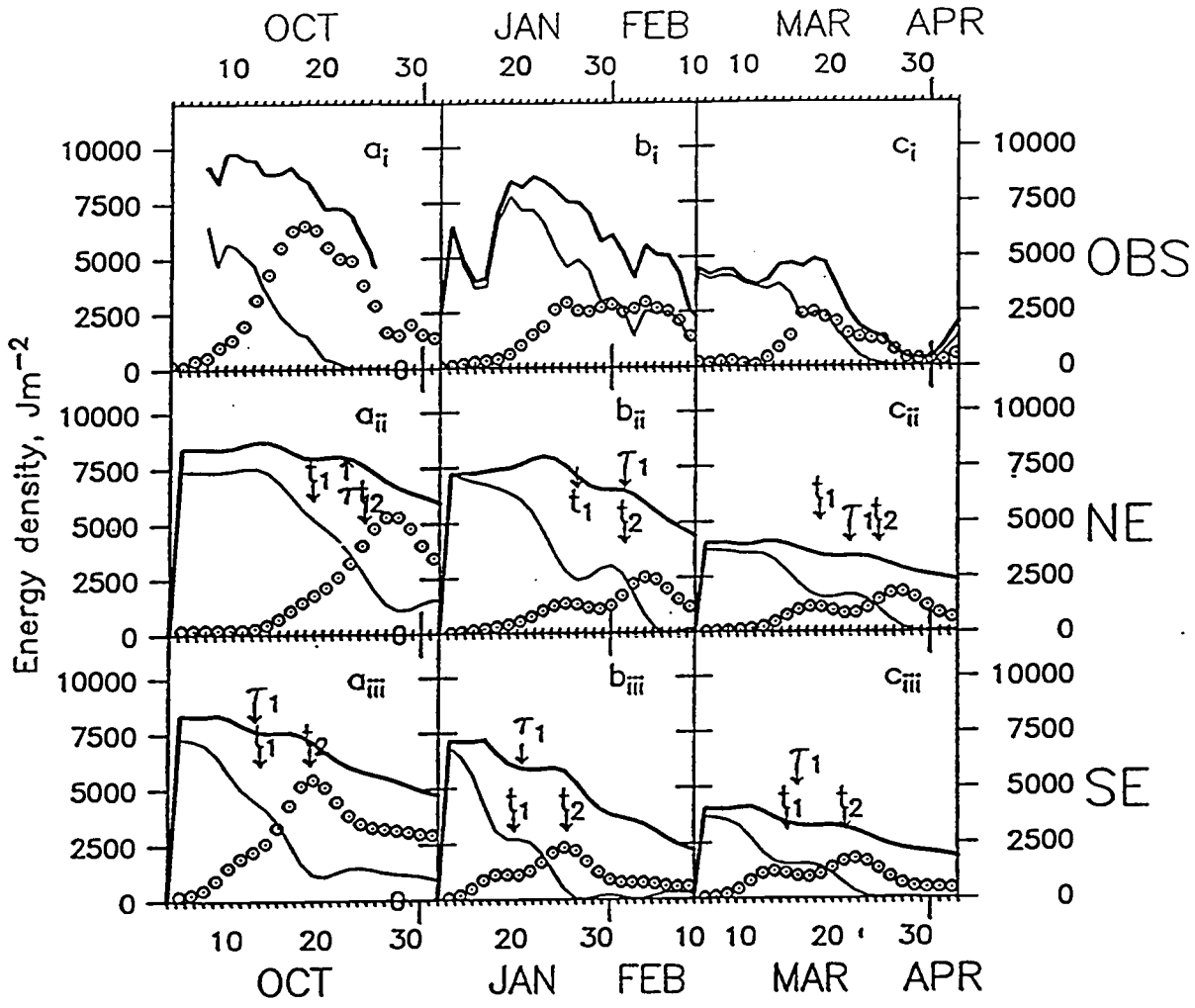

Fig. III.7. Horizontal kinetic energy density vertical integrals of observations and model runs. Here, we vary the initial N-S wavenumber l_o of the model's initial conditions, to investigate the effect on the sampled HKE. E_{ML} (light line), E_{PC} (dotted line), and E_T (heavy line) are displayed. The observations are shown in the top row. The runs have as initial condition a wave propagating to the NE (subscripts ii) and to the SE (subscript iii). Each column corresponds to an event: October, January and March, from left to right.

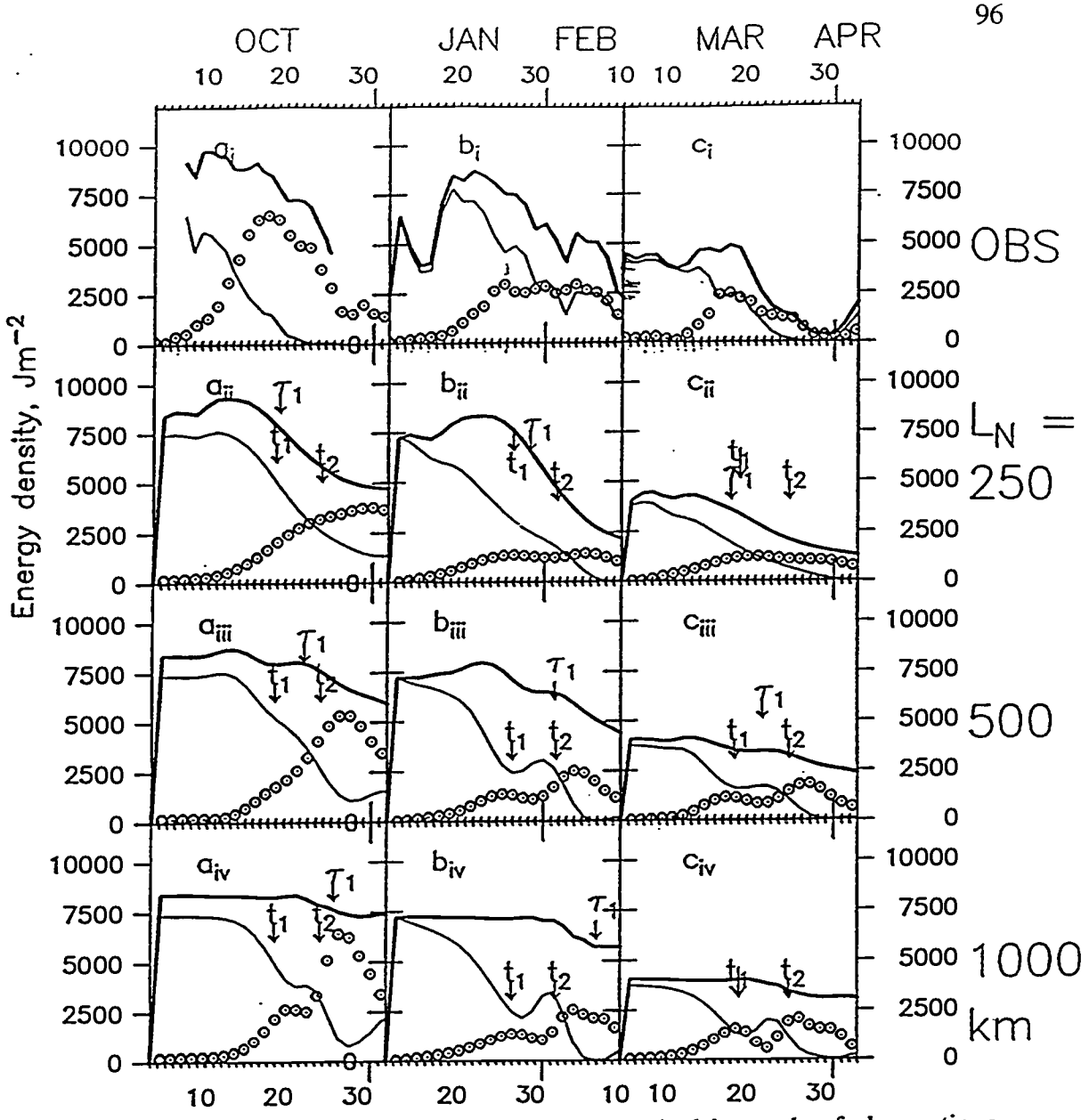

Fig. III.8. Horizontal kinetic energy density vertical integrals of observations and model runs. Here, we vary the northern extent L_N of the model's initial conditions, to investigate the effect on the sampled HKE. E_{ML} (light line), E_{PC} (dotted line), and E_T (heavy line) are displayed. The observations are shown in the top row. The runs are initialized by a wave propagating to the NE with LN = 250, 500 and 100 km are shown in rows 2, 3 and 4 respectively. Each column corresponds to an event: October, January and March, from left to right.

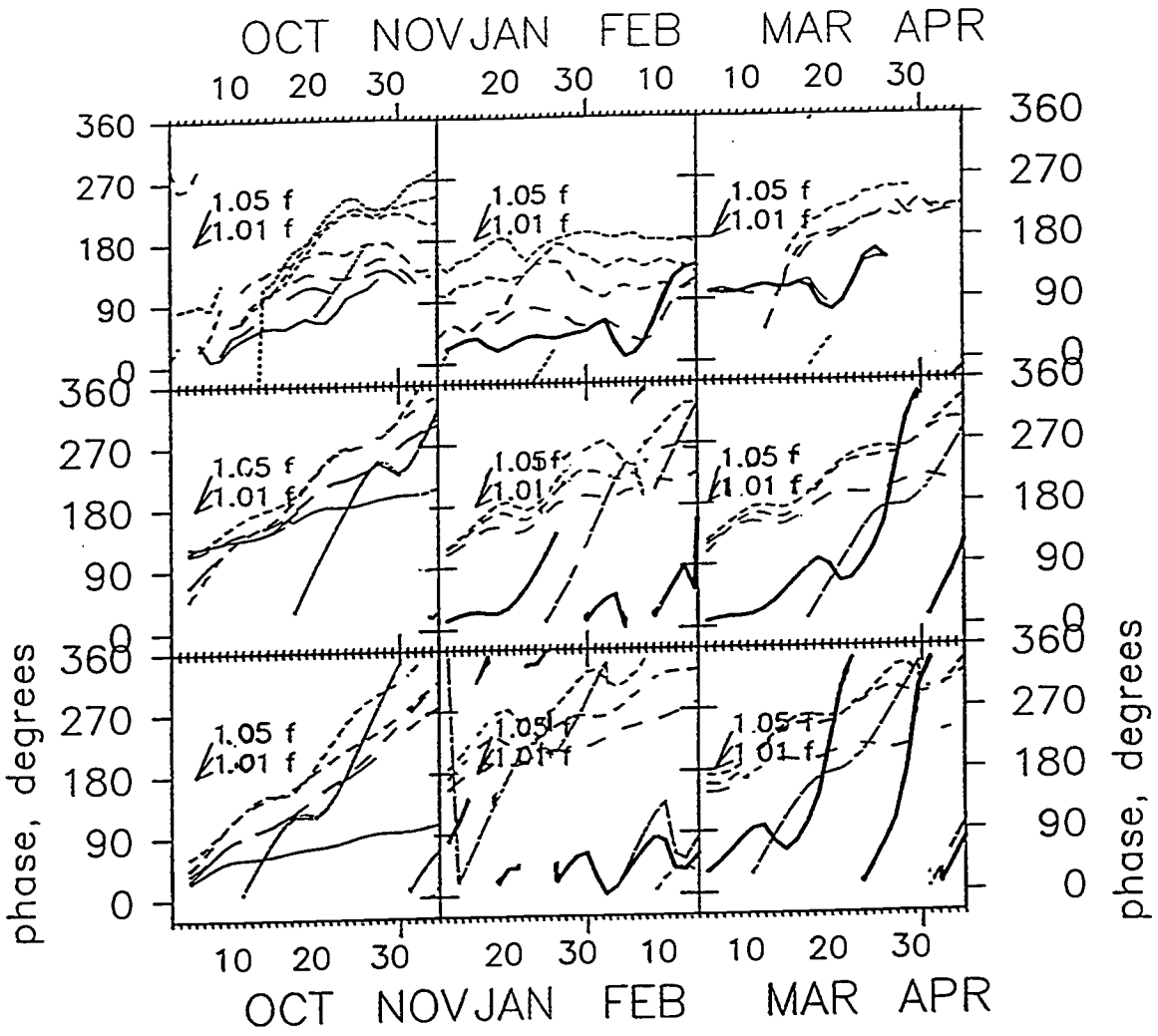

Fig. III.9. Phase time series of observations and model runs, displayed with the same order as in Fig. III.8. Observations from 60, 80, 100, 120, 140 160 and 195 are shown for October. From mixed-layer and 140, 160 and 195 meters for the other two events. Dash length decreases with increasing depth. Both frequency and vertical phase differences can be implied from this plot. The phase slopes for frequencies 1.01, 1.03 and 1.05 f_0 are shown in each panel.

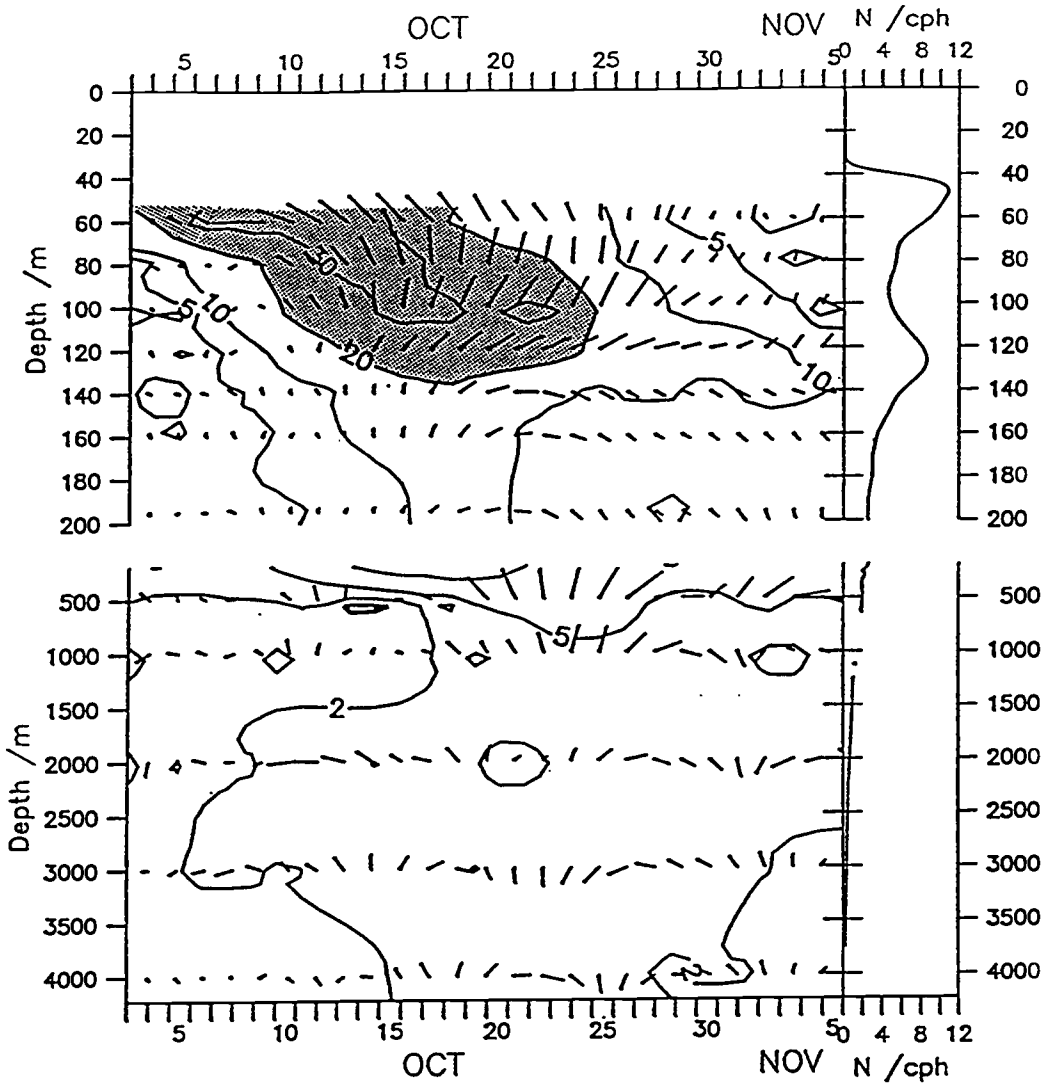

Fig. III.10a. Amplitude contour lines of October observations. Stick-diagrams of the decomposed, backrotated data are overlaid. The stratification profile is shown to the right of each panel.

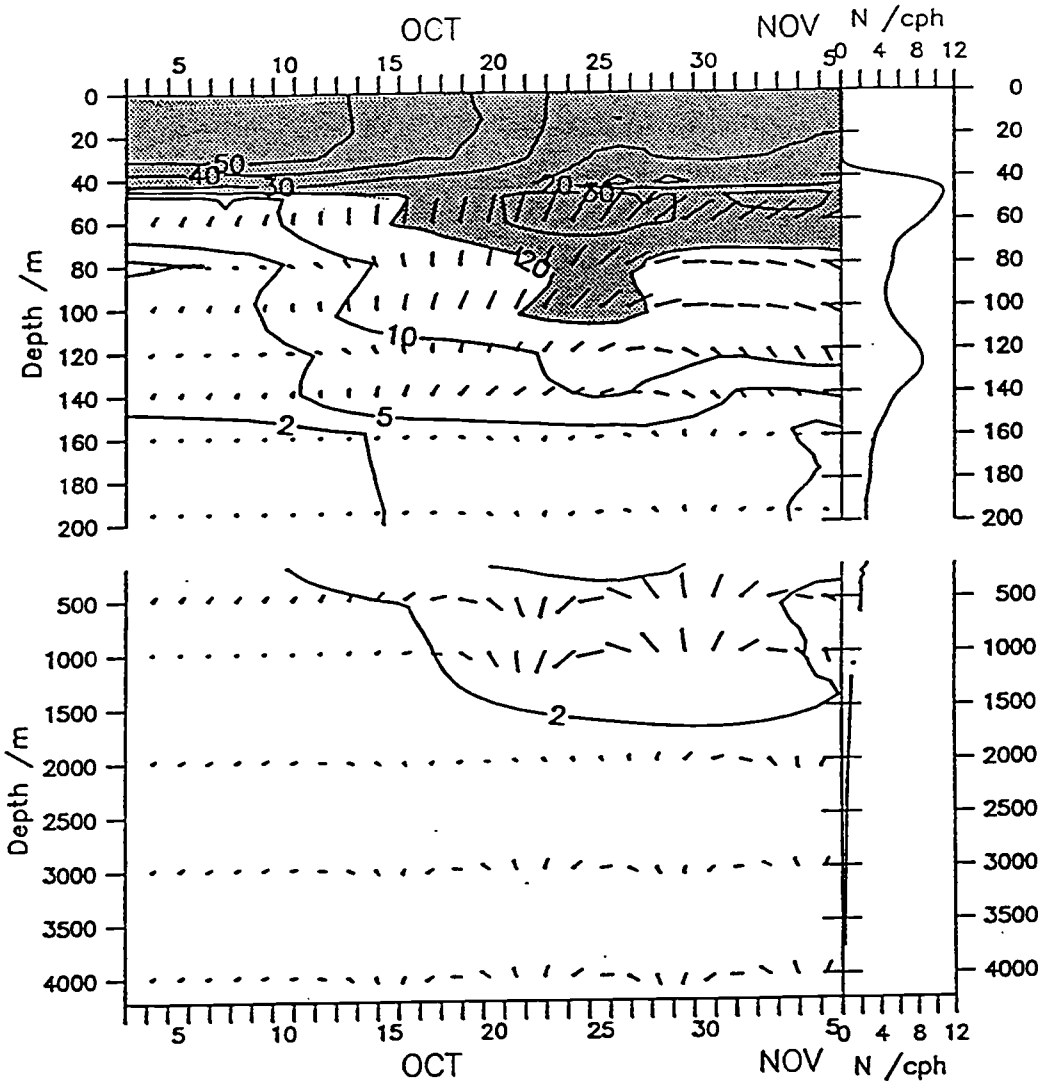

Fig. III.10b. As in Fig. III.10a, but for October model runs, using the initial wavenumbers of Table III.1.

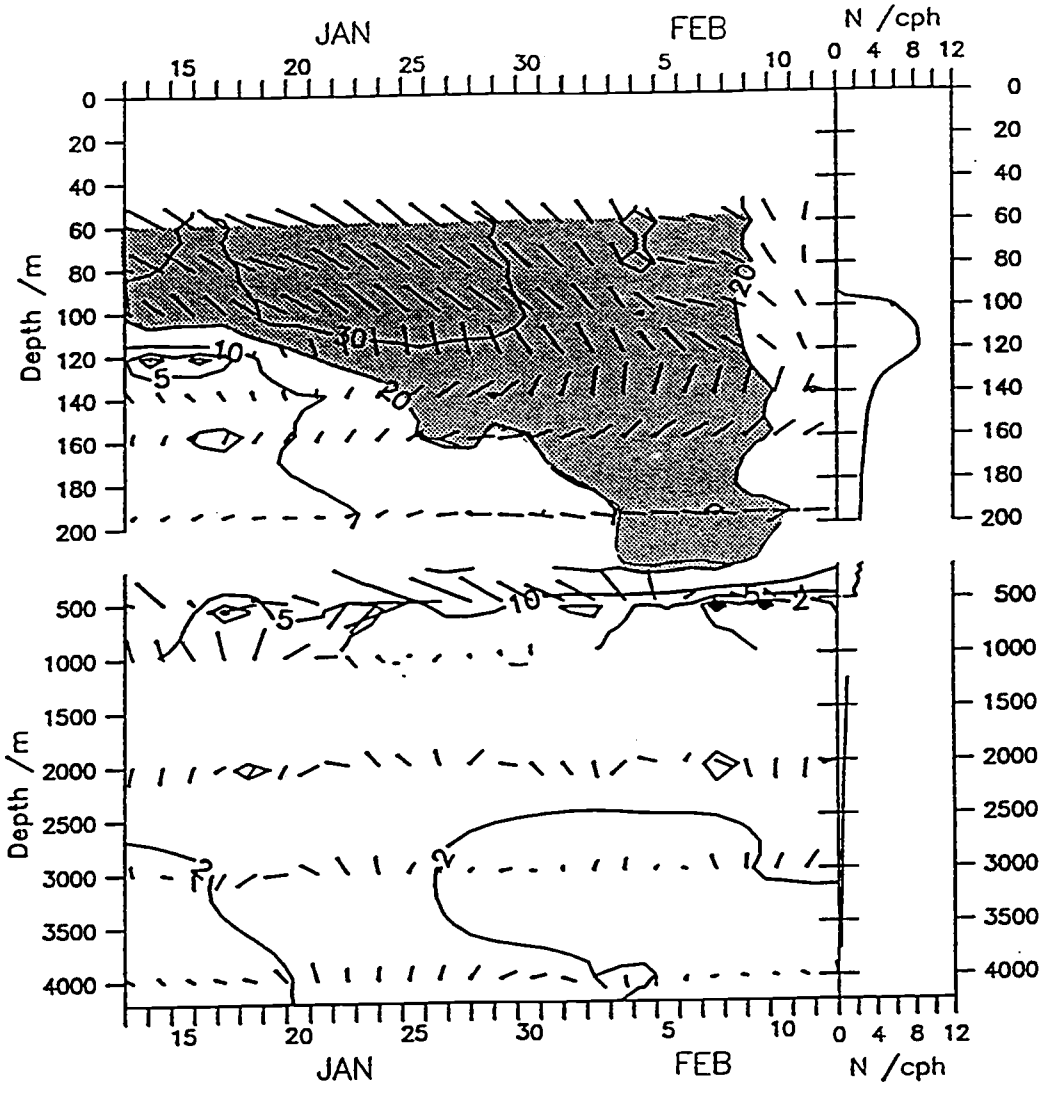

Fig. III.11a. As in Fig. III.10a, but for January observations.

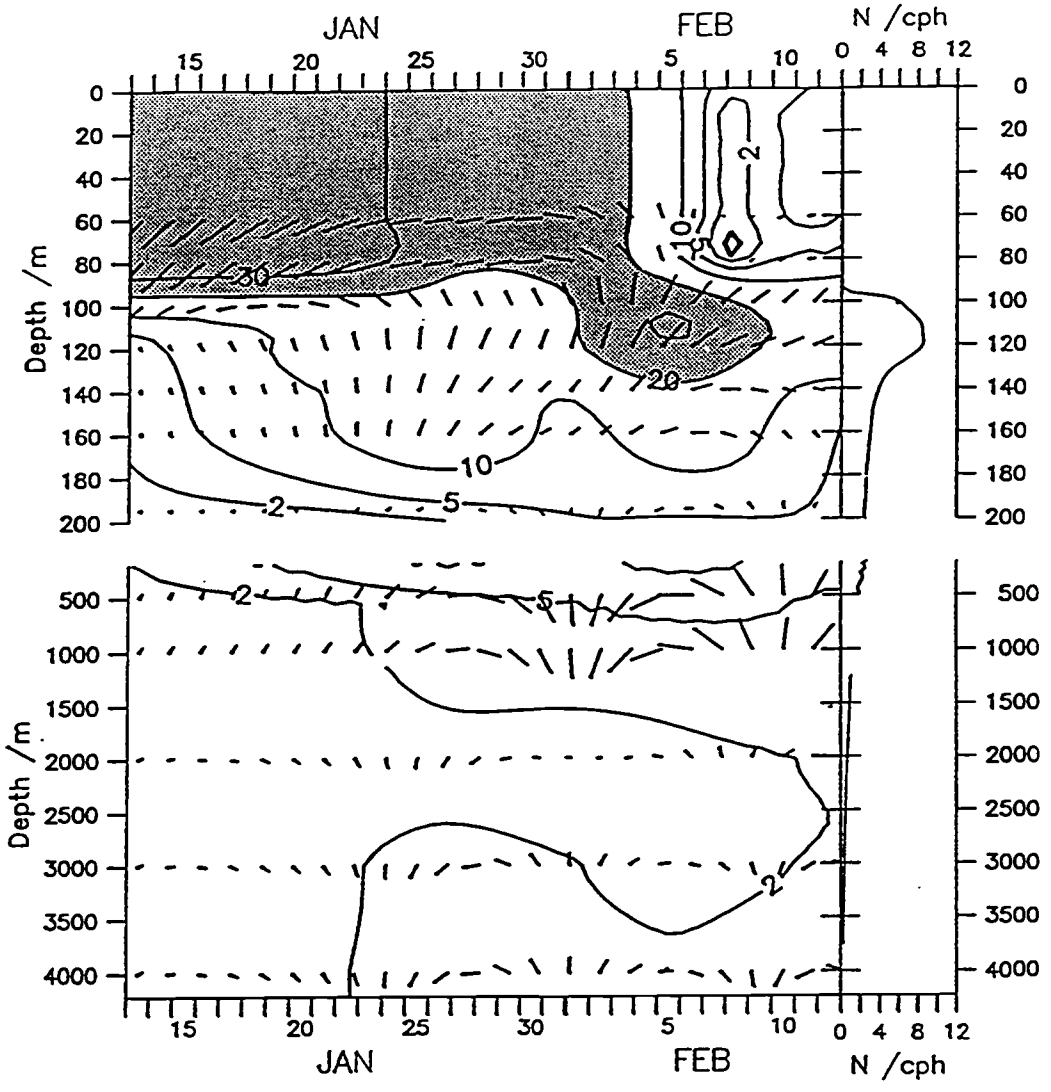

Fig. III.11b. As in Fig. III.10b, but for January model runs.

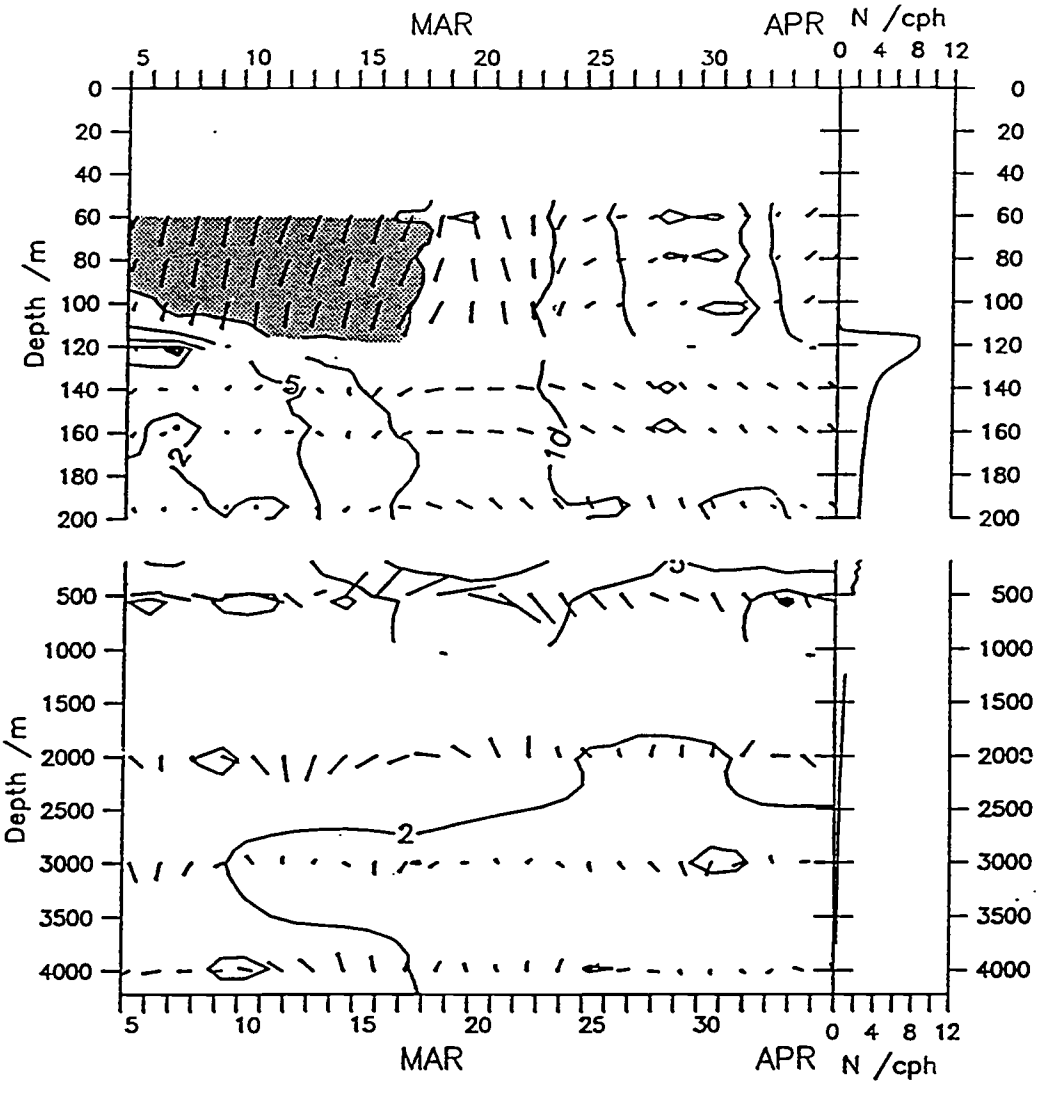

Fig. III.12a. As in Fig. III.10a, but for March observations.

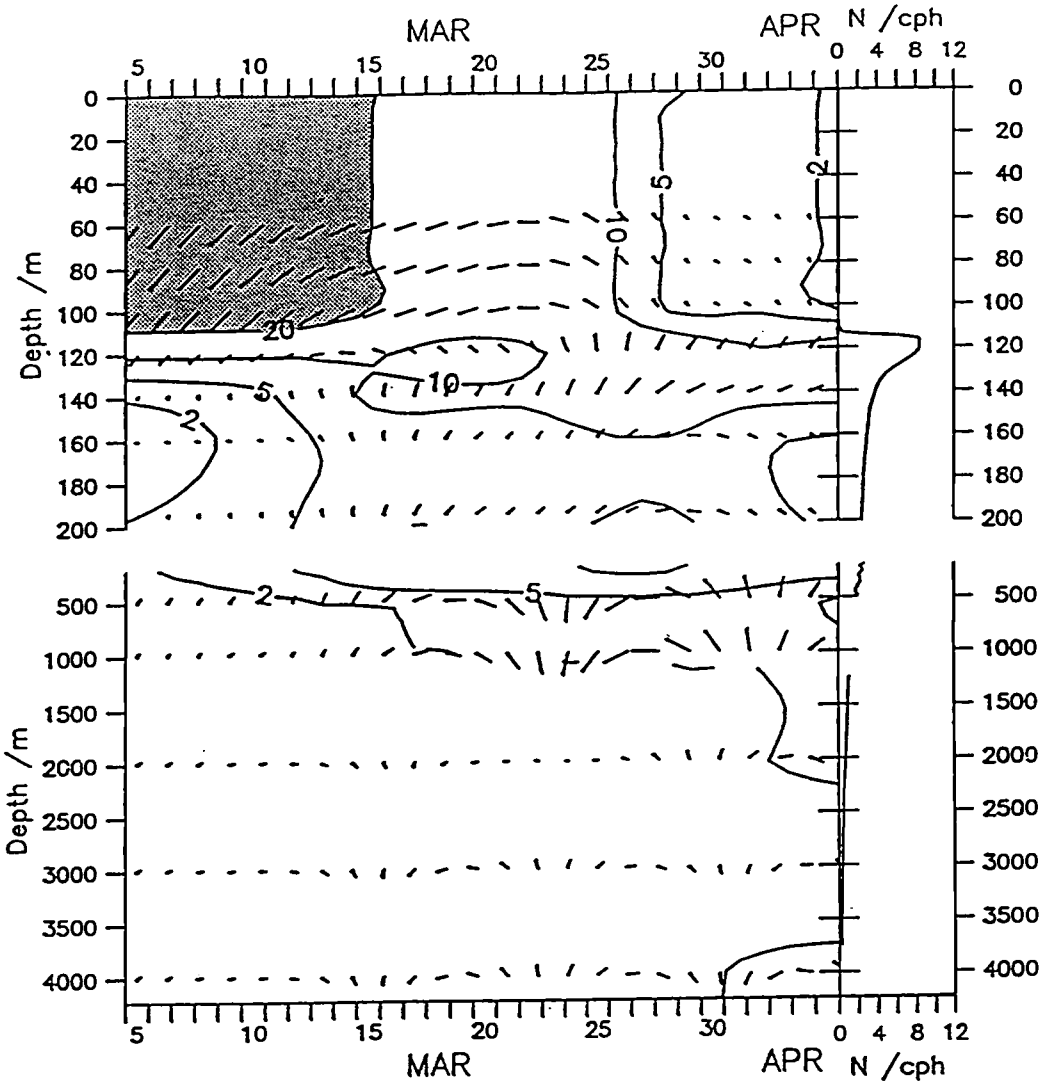

Fig. III.12b. As in Fig. III.10b, but for March model runs.

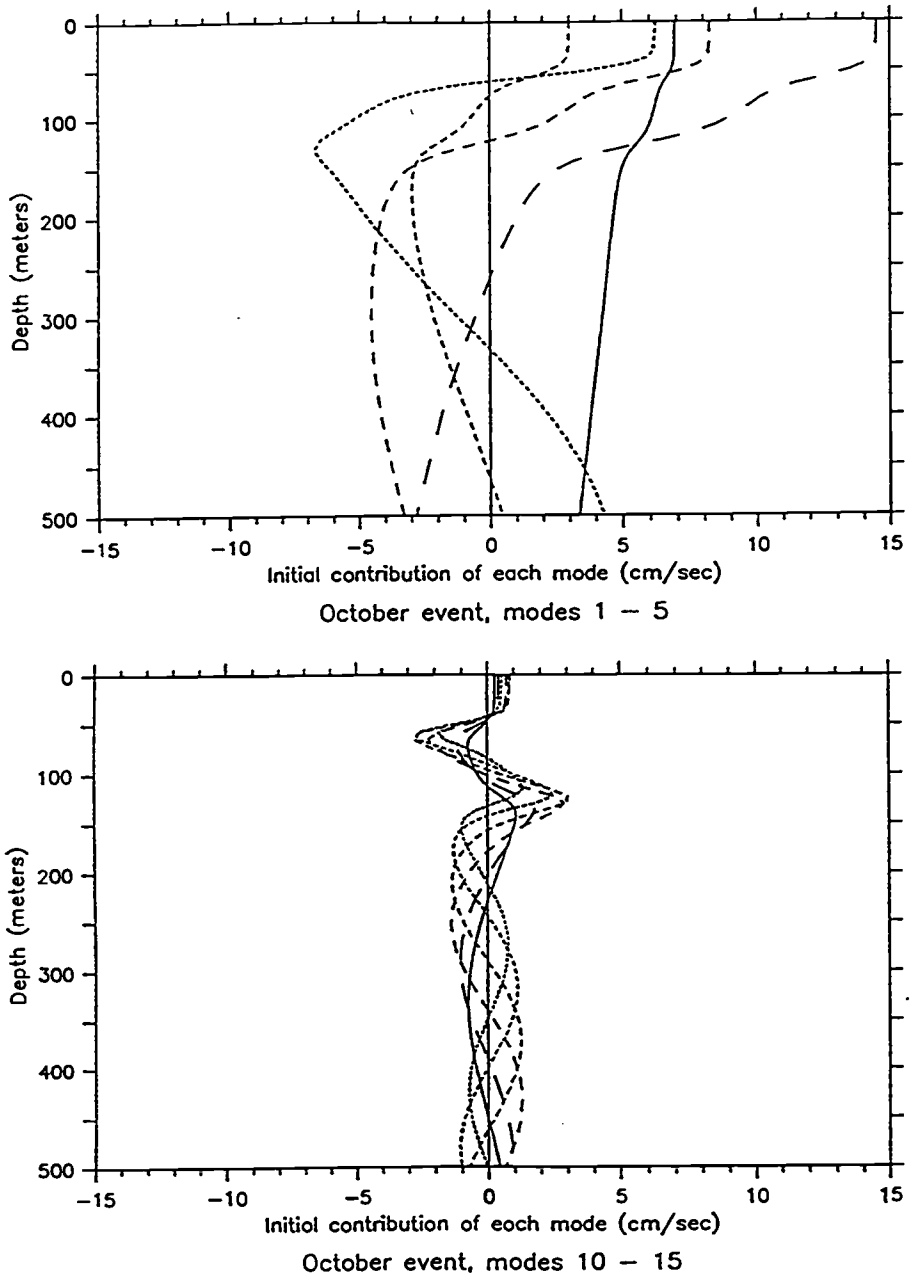

Fig. III.13. Modal shapes, weighted properly to provide S(z), the initial condition with depth, are displayed. Note the difference between the lower modes (top panel) and the higher modes (bottom panel).

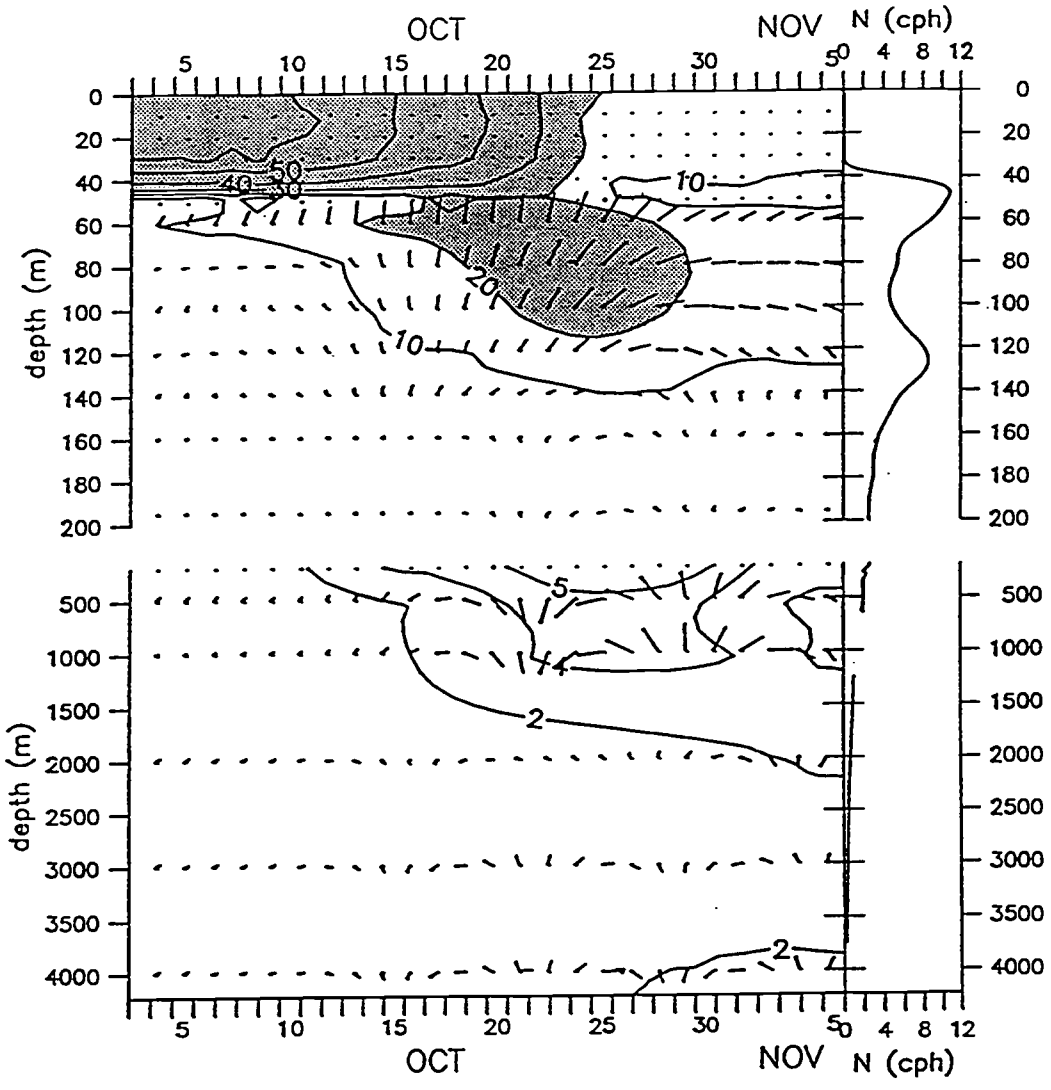

Fig. III.14. As in Fig. III.10b, but using a modal elimination method.

Table III.1. Horizontal wavenumbers of the directly wind-forced mixed-layer inertial oscillations, forced by the three selected wind events. The speed and bearing of the fronts have been computed from monthly storm-track maps.

Event	Bearing	Speed (ms^{-1})	k_0^{-1} (km)	l_0^{-1} (km)	k_0 $(km)^{-1}$	l_0 $(km)^{-1}$
October 4	30^0	16	290	165	0.003	0.006
January 12	45^0	10	126	122	0.008	0.008
March 3	60^0	15	161	262	0.006	0.004

III.8. References

Bell, T., 1978: Radiation damping of inertial oscillations in the upper ocean. *J. Fluid Mech.*, **88**, 2, 289-308.

Broutman, D. and W. R. Young, 1986: On the interaction of small-scale oceanic internal waves and near-inertial waves. *J. Fluid Mech,*. **166**, 341-358.

D'Asaro, E., 1985: The Energy Flux From the Wind to Near-Inertial Motions in the Surface Mixed Layer. *J. Phys. Oceanogr.*, **15**,1043-1059.

D'Asaro, E., 1989: The Decay of Wind-Forced Mixed Layer Inertial Oscillations Due to the Beta Effect. *J. Geophys. Res.*, **94**, 2045-2056.

D'Asaro, 1993: Analysis of Drifter data from OCEAN-STORMS.

De Young, B. and C. L. Tang, 1990: Storm-Forced Baroclinic Near-Inertial Currents on the Grand Bank. *J. Phys. Oceanogr.*, **20**, 1725-1741.

Eriksen, C. C., 1991: Observations of Near-Inertial Internal Waves and Mixing in the Seasonal Thermocline. *'A ha Huliko'a Hawaiian Winter Workshop Proceedings,* University of Hawaii at Manoa, January 15-18, 1991, pp. 71-88.

Fjeldstad, J. E., 1964: Internal waves of tidal origin. Part I. Theory and analysis of observations. *Geophyiske. Publikasjoner*, **XXV**, 5, 1-73.

Gill, A. E., 1982: Atmosphere-Ocean Dynamics, *Academic Press*, 346-353.

Gill, A. E., 1984: On the Behavior of Internal Waves in the Wakes of Storms. *J. Phys. Oceanogr.*, **14**, 1129-1151.

Gonella, J., 1972: A Rotary-Component method for analyzing meteorological and oceanographic vector time series. *Deep-Sea Res.*, **19**, 833-846.

Greatbatch, R. J., 1983: On the response of the ocean to a moving storm: The non-linear dynamics. *J. Phys. Oceanogr.*, **13**, pp. 357-367.

Greatbatch, R. J., 1984: On the response of the Ocean to a moving storm: Parameters and Scales. *J. Phys. Oceanogr.*, **14**, pp. 59-78.

Hebert, D., and J. N. Moum, 1993: Decay of a Near-Inertial Wave. *paper submitted to J. Phys. Oceanogr.*

Henyey, F. S., J. A. Wright, and S. M. Flatté. , 1986: Energy and Action Flow Through the Internal Wave Field: an Eikonal Approach. *J. Geophys. Res.*, **91**, C7, 8487-8495.

Krauss, W., 1981: The Erosion of a Thermocline. *J. Phys. Oceanogr.*, **11**, 415-433

Kundu, P. K., 1984: Generation of Coastal Inertial Oscillations by Time-Varying Wind. *J. Phys. Oceanogr.*, **14**, 1901-1913.

Kundu, P. K., and R. E. Thomson, 1985: Inertial Oscillations Due to a Moving Front. *J. Phys. Oceanogr.*, **15**, 1076-1084.

Kundu, P. K., 1986: A Two-Dimensional Model of Inertial Oscillations Generated by a Propagating Wind-Field. *J. Phys. Oceanogr.*, **16**, 1399-1411.

Kunze, E., 1985: Near-Inertial Wave Propagation in Geostrophic Shear. *J. Phys. Oceanogr.*, **15**, 544-565.

Levine, M. D., C. A. Paulson, S. R. Gard, J. Simpkins, V. Zervakis, 1990: Observations from the C1 mooring during OCEAN-STORMS in the N.E. Pacific Ocean, August 1987-June 1988. *Reference 90-3, Data Report 151, Oregon State University*, 18.

Levitus, 1982: Climatological Atlas of the World Ocean. *Professional Paper 13*, National Oceanic and Atmospheric Administration, U.S. Department of Commerce, Rockville, Md.

Lindsay, R. W. , 1988: Surface Meteorology during Ocean Storms Field Program. *Technical Report, APL-UW TR 8823*, Applied Physics Laboratory, University of Washington.

McCreary, J. P., 1981: A Linear Stratified Ocean Model of the Equatorial Undercurrent. *Proc. R. Soc. London*, Ser. A, **62**, 603-373.

Millot and Crépon, 1981: Inertial Oscillations on the Continental Shelf of the Gulf of Lions-Observations and Theory. *J. Phys. Oceanogr.*, **11**, 639-657.

Paduan, J., R. A. de Szoeke, and R. A Weller, 1988: Inertial Oscillations in the Upper Ocean During the Mixed Layer Dynamics of the Upper Ocean Experiment. *J. Geophys. Res.*, **94**, 4835-4842.

Perkins, H. T., 1970: Inertial Oscillations in the Mediterranean. *PhD Thesis*, M.I.T.-W.H.O.I.

Pollard, R. T., 1970: On the Generation by Winds of Inertial Waves in the Ocean. *Deep-Sea Res.*, **17**, 795-812.

Pollard, R. T. and R. C. Millard, 1970: Comparison Between Observed and Simulated Wind-Generated Inertial Oscillations. *Deep-Sea Res.*, **17**, 813-821.

Price, J. G., 1983: Internal Wave Wake of a Moving Storm. *J. Phys. Oceanogr.*, **13**, 949-965.

Qi, H., 1993: *Personal Communication*

Rubenstein, D. M., 1983: Vertical Dispersion of Inertial Waves in the Upper Ocean. *J. Geophys. Res.*, **88**, 4368-4380.

Shay, L., K., and R. L. Elsberry, 1987: Near-Inertial Ocean Current Response to Hurricane Frederick. *J. Phys. Oceanogr.*, **17**, 1249-1269.

Shay, L., K., R. L. Elsberry and P. G. Black, 1989: Vertical Structure of the Ocean Current Response to a Hurricane. *J. Phys. Oceanogr.*, **19**, 649-669.

Smith, S. D., 1988: Coefficients for Sea Surface Wind Stress, Heat Flux, and Wind Profiles as a Function of Wind Speed and Temperature. *J. Geophys. Res.*, **93**, C12, 15,467-15,472.

Tabata, S., L. A. F. Spearing, R. H. Bigham, B. G. Minkley, J. Love, D. Yelland, J. Linguanti, P. M. Kimber, 1988: STP / Hydrographic Observations along Line P, Line R and Associated Lines and in the "OCEAN STORMS" Area: Cruise I - 22 September - 16 October, 1987-- Cruise III -24 November - 9 December, 1987. *Canadian Data Report of Hydrographic and Ocean Sciences,***No 70**, Institute of Ocean Sciences, Department of Fisheries and Oceans, Sidney, B.C. V8L 4B2.

Wang, D. P., 1991: Generation and Propagation of inertial waves in the subtropical front. *J. Mar. Res.*, **49**, 619-633.

IV. PARAMETERIZING THE DECAY OF MIXED-LAYER INERTIAL OSCILLATIONS GENERATED BY THE WIND: A MODIFICATION OF THE SLAB MODEL.

IV.1. Abstract

Modeling the near-inertial response of the mixed layer to variable wind-speeds as a solid slab over time-scales of about an inertial period has been a quite successful way to simulate the generation of mixed-layer inertial oscillations. However, the method that the model uses to damp the inertial oscillations (a constant body friction term) does not necessarily represent the dominant process of extracting kinetic energy from the mixed-layer. In this paper we modify the parameterization of inertial oscillations' decay by assuming that inertial pumping is the dominant mechanism of energy transfer from the mixed-layer to the pycnocline. The new, decay coefficient, r', is found to be a function of latitude, stratification, mixed-layer depth and horizontal wavenumber of forcing, and to increase quadratically in time, as opposed to the previous estimates of $r^{-1} \sim 4$ days, a constant. Comparison of the slab model results with OCEAN-STORMS observations reveals a better agreement when using the new parameterization than the traditional method. This result suggests that the dominant sink of mixed-layer inertial energy during the OCEAN-STORMS experiment was provided by inertial pumping, and that the horizontal scales of the forcing were large.

IV.2. Introduction

Mixed-layer inertial oscillations are very commonly observed in the ocean (Day and Webster, 1964; Webster, 1968; Lacombe and Gonella, 1964; Hunkins, 1967, and many others). They are usually observed after the passage of a front, a storm or a hurricane, and they can be very energetic, with amplitudes exceeding 1 m s^{-1}. The hodograph of their velocity vector is nearly a circle on the horizontal plane, and their frequency is very near the local inertial f_0. The generation of inertial currents by the wind, clearly implied by the observations, has been successfully modelled by Pollard and Millard (1970) and other investigators (e.g. Kundu, 1976; Pollard, 1980; D'Asaro, 1985; Paduan et al., 1989). The basic assumptions of the Pollard-Millard model are: the mixed-layer responds to the wind-stress as a solid, horizontally homogeneous "slab" over time scales comparable to one inertial period and longer, and the stress is zero below the mixed-layer. This assumption is supported both by the very high vertical coherence of the observed mixed-layer currents, as well as the observed vertical wavenumber spectrum at the low frequency bands of the Garrett-Munk spectrum (Eriksen, 1988). The *slab* model (as it is known in the oceanographic community) has been proven successful in predicting the generation of mixed-layer inertial oscillations by variations in the wind-stress with time. We made use of the traditional slab model in chapter III.

The decay of the mixed-layer inertial oscillations has been modeled by Pollard and Millard (1970) (and all the investigators who made use of the slab model after them) with a body (or *Rayleigh*) friction, that damps the inertial oscillations. Since the slab model is inviscid and horizontally homogeneous, the added friction is the only way to extract energy from the slab, other than the occasional negative feedback by the wind. Other processes, possible candidates for sinks of mixed layer energy, like the generation of near-inertial internal gravity waves, known as *inertial pumping* (Pollard, 1970; Price, 1983; Gill, 1984; Kundu, 1985, 1986; others) or of high frequency waves (Bell, 1978) are not accounted for

by the slab model. The result of the body friction damping term is an exponential decay in time of the horizontal kinetic energy of the inertial oscillations. A constant decay coefficient r has been used by all investigators, with values for r^{-1} usually ranging from 2 to 8 days, with more common $r^{-1} = 4$ days.

In this note, we modify the decay parameterization of the slab model that models the energy loss in the mixed layer due to the generation of near-inertial internal gravity waves by *inertial pumping*. Appealing to the numerical model of near-inertial wave generation (chapter II), we propose a new friction coefficient $r'(t)$ that, contrary to the constant r, is compatible with inertial pumping. The quantity $r'(t)$ is a function of latitude and stratification, and does not require *ad hoc* tuning.

A short description of the traditional slab model is presented in section 2. Section 3 provides some insights to the background theory of linear inertial pumping. Based on those insights, we define a new decay coefficient for the slab model in section 4, and compare the impulse response of model using the new coefficient with the old one in section 5. Section 6 compares the impulse response of the modified slab model to results from a full water column numerical model. Comparison with mixed-layer current observations are made in section 7. We summarize our results and conclude in section 8.

IV.3. The Slab Model

IV.3.*a. Dynamics*

The slab model is derived from the linear horizontal momentum equations on a rotating earth:

$$\frac{du}{dt} - f_0 v = \frac{1}{\rho_0}\frac{\partial \tau^x}{\partial z} \tag{1}$$

$$\frac{dv}{dt} + f_0 u = \frac{1}{\rho_0}\frac{\partial \tau^y}{\partial z} \tag{2}$$

where (u,v) are the zonal and meridional components of current velocity; (τ^x,τ^y) are the zonal and meridional components of stress, ρ_0 the seawater density, and f_0 is the constant Coriolis parameter. Horizontal homogeneity has been assumed --- hence, there are no horizontal gradients and vertical particle velocity w=0. Assuming that the mixed-layer responds as a slab, and that the stress at the base of the mixed-layer is a *Rayleigh* body friction with friction coefficient r, we can integrate **(1)** and **(2)** over the mixed-layer depth H_{mix}. Dividing by H_{mix} yields:

$$\frac{du}{dt} - f_0 v = \frac{1}{\rho_0 H_{mix}}\tau_s^x - ru \tag{3}$$

$$\frac{dv}{dt} + f_0 u = \frac{1}{\rho_0 H_{mix}}\tau_s^y - rv \tag{4}$$

where $\vec{\tau}_s = (\tau_s^x , \tau_s^y)$ is the wind stress at the surface.

Defining $Z = u + iv$, $\omega = r + if_0$, and $T = \rho_0^{-1} (\tau_s^x + i\tau_s^y)$, we then write (3) and (4) in one equation:

$$\frac{dZ}{dt} + \omega Z = \frac{T}{H_{mix}} \tag{5}$$

The solution of (5) is given by:

$$Z(t) = Z(0)e^{-\omega t} + \int_0^t \frac{T(t')}{H_{mix}(t')} e^{-\omega(t-t')} dt' \tag{6}$$

where the first term is the solution to the homogeneous equation and the second term is the particular solution, expressed as a convolution of the impulse response with the forcing. The above solution includes the directly forced currents and the generation of inertial oscillations. The constant part of the directly forced current is the Ekman transport. The free near-inertial response can be isolated by subtracting the directly forced currents from (5) (D'Asaro, 1985; Paduan et al., 1989):

$$\frac{dZ}{dt} + \omega Z = \frac{1}{\omega} \frac{d\left(\frac{T}{H_{mix}}\right)}{dt} \tag{7}$$

The total solution can then be written

$$Z(t) = Z(0)e^{-\omega t} + \int_0^t \frac{1}{\omega} \frac{d}{dt}\left(\frac{T(t')}{H_{mix}(t')}\right) e^{-\omega(t-t')} dt' \tag{8}$$

IV.3.*b. Energetics*

The conservation of kinetic energy is obtained by multiplying (3) by $\rho_0 u$ and (4) by $\rho_0 v$ and adding :

$$\frac{\partial E}{\partial t} = \frac{\vec{\tau}_s \cdot \vec{u}}{H_{mix}} - 2rE$$

where E the horizontal kinetic energy density. The first term on the right hand side represents the energy flux into the mixed-layer by the wind, and the second term represents the energy dissipation due to friction. In the absence of wind stress ($\vec{\tau}_s = 0$) the mixed layer energy decays exponentially in time with a characteristic time-scale of $(2r)^{-1}$. Based on comparisons with observations, investigators have estimated r^{-1} to be between 2 and 8 days, with a most common estimate of 4 days (Pollard and Millard, 1970; D'Asaro, 1985; Paduan, 1989).

IV.4. Inertial pumping theory

Most investigators do not describe the physical process that the Rayleigh body friction represents in the slab model. D'Asaro (1985) proceeds to explicitly call r "an artificial damping constant that parameterizes the transfer of energy from the mixed-layer to the deeper ocean". One could argue that body friction term as used in the traditional slab model is a crude parameterization for drag acting on the base of the mixed-layer by turbulent mixing. In this section, we replace r by a time-dependent r´(t), defined to describe the loss of mixed-layer energy by the radiation of near-inertial waves through the process of *inertial pumping*. We base the form of r' on analytical predictions about the evolution of mixed-layer kinetic energy based on linear internal wave theory, developed in chapter II. The analytical predictions were tested by comparing with results from a numerical model that describes the near-inertial waves' propagation over the whole water column.

A short description of the analytical and numerical model developed in chapter II will help us understand the theoretical framework which will serve as a basis for modifying the slab model to describe inertial pumping. Both the numerical model and the analytical predictions are descendants of work done by Gill (1984). In a comprehensive analysis of the stratified ocean's response to mixed-layer currents, Gill showed that for the process of *inertial pumping* to efficiently extract energy from the mixed-layer, the horizontal scales of the wavefield should be comparable to the baroclinic Rossby radius. In that analysis, the energy of the initial mixed layer velocity field is distributed into vertical normal modes. All modes initially start in-phase in the mixed-layer and their sum is zero in the pycnocline. Thus initially there are currents only in the mixed-layer. Each vertical normal mode is characterized by an *eigenspeed* c_n. The relative contribution, σ_n, of each mode to the initial mixed-layer velocity is determined by the assumption that the initial currents are restricted to the mixed-layer.

Then, using Gill's normalization, we get:

$$\sigma_n = \frac{\int_{H_{mix}}^{0} \phi_n(z)\,dz}{\int_{H}^{0} \phi_n^2(z)\,dz} \qquad (10)$$

where H is the ocean depth, and $\phi_n(z)$ is the non-dimensional eigenfunction defining the shape of each mode. For constant N, $\sigma_1 \approx 2\ H_{mix} / H$. For a more typical, exponential-like stratification profile, we can approximate σ_1 by $\sigma_1 \approx (10\ H_{mix}) / H$. For a typical H = 4000 m, σ_1 may vary from 0.05 to 0.37. Gill has showed that σ_n represents not only the relative contribution of each mode to the initial mixed-layer velocity, but also the fraction of the mode's contribution to the energy of the whole water column. It can also be shown that the contribution of each mode to the energy of the mixed-layer is $\sigma_1(2-\sigma_1)$.

Gill's model is two-dimensional (depth and meridional), but here we will include the zonal direction following the analysis in chapter II. Each baroclinic mode follows the dispersion relation

$$\omega_n^2 = f_0^2 + c_n^2(k^2 + l^2) \qquad (11)$$

where ω_n the frequency of each mode, and k, l the zonal and meridional wavenumbers respectively. The lower the baroclinic mode, the higher its eigenspeed c_n and frequency.

As each mode has a different frequency and all modes start in phase in the mixed-layer, eventually the first mode will become out-of-phase with the higher modes (which rotate very near f_0) in the mixed-layer, and in-phase in the pycnocline. The frequency of the first mode is greater than the very high modes by

$$\omega_1 - f_0 \propto \frac{c_1^2(k^2+l^2)}{f_0} \tag{12}$$

and a phase difference of π in the mixed-layer develops in time

$$t_1 = \frac{2\pi f_0}{c_n^2(k^2+l^2)} \tag{13}$$

Hence, in time t_1 mode 1 interferes destructively with the other modes in the mixed-layer, reducing the velocity by a factor of $1\text{-}2\sigma_1$, and the energy by $(1\text{-}2\sigma_1)^2$ of the initial value (Gill, 1984). So, for H = 4000 m, and H_{mix} = 20 to 150 m, the mixed-layer energy will decay from 0.81 to 0.07 of its initial value in t_1.

One drawback of this analysis by Gill (1984) is that the atmospheric scales are generally many times larger than the baroclinic Rossby radius. The horizontal scales of observed near-inertial waves are often many times smaller than the scales of the forcing. To explain this behavior, D'Asaro (1989) showed that on a β-plane the meridional wavenumber of a freely propagating near-inertial wave will follow

$$l = l_0 - \beta t \tag{14}$$

where l_0 the initial wavenumber set by the atmospheric forcing and $\beta \equiv df/dy$, the rate of change of the Coriolis parameter with latitude. The above relation can be easily derived by ray theory (see chapter II) and explains the equatorward refraction and increase of wavenumber displayed by near-inertial waves (Anderson and Gill, 1983). In chapter II, we incorporated (13) in our analysis of a three-dimensional, β-plane model, and showed that it can be used reliably in (12) to estimate time-scales of energy exchange between the mixed-layer and the pycnocline. Therefore, the time-scale for mixed-layer energy decay due to the first mode can be written from (12) and (13) as:

$$t_1 = \frac{2\pi f_0}{c_1^2[k_0^2 + (l_0 - \beta t_1)^2]} \qquad (15)$$

As showed in chapter II, the smallest positive real root of (14) defines the time-scale for the first energy exchange between mixed-layer and pycnocline due to the interference of mode 1 with high modes.

IV.5. Modification of the friction coefficient

Since mode 1 often makes a dominant contribution to the mixed-layer velocity, we choose t_1 to parameterize the decay time scale. We modify the constant friction coefficient r of the slab model to produce a decay time scale compatible with predictions on a β-plane for energy flux to the deep ocean and pycnocline by near-inertial internal gravity waves. To make the decay time scale in the slab model (r^{-1}) comparable to the time-scale for inertial pumping t_1 on a β-plane (14) , we simply replace r by r', defined by

$$r'(t) \equiv \frac{1}{t_1} = \frac{c_1^2[k_0^2 + (l_0 - \beta t)^2]}{2\pi f_0} \tag{16}$$

Note that r' as defined by (15), is no longer constant, but rather a quadratic function of time. Assuming no energy flux from the wind, the energy equation (9) becomes

$$\frac{dE}{dt} = -2r'(t)E \tag{17}$$

which has the solution

$$E(t) = E(0)e^{-2\int_0^t r'(t')dt'} \tag{18}$$

By defining

$$R(t) \equiv \int_0^t r'(t')dt' \tag{19}$$

we find

$$E(t) = E(0)\, e^{-2R(t)} \tag{20}$$

where

$$R(t) = \frac{c_1^2}{2\pi f_0}\left[(k_0^2 + l_0^2)t - l_0 \beta t^2 + \frac{\beta^2}{3} t^3\right] \tag{21}$$

It is useful to define a complex phase $\Omega(t) \equiv r'(t) + if_0 t$. The solution (6) then becomes

$$Z(t) = Z(0)e^{-\Omega(t)} + \int_0^t \frac{T(t')}{H_{mix}(t')} e^{-\Omega(t-t')} dt' \tag{22}$$

We can easily retrieve the Pollard-Millard solution by replacing $\Omega(t)$ by $\omega t = (r+if_0)t$, where r, f_0 are constants. Because the newly defined $\Omega(t)$ is a complicated function of time, it is not possible to retrieve separate analytic expressions for directly forced and near-inertial waves, as was done in (8).

IV.6. Comparison of impulse responses of r and r´(t)

The decay of mixed-layer energy generated by an impulse wind is shown in Fig. IV.1. The decay has been calculated for a constant r = (4 days)$^{-1}$ and r´(t) for l_0 = +0.005 km^{-1}, 0 km^{-1}, -0.005 km^{-1}. All calculations involving r´(t) were done using k_0 = 0 and c_1 = 2.6 m s^{-1} at a latitude of 50^0. The value of c_1 is typical for open ocean mid-latitude stratification profiles (see chapter II).

The decay based on r´(t) is no longer exponential, but has a bell-like shape. The energy remains in the mixed-layer longer if the propagation of the initial oscillations were northward, shorter if the propagation were southward. The effect of the new response function can affect not only to the decay of mixed-layer oscillations, but also to their generation; this can be deduced by (9) by assuming subsequent wind-forcings in shorter time than 10 days. If the additional forcing induces oscillations in-phase with the pre-existing, we have increased energy flux into the mixed-layer by (9). If the opposite happens, the wind can extract energy from the mixed-layer. An exponential decay of the mixed-layer energy would greatly reduce the effect of consecutive forcings, by underestimating the amplitude of the pre-existing mixed-layer currents.

IV.7. Comparison with a numerical model on a β-plane

IV.7.*a. Comparison utilizing (15)*

In order to assess the performance of our parameterization (20) and its use in a slab model (21), we compare the mixed layer's energy decay expected by (19) with the decay predicted by a numerical model that accurately describes linear inertial pumping, developed in chapter II. We compare the decay expected by the slab-model with the full water column model runs, for various mixed-layer depths and northern extents L_N of the initial conditions (Fig. IV.2). Note that r´(t), as defined by (15), is not an explicit function of H_{mix} or the horizontal northern extent L_N of the initial conditions. There is only a very small variation of c_1, from 2.3 to 2.8 m s^{-1} for the shallowest to the deepest mixed-layer cases respectively. Thus, in Fig. IV.2, the decay of the mixed-layer energy based on the slab model is essentially the same for all cases. For both slab and numerical model we have used $k_0 = l_0 = 0$ at a latitude of 50^0, for all cases. As a sensitivity test, slab-model predictions for an r´ reduced by a factor of $(2\pi)^{-1}$ are also shown.

Figure IV.2 shows some variation of the numerical model results for different values of L_N. We showed that the phenomenon of *inertial beating* (section 3; chapter II.3) will occur when the northern extent L_N of the initial conditions is so large that the low modes propagating from high latitudes, develop a phase difference of π with the native high modes before they have propagated away. If L_N is too small, the process that dominates the transfer of energy vertically is not modal interference, but rather horizontal departure of the modes. Note that for the parameters used in Fig. IV.2, L_N shorter than 250 km would result in faster decay of mixed-layer energy. However, in that case, an initial wavenumber $l_0 = 0$ would not be appropriate, and an equivalent higher wavenumber should be used to describe the fast change of initial conditions with latitude. A high, southward meridional wavenumber would also cause the slab model prediction to be shorter (Fig. IV.1).

Fig. IV.2 also reveals that the evolution of the mixed-layer energy decay in the numerical model is sensitive to H_{mix}. This is due to the differences in the relative contribution of each mode σ_n (section 3); the propagation speeds and frequencies of the modes are only slightly affected (chapter II.4c). In deep mixed-layer cases, modes 1 and 2 contain as much as 60 % of the velocity field, while for shallow mixed-layers the contribution may be only 25 %.

Hence the differences between slab and numerical models are not sensitive to L_N variations, but are dependent on H_{mix}. The slab-model predictions underestimate the energy decay for deep mixed layers, while slightly overestimate it for shallow mixed-layers. For a 50 m mixed layer, the slab-model agrees well with predictions for all northern extents L_N > 250 km.

IV.7.*b. Accounting for the effect of mixed-layer depth*

To account for variations in H_{mix}, we fine-tune the parameter r′(t). Although the time-scale t_1 is not very different for varying H_{mix}, the amount of energy that leaves the mixed-layer at that time is larger for deep mixed layers. Hence, we modify the decay time-scale in order to account for the relative magnitude of the low modes, specifically σ_1. Note that the expected change in r′(t) over the range of H_{mix} will be a factor of 10 at most (Fig. IV.2), with the agreement seeming the best near H_{mix} = 50 m. We chose to normalize r′(t) by the ratio H_{mix}/50 m. The effect would be delaying the decay for shallower mixed-layers and accelerating it for deeper mixed-layers; thus, a new parameterization for r′ will be:

$$r'(t) = \left(\frac{H_{mix}}{50\,m}\right)\frac{c_1^2}{2\pi f_0}\left[(k_0^2 + (l_0 - \beta t)^2\right] \qquad (23)$$

The energy decay estimated using the new parameterization (23) is compared with the numerical model in Fig. IV.3; the dependence on mixed-layer depth has been successfully modeled.

IV.8. Comparison with observations

In order to further assess the performance of the proposed parameterization of r′(t), we compare simulated currents with observations. The OCEAN-STORMS experiment was held in the N.E. Pacific Ocean from August 1987 to July 1988. Observations of the oceanic response to strong atmospheric forcing was made with a variety of instruments. A subsurface mooring was deployed at 47^0 25.4′ N, 139^0 17.8′ W, with a series of current meters extending from 60 to 4000 m depth. Of special interest to this paper is the current meter located at 60 m, that recorded the mixed-layer oscillations from mid-November 1987 to the beginning of May of 1988, when the mixed-layer extended deeper than 60 m. An Aanderaa TR-1 thermistor chain, located on a mooring about 55 km to the west, provided hourly measurements of temperature between the depths of 9 and 109 m, at intervals of 10 m. We used the thermistor chain measurements to monitor the mixed-layer depth as it evolved in time. A time-series of wind speed at a height of 4 m was recorded by an anemometer positioned on a surface mooring 17 km to the north. The wind speed was converted to surface wind-stress assuming neutral stratification for the lower part of the atmosphere (Smith, 1988).

The observed and modeled near-inertial mixed-layer currents are shown in Fig. IV.4. Both observed and modeled time-series were complex demodulated around a frequency of 0.0625 cph using a boxcar window. The phase estimates were backrotated so that constant phase in time suggests a perfect inertial oscillation.

The slab model (21) was forced by the observed time series of wind-stress and mixed layer depth. The modeled response for two values of r = constant of (4 days)$^{-1}$ and (15 days)$^{-1}$ is shown in Fig. IV.4a. The response of the model using the new time-dependent parameterizations, with and without the H_{mix} dependence is shown in Fig. IV.4.b. In the time-dependent r′(t) cases, we assumed k_0(t), l_0(t) = 0.

The currents modeled using the new parameterizations are in a much better agreement with the observed current at 60 m than the current modeled using a constant friction parameter r. This can be seen especially immediately after a major forcing event, such as December 3, January 15, March 5; the modeled magnitudes for r constant are significantly lower than the observed (Fig. IV.4a). We attribute the improvement to the better agreement of the mixed-layer kinetic energy decay using r´(t) with inertial pumping theory (Fig. IV.2). Equation (9) shows that the energy flux from the wind to the mixed-layer is given by $\vec{\tau}_s \cdot \vec{u}$, where $\vec{u}$ is the preexisting mixed-layer current from all earlier forcings. For a constant r coefficient, the pre-existing currents have been decaying exponentially in time; for the time-varying r´, the decay is bell-shaped (Fig. IV.1). The result of the exponential decay of $\vec{u}$ for constant r, is that the time that $\vec{\tau}_s$ can resonate with large $\vec{u}$ values is greatly shortened, thus underestimating the energy flux into the ocean.

There is no significant difference between the runs of the new parameterization with and without H_{mix}; the model does not seem to be very sensitive to the fine-tuning we performed in (23).

We used complex correlations (Kundu, 1976) to quantify the agreement between observations and modelled data. The correlations were calculated on hourly data; we also estimated the correlation on the demodulated estimates. The complex correlation of the unfiltered series gave a coefficient of 0.79 for the model results using r´(t), with a phase of ~15^0; the corresponding results for both the constant r runs displayed in Fig. IV.4a were 0.72-0.73 and 12-19^0. The correlation of the filtered series was improved: the correlation coefficient had a 0.88 amplitude and ~-16^0 phase for the model runs using r´(t) and r´(t, H_{mix}), while the respective values were ~0.81 and from -13^0 to -21^0 for the constant r model runs. The phase signifies the counterclockwise angle that the modeled data lead observations. The higher correlation of the filtered data can be attributed to the extraction of non-inertial motions from the current-meter record. The correlation phase of near 15^0 is consistent with the rotation of an inertial oscillation in about 40 minutes.

IV.9. Summary and Discussion

We replaced the constant Rayleigh friction coefficient used in the traditional slab models with a time-dependent one. The modification was based on the assumption that inertial pumping is the main contributor to the decay of mixed-layer near-inertial kinetic energy.

The modification was tested and fine-tuned by comparison to a numerical model, describing the inertial pumping process. The new parameterization agrees with the numerical model for various wavenumbers and horizontal extents of the initial mixed-layer inertial oscillations, and can be fine-tuned to account for varying mixed-layer depths.

We assessed the new parameterization by comparing slab-model runs with data from the OCEAN-STORMS experiment. The agreement was very good; the success of the new parameterization is enhanced by the fact that, contrary to the constant body friction coefficient method, it does not require any kind of tuning or fitting with data. Fine-tuning to account for varying H_{mix} requires some amount of fitting, but the first order estimate of r´does not.

The better agreement using the new parameterization suggests that the major mechanism responsible for the decay of mixed-layer horizontal kinetic energy during the OCEAN-STORMS experiment was inertial pumping.

The fact that the model runs with $k_0 = l_0 = 0$ suggest that the majority of the forcing fronts during the experiment were of large horizontal scale, or that the model is not very sensitive to small horizontal wavenumber variations.

The new parameterization describes one possible process of extracting near-inertial kinetic energy from the mixed-layer, the process of inertial pumping. The traditional, constant r parameterization is more compatible with another possible sink of energy, that is through turbulent stresses at the base of the mixed-layer. We ran the slab-model with both parameterizations to propose that inertial pumping probable the dominant process of mixed layer kinetic energy decay. Similar use of the model

in other data sets could reveal otherwise. One possible area that we don't expect inertial pumping to be the dominant mechanism of mixed-layer inertial oscillations decay is the high latitudes. In chapter II we showed that the expected time-scales of decay due to inertial pumping grow very large near the arctic circles. That could leave other candidates for effective sinks of mixed-layer energy: Besides the mechanisms already described above, there are non-linear transfers of energy to higher internal wave frequency bands (Broutman and Young, 1986, Flatté et al., 1985, Henyey et al., 1986) as well as linear forcing of high-frequency and wavenumber internal waves (Bell, 1978). A possible different parameterization of the slab model for every process might provide a tool for diagnosing the dominant processes of mixed-layer inertial kinetic energy at various circumstances and areas of the world ocean.

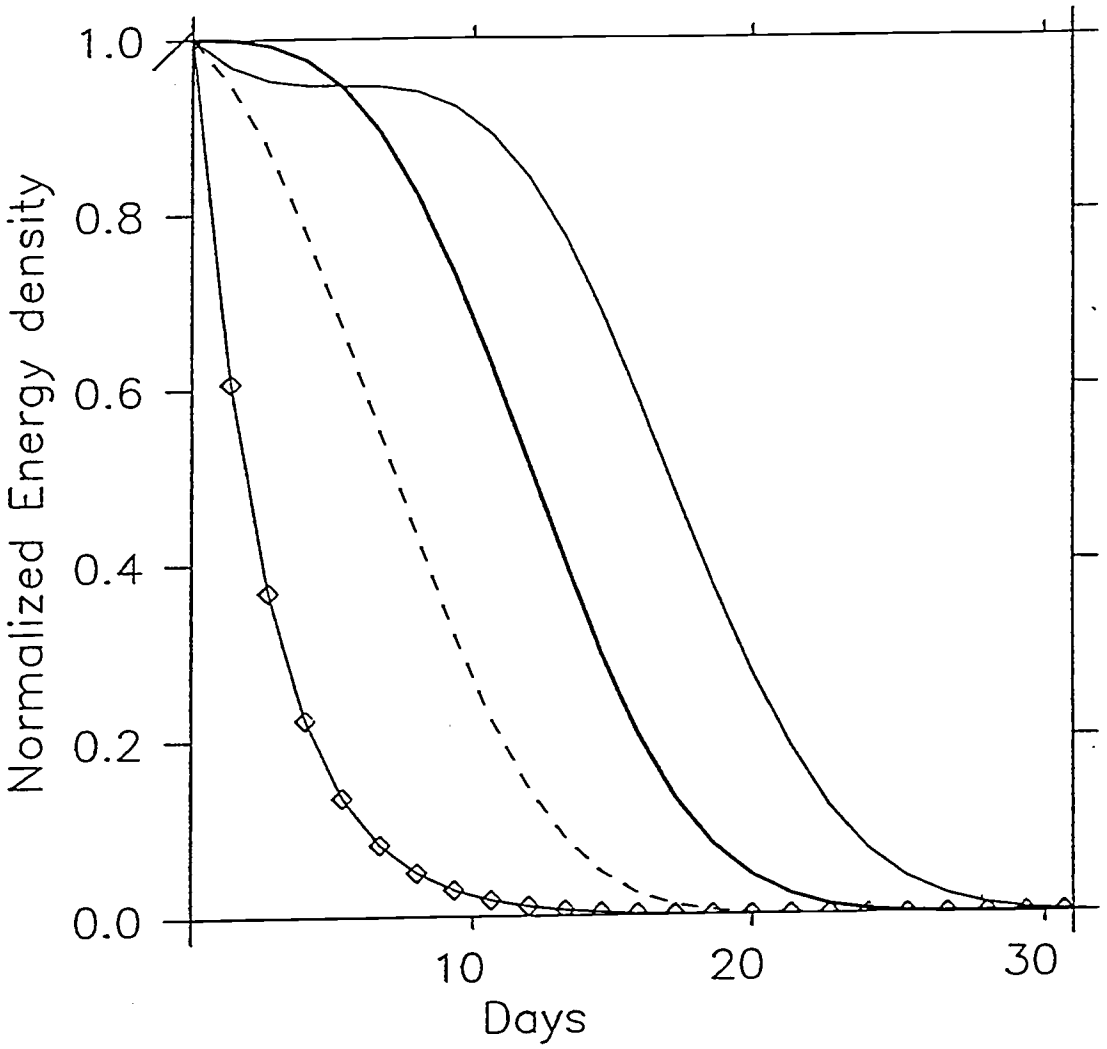

Fig. IV.1 : Comparison of mixed-layer near-inertial horizontal kinetic energy decay using r = (4 days)$^{-1}$ (dotted line, ◊—◊—◊); r′ (t, l_0 = (+0.005 km)$^{-1}$) (light line); r′(t, l_0 = 0 km^{-1}) (heavy line) and r′(t, l_0 = (-0.005 km)$^{-1}$) (dashed line). All calculations involving r′(t) were done using $k_0 = 0$ and $c_1 = 2.6$ m s^{-1} at a latitude of 50^0.

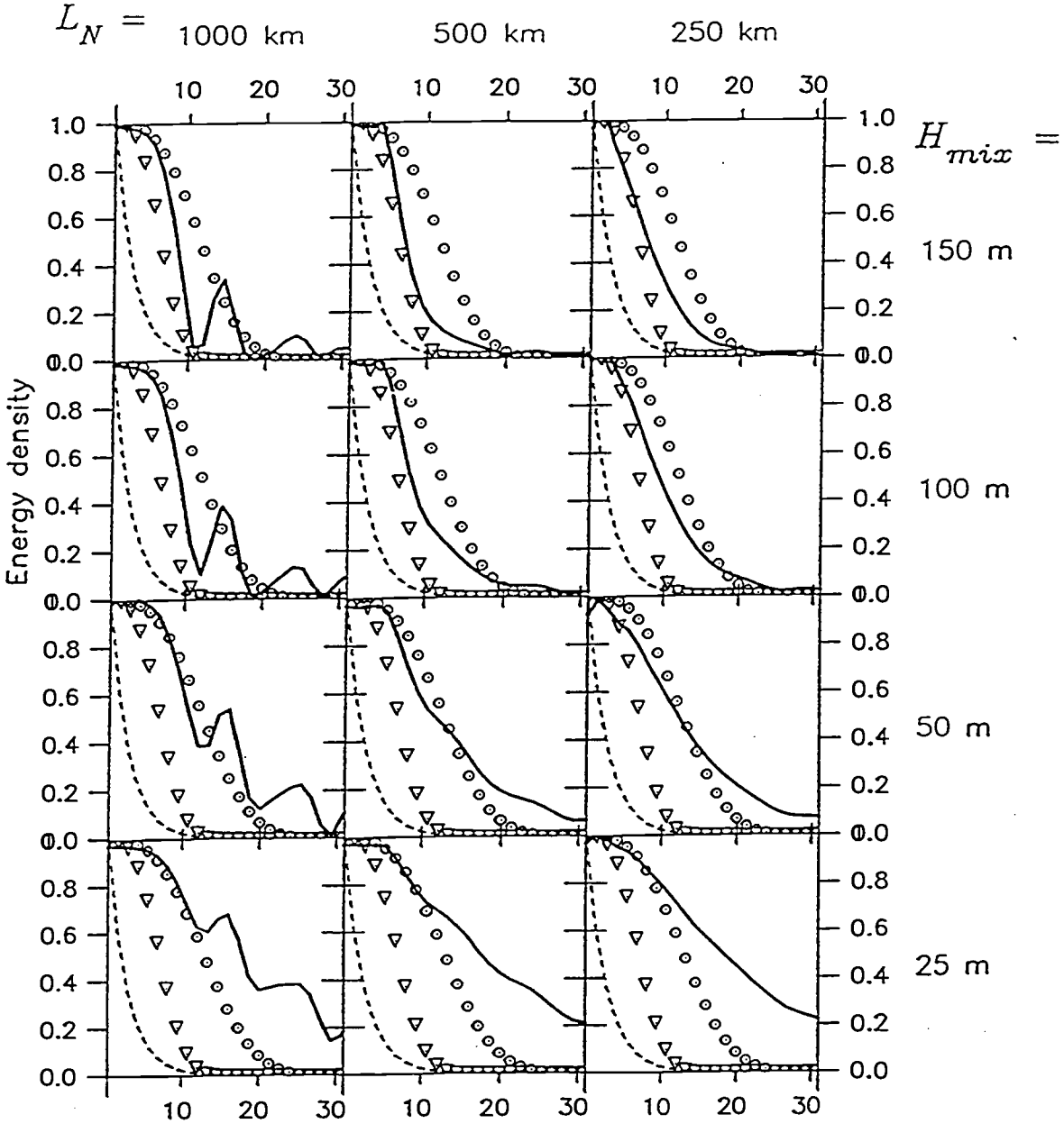

Fig. IV.2 : Comparison of slab-model runs for r´(t) defined by (16) (dotted line, ⊙ ⊙ ⊙ ⊙), an r´(t) smaller than (20) by 2π (dotted line, ▽ ▽ ▽ ▽), r = (4 days)$^{-1}$ (dashed line), and full water column model runs (heavy line). In the full model runs, we vary northern extent L_N (by column, left to right, 1000, 500, and 250 km) and mixed-layer depth H_{mix} (by row, top to bottom 150, 100, 50 and 25 m). For both models, we have used $k_0 = l_0 = 0$.

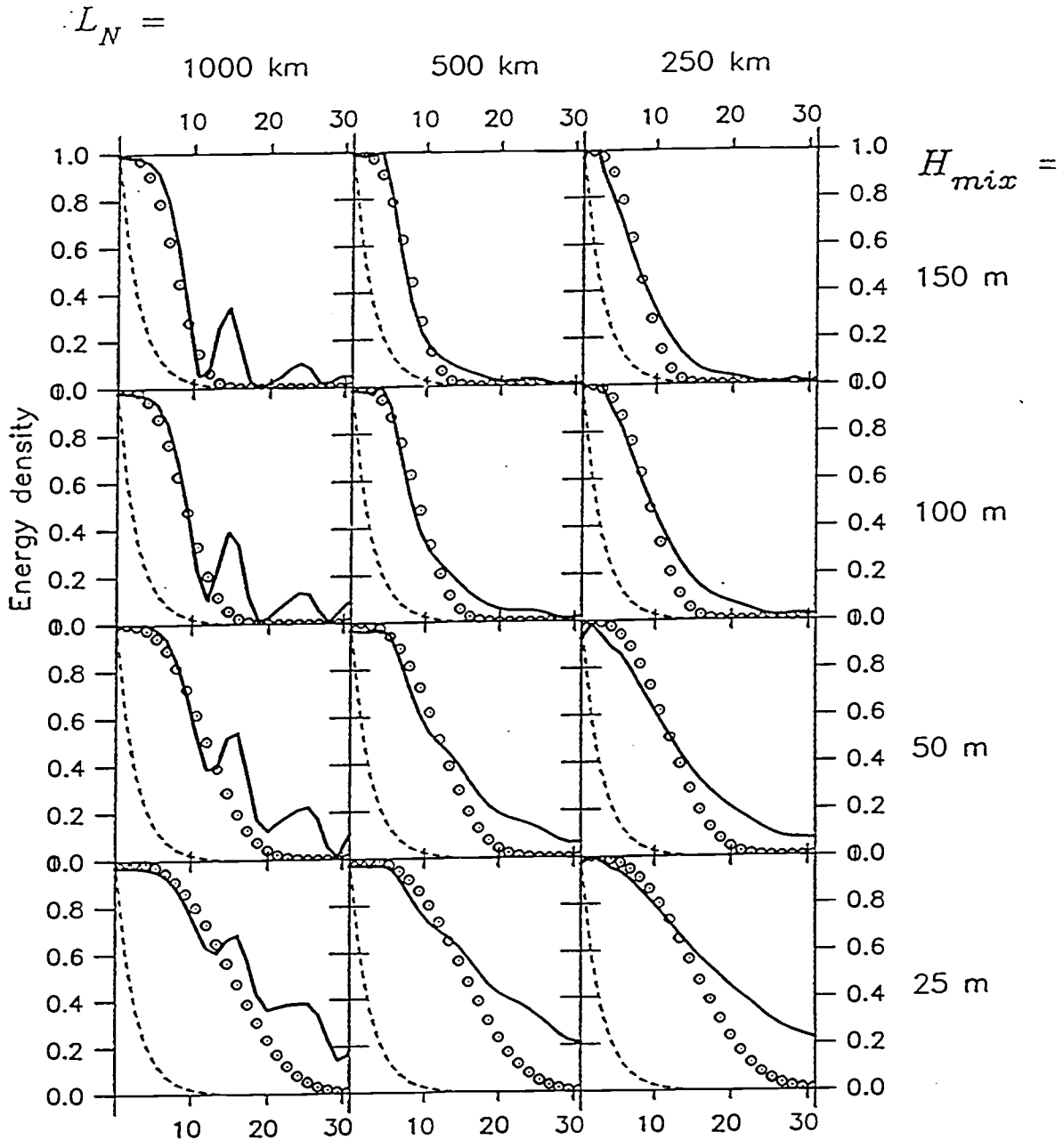

Fig. IV.3 : Comparison of slab-model runs for r′(t) defined by (23) (dotted line, ⊙ ⊙ ⊙ ⊙), , r = (4 days)$^{-1}$ (dashed line), and full water column model runs (heavy line). In the full model runs, we vary northern extent L_N and mixed-layer depth H_{mix} in the same way as in Fig. IV.2. For both models, we have used $k_0 = l_0 = 0$.

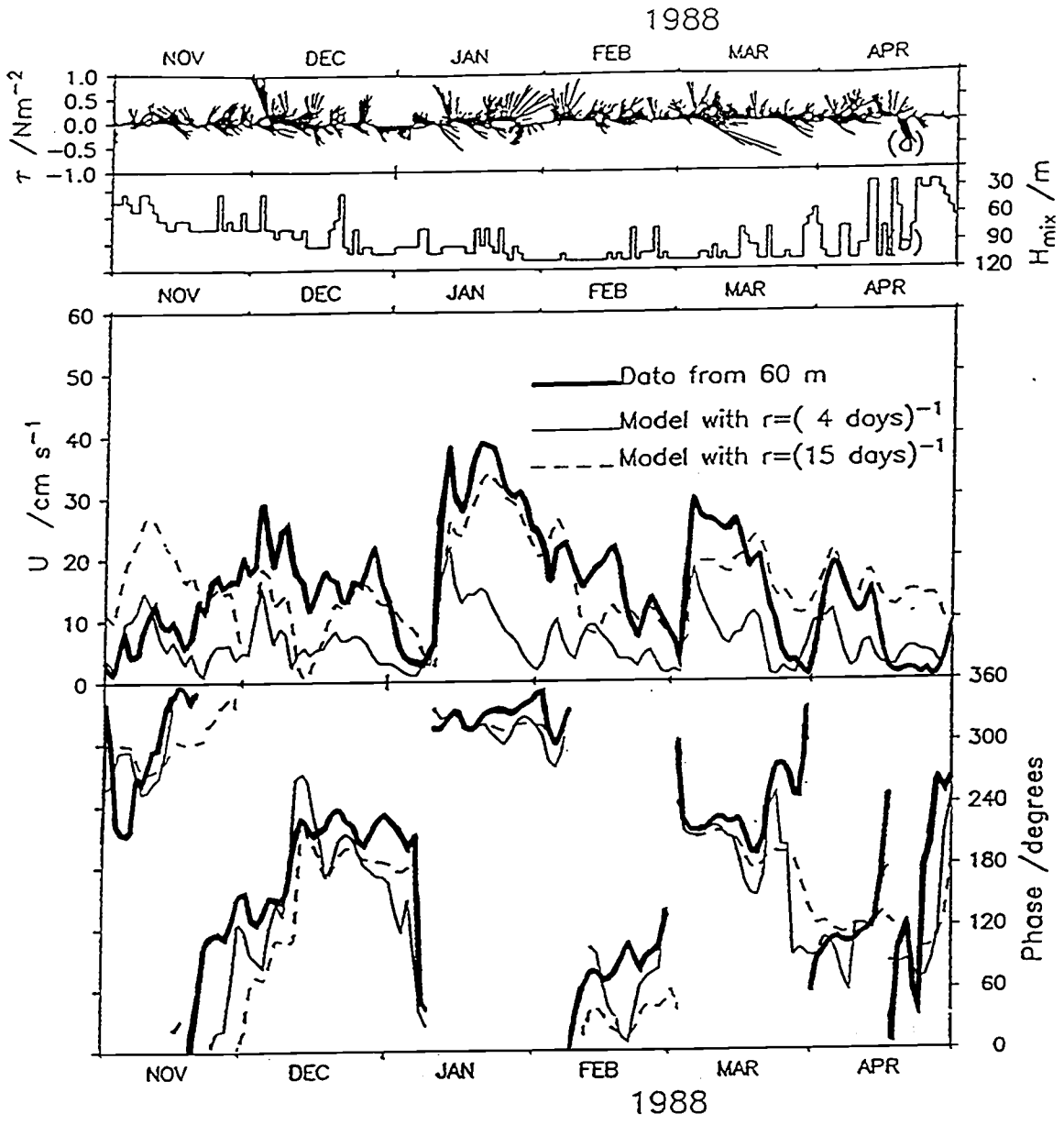

Fig. IV.4a : (a) Time series of wind-stress at site C0; (b) mixed-layer depth , and (c) bottom panel: Comparison of observed inertial oscillations at 60 m (thick line) with slab-model runs for r = (4 days)$^{-1}$ (light line), and r = (15 days)$^{-1}$ (dashed line). The mixed-layer is deeper than 60 m between mid-November and mid-April.

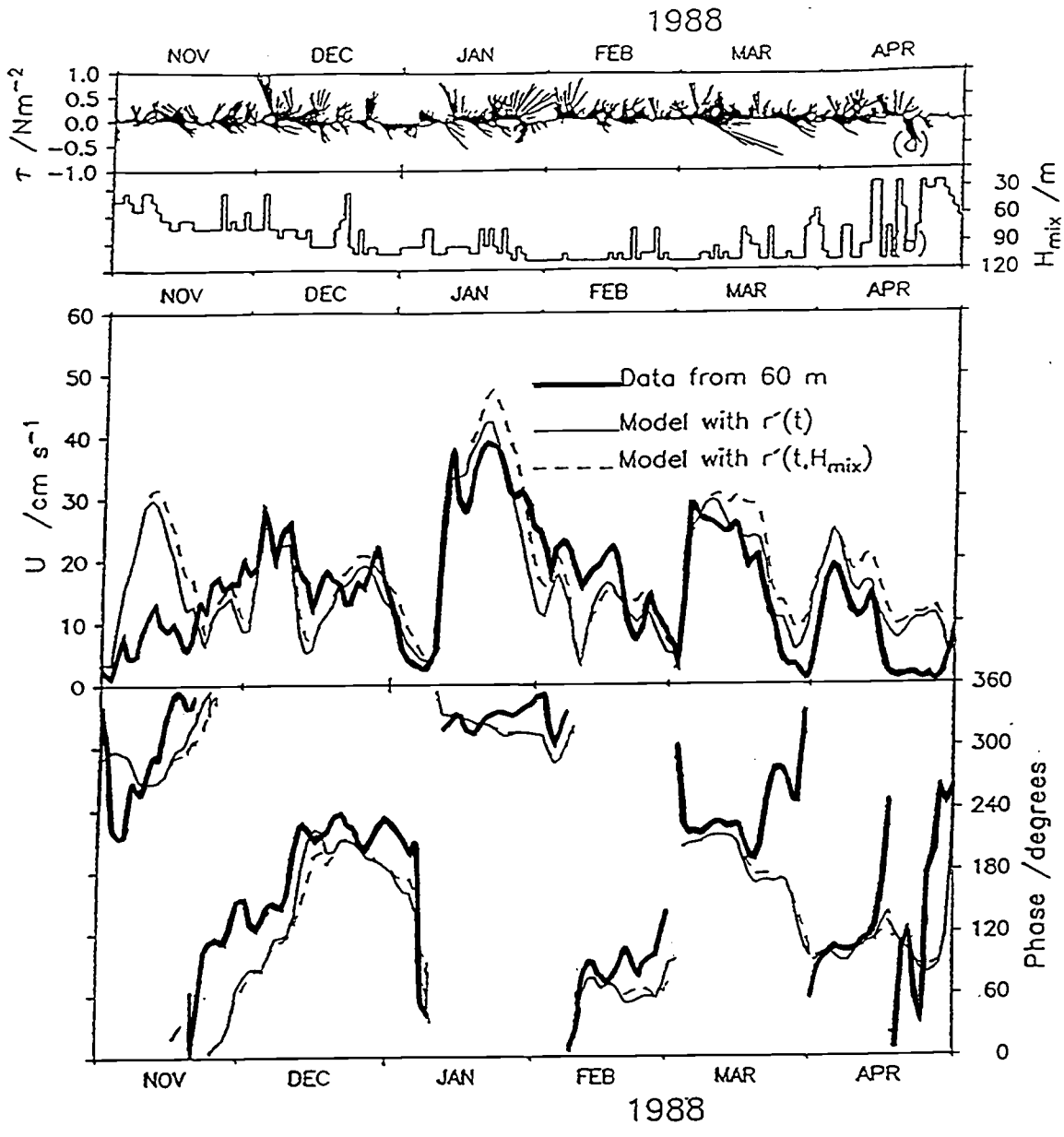

Fig. IV.4b : (a) Time series of wind-stress at site C0; (b) mixed-layer depth , and (c) bottom panel: Comparison of observed inertial oscillations at 60 m (thick line) with slab-model runs for r′(t) as defined by (16) (light line), and r′(t) as defined by (23) (dashed line). The mixed-layer is deeper than 60 m between mid-November and mid-April.

IV.10. References

Bell, T., 1978: Radiation damping of inertial oscillations in the upper ocean. *J. Fluid Mech.*, **88**, 2, 289-308.

Broutman, D. and W. R. Young, 1986: On the interaction of small-scale oceanic internal waves and near-inertial waves. *J. Fluid Mech,*. **166**, 341-358.

D' Asaro, E., 1985: Upper Ocean Temperature Structure, Inertial Currents, and Richardson Numbers Observed During Strong Meteorological Forcing. *J. Phys. Oceanogr.*, **15**, 943-962.

D'Asaro, E., 1989: The Decay of Wind-Forced Mixed Layer Inertial Oscillations Due to the Beta Effect. *J. Geophys. Res.*, **94**, 2045-2056.

Day, C. G. and F. Webster, 1965: Some current measurements in the Sargasso Sea. *Deep Sea Research*, **12**, 805-814.

Eriksen, C. C., 1988: On Wind Forcing and Observed Oceanic Wave Spectra. *J. Geophys. Res.*, **93**, C5, 4985-4992.

Flatté, S. M., F. S. Henyey and J. A. Wright, 1985: Eikonal calculations of short-wavelength internal-wave spectra. *J. Geophys. Res.*, **90**, 7265-7272.

Gill, A. E., 1984: On the Behavior of Internal Waves in the Wakes of Storms. *J. Phys. Oceanogr.*, **14**, 1129-1151.

Henyey, F. S., J. A. Wright, and S. M. Flatté. , 1986: Energy and Action Flow Through the Internal Wave Field: an Eikonal Approach. *J. Geophys. Res.*, **91**, C7, 8487-8495.

Hunkins, K., 1967: Inertial Oscillations of Fletcher's Ice Island (T-3). *J. Geophys. Res.*, **72**, 1165-1174.

Kundu, P. K., 1976: An Analysis of Inertial Oscillations Observed Near Oregon Coast. *J. Phys. Oceanogr.*, **6**, 879-893.

Lacombe, H., and J. Gonella, 1964: Oscillations d'inertie des masses d' eau en Mediterranée occidentale. *C. r. hebd. Séanc. Acad. Sci.,Paris,* 259, 2487-2490.

Paduan, J., R. A. de Szoeke, and R. A Weller, 1989: Inertial Oscillations in the Upper Ocean During the Mixed Layer Dynamics of the Upper Ocean Experiment. *J. Geophys. Res.*, **94**, C4, 4835-4842.

Pollard, R. T. and R. C. Millard, 1970: Comparison Between Observed and Simulated Wind-Generated Inertial Oscillations. *Deep Sea Research*, **17**, 813-821.

Pollard, R. T., 1980: Properties of near-surface inertial oscillations. *J. Phys. Oceanogr.*, **10**, 385-398.

Smith, S. D., 1988: Coefficients for Sea Surface Wind Stress, Heat Flux, and Wind Profiles as a Function of Wind Speed and Temperature. *J. Geophys. Res.*, **93**, C12, 15,467-15,472.

Webster F., 1968: Observations of inertial-period motions in the deep-sea. *Rev. Geophys.*, **6**, 473-490.

V. GENERAL CONCLUSIONS

In chapter II of this study we address the problem of vertical and horizontal radiation of near-inertial internal gravity waves from the mixed-layer. We assume that the initial currents are concentrated in the mixed-layer and have a horizontal structure set by the horizontal advection of a large atmospheric front over the ocean surface. The radiation of the wavefield is assumed consistent with linear, inviscid dynamics on a β-plane (section II.2). The wave evolution is calculated using a numerical model. The main conclusions from this chapter are:

- The model results agree with predictions based on analytical linear wave theory on a β-plane. The association of the numerical model and analytical theory permits predictions of many features of the wave evolution without the need to run the numerical model.
- The horizontal propagation of modes at distinct speeds causes vertical propagation of energy through two mechanisms: Modal interference and modal departure.
- When the initial mixed-layer currents have a large horizontal extent ($L_N > 500$ km), the vertical propagation of energy is caused by the interference of modes characterized by different frequencies (inertial beating). If t_n represents the time of inertial beating of mode n, the beating of mode 1 at t_1 marks the first time of effective vertical propagation of energy. The value of t_n depends greatly on the initial wavenumber of the currents in the mixed layer. The β-effect causes a great difference in t_n between an initially northward or southward propagating front--inertial beating occurs sooner for a southward going front (Fig. II.3a).
- For initial conditions of short horizontal extent ($L_N < 250$ km), the dominant cause of vertical propagation of energy is the successive departure of modes from the generation area. To characterize the time scales of this process, we have defined τ_n^{NS} and τ_n^{EW} to represent the times when mode n leaves $y = 0$ due to horizontal propagation. These time scales are a function of the

horizontal extent of the storm as well as the initial wavenumber (Fig. II.3b).

- Beside the initial wavenumber all the time scales are affected by the modal eigenspeeds c_n and the value of f_0 which are functions of stratification and latitude. We estimated that the evolution of the near-inertial waves varies from a few days at low latitudes to several weeks at high (Fig. II.11).
- In addition to the time scales the modal decomposition of the wavefield is needed to determine the quantitative effect of the inertial beating and horizontal propagation. For example, if mode 1 is a large fraction of the total energy (σ_1 large), then the vertical propagation at t_1 will be significant. The modal composition is set by the stratification. The deeper the mixed layer the larger the mode 1 contribution. Hence the energy transfers at times t_1 and τ_1^{NS} are more dramatic for deeper mixed layer (Fig. II.8).
- From the two processes described by the model, it is modal interference that can be associated with the frequently observed intermittency of the near-inertial waves. When the modal departure is the dominant mechanism of downward propagation of energy, there is no intermittency ("beating") observed (Fig. II.8). The intermittency can also be traced in the currents' phase, as short periods of sub-inertial frequencies, coincident with amplitude minima (Fig. II.9).

The three-dimensional model developed in this chapter provided us with confidence of the ability of analytical theory to describe the evolution of the inertial wavefield generated by a large, fast storm propagating at any direction. However, in order to assess the validity of either model or theory, a comparison with oceanic observations is needed. The validity of the present analysis can also be tested by the development of a simple model forced by wind-stress, where the decay of the mixed-layer oscillations is consistent with the predictions developed here. Chapters III and IV of this thesis were both steps to that direction.

In Chapter III we compared three relatively distinct events of inertial current

generation during the OCEAN-STORMS experiment with results from a linear numerical model. We focused our attention on the characteristic time-scales of energy exchange between the mixed-layer and the pycnocline.

The observed near-inertial response of the ocean demonstrated some characteristics common to all cases, and some differences among them:

- The time-scale for the energy propagation from the mixed-layer to the pycnocline, defined as the time for E_{PC} to reach its maximum, was 13-15 days for all three events. However, the increase started immediately after the October event, while it was delayed by about a week in the other two events.
- The time for E_{PC} to return to background levels was 13-15 days for the October and March events. The decay of E_{PC} was not clearly defined during January, due to the multiple atmospheric forcing.
- The observed mixed-layer frequencies were 1.00-1.01 f_0 for 14-20 days, then fluctuated between 0.08 f_0 and 1.03 f_0 (January, March) (Fig. III.9a_i,b_i,c_i). No estimates of frequency were available for the mixed-layer in October.
- The waves propagated into the pycnocline as a beam (Fig. III.10a, 11a, 12a). The beam maximum propagated vertically from 60 to 100 m in a week (October); the distance between 100 and 195 m depth was covered by the beam maximum in 11 days in January and 6 days in March.
- The frequencies recorded in the pycnocline are higher inside the 'beam', ranging from 1.03 to 1.05 f_0, at all events. After the beam is gone, the frequencies fall to 1.00-1.02 f_0. The higher frequencies are associated with the vertical propagation of the beam.
- In all three events, the near-inertial waves of the pycnocline develop higher frequencies than the mixed layer currents during the passage of the beam; as a result, vertical phase differences develop that increase in time as the beam propagates vertically. The resulting phase difference after the propagation of the beam between 60 and 195 meters is usually 120 ± 30^0. The phase propagates

upward, consistent with downward propagation of energy.

We compared the observations with both the numerical model and the analytical predictions based on linear theory, developed in chapter II. The main conclusions from the comparison were:

- The overall amount of energy observed radiating from the mixed-layer to the pycnocline, is reproduced by the model. The magnitude of the pycnocline energy, E_{PC}, of the modeled currents, is comparable to the observed E_{PC}, for all three events.
- The changes of the observed pycnocline energy E_{PC} occur near the analytically predicted times t_1 and t_2 (beating of modes 1 and 2 respectively), calculated using our initial wavenumber estimates for each event.
- There is a trend of the model to slightly underestimate the peak of E_{PC} at t_1 and overestimate it at t_2 for the January and March events. This disagreement is greatest during the October event; while the model shows E_{PC} peaking at time t_2, the observed peaks at t_1..
- The features of the energy exchange between mixed-layer and pycnocline for the October and March events suggest that the pumping is due to modal interference and not due to modal departure. Modal departure may be important during January.
- The detailed vertical structure of the observed currents is different than the modeled. The modeled currents do not propagate vertically as a beam, but rather stick to the top 40-50 m of the pycnocline.
- The modeled currents have frequencies ranging from slightly sub-inertial to 1.05 f, and their phase propagates upward, both characteristics of the observed currents. However, the model fails to reproduce the detailed temporal and spatial structure of the phase of the observed currents.

From chapter III, we have learned that while linear dynamics is adequate to estimate characteristic time scales and coarse features of near-inertial waves, we need to include more complicated dynamics to explain the detailed structure of the wave fields.

Finally, in chapter IV, we modified the slab model of generation of mixed-layer inertial oscillations by the wind to account for decay due to inertial pumping on a β-plane. The constant Rayleigh friction coefficient of the traditional slab models was replaced with a time-dependent coefficient, parameterizing internal wave radiation to the pycnocline.. The main conclusions from this chapter are:

- The new parameterization was assessed by comparing slab-model runs with data from the OCEAN-STORMS experiment. The agreement was very good; the success of the new parameterization is enhanced by the fact that, contrary to the constant body friction coefficient method, it does not require any kind of tuning or fitting with data. Fine-tuning to account for varying H_{mix} requires some amount of fitting, but a first-order estimate does not.
- The better agreement using the new parameterization suggests that the major mechanism responsible for the decay of mixed-layer horizontal kinetic energy during the OCEAN-STORMS experiment was inertial pumping.
- The fact that the runs were performed with $k_o = l_o = 0$ suggest that the majority of the forcing fronts during the experiment were of large horizontal scale, or that the model is not very sensitive to small horizontal wavenumber variations.

We believe it is possible to employ the slab model in different areas of the world ocean to identify dominant mechanisms of mixed-layer near-inertial energy decay.

VI. BIBLIOGRAPHY

Anderson, D. L., and A. E. Gill, 1979: Beta Dispersion of Inertial Waves. *J. Geophys. Res.*, **84**, 1836-1842.

Bell, T., 1978: Radiation damping of inertial oscillations in the upper ocean. *J. Fluid Mech.*, **88**, 2, 289-308.

Broutman, D. and W. R. Young, 1986: On the interaction of small-scale oceanic internal waves and near-inertial waves. *J. Fluid Mech,*. **166**, 341-358.

D'Asaro, E., 1985: The Energy Flux From the Wind to Near-Inertial Motions in the Surface Mixed Layer. *J. Phys. Oceanogr.*, **15**,1043-1059.

D'Asaro, E., 1985b: Upper Ocean Temperature Structure, Inertial Currents, and Richardson Numbers Observed During Strong Meteorological Forcing. *J. Phys. Oceanogr.*, **15**, 943-962.

D'Asaro, E., 1989: The Decay of Wind-Forced Mixed Layer Inertial Oscillations Due to the Beta Effect. *J. Geophys. Res.*, **94**, 2045-2056.

D'Asaro, 1993: Analysis of Drifter data from OCEAN-STORMS.*Submitted for publication to J. Phys. Oceanogr.*

Day, C. G. and F. Webster, 1965: Some current measurements in the Sargasso Sea. *Deep Sea Research*, **12**, 805-814.

De Young, B. and C. L. Tang, 1990: Storm-Forced Baroclinic Near-Inertial Currents on the Grand Bank. *J. Phys. Oceanogr.*, **20**, 1725-1741.

Eriksen, C. C., 1988: On Wind Forcing and Observed Oceanic Wave Spectra. *J. Geophys. Res.*, **93**, C5, 4985-4992.

Eriksen, C. C., 1991: Observations of Near-Inertial Internal Waves and Mixing in the Seasonal Thermocline. *'Aha Huliko'a Hawaiian Winter Workshop Proceedings,* University of Hawaii at Manoa, January 15-18, 1991, pp. 71-88.

Fjeldstad, J. E., 1964: Internal waves of tidal origin. Part I. Theory and analysis of observations. *Geophyiske. Publikasjoner*, **XXV**, 5, 1-73.

Flatté, S. M., F. S. Henyey and J. A. Wright, 1985: Eikonal calculations of short-wavelength internal-wave spectra. *J. Geophys. Res.*, **90**, 7265-7272.

Fu, L. L., 1981: Observations and models of inertial waves in the deep ocean. *Rev. Geoph. Space Phys.*, **19**, 191-170

Garrett, C. J. R. and W. H. Munk, 1975: Space-time scales of internal waves: A progress report. *J. Geophys. Res.*, **80**, 291-297.

Gill, A. E., 1984: On the Behavior of Internal Waves in the Wakes of Storms. *J. Phys. Oceanogr.*, **14**, 1129-1151.

Gill, A. E., 1982: Atmosphere-Ocean Dynamics, *Academic Press*, 346-353.

Gonella, J., 1972: A Rotary-Component method for analysing meteorological and oceanographic vector time series. *Deep-Sea Res.*, **19**, 833-846.

Greatbatch, R. J., 1983: On the response of the ocean to a moving storm: The non-linear dynamics. *J. Phys. Oceanogr.*, **13**, pp. 357-367.

Greatbatch, R. J., 1984: On the response of the Ocean to a moving storm: Parameters and Scales. *J. Phys. Oceanogr.*, **14**, pp. 59-78.

Hebert, D., and J. N. Moum, 1993: Decay of a Near-Inertial Wave. *paper submitted to JPO.*

Henyey, F. S., J. A. Wright, and S. M. Flatté. , 1986: Energy and Action Flow Through the Internal Wave Field: an Eikonal Approach. *J. Geophys. Res.,* **91**, C7, 8487-8495.

Higdon, R., L., 1993: Radiation Boundary Conditions for Dispersive Waves. to appear in *SIAM J. Numerical Analysis.*

Hunkins, K., 1967: Inertial Oscillations of Fletcher's Ice Island (T-3). *J. Geophys. Res.*, **72**, 1165-1174.

Krauss, W., 1981: The Erosion of a Thermocline. *J. Phys. Oceanogr.*, **11**, 415-433

Kundu, P. K., 1976: An Analysis of Inertial Oscillations Observed Near Oregon Coast. *J. Phys. Oceanogr.*, **6**, 879-893.

Kundu, P. K., 1984: Generation of Coastal Inertial Oscillations by Time-Varying Wind. *J. Phys. Oceanogr.*, **14**, 1901-1913.

Kundu, P. K., 1986: A Two-Dimensional Model of Inertial Oscillations Generated by a Propagating Wind-Field. *J. Phys. Oceanogr.*, **16**, 1399-1411.

Kundu, P. K., 1992: On Internal Waves Generated by Propagating Wind-Stress. *(Submitted for publication, 30 Sept. 1992).*

Kundu, P. K., and R. E. Thomson, 1985: Inertial Oscillations Due to a Moving Front. *J. Phys. Oceanogr.*, **15**, 1076-1084.

Kunze, E., 1985: Near-Inertial Wave Propagation in Geostrophic Shear. *J. Phys. Oceanogr.*, **15**, 544-565.

Lacombe, H., and J. Gonella, 1964: Oscillations d'inertie des masses d' eau en Mediterranée occidentale. *C. r. hebd. Séanc. Acad. Sci.,Paris,* **259**, 2487-2490.

Leaman, K., 1976: Observations on the vertical polarization and energy flux of near-inertial waves.*J. Phys. Oceanogr.*, **6**, 894-908.

Leaman, K., and T. B. Sanford, 1975: Vertical energy propagation of inertial waves. *J. Geophys. Res.*, **80**, 1975-1978.

Levine, M. D., C. A. Paulson, S. R. Gard, J. Simpkins, V. Zervakis, 1990: Observations from the C1 mooring during OCEAN-STORMS in the N.E. Pacific Ocean, August 1987-June 1988. *Reference 90-3, Data Report 151, Oregon State University*, 18.

Levitus, S., 1982: Climatological Atlas of the World Ocean. *Professional Paper 13*, National Oceanic and Atmospheric Administration, U.S. Department of Commerce, Rockville, Md.

Lighthill, J., 1978: Waves in Fluids. *Cambridge University Press*, 317-325.

Lindsay, R. W. , 1988: Surface Meteorology during Ocean Storms Field Program. *Technical Report, APL-UW TR 8823*, Applied Phusics Laboratory, University of Washington.

Marmorino, G. O., L. J. Rosenblum, and C. L. Trump, 1987: Fine Scale Temperature Variability: The Influence of Near-Inertial Waves. *J. Geophys. Res.*, **92**, C12, 13,049-13,062.

McCreary, J. P., 1981: A Linear Stratified Ocean Model of the Equatorial Undercurrent. *Proc. R. Soc. London*, Ser. A, **62**, 603-373.

Millot and Crépon, 1981: Inertial Oscillations on the Continental Shelf of the Gulf of Lions-Observations and Theory. *J. Phys. Oceanogr.*, **11**, 639-657.

Munk, W, 1981: Internal Waves and Small-Scale Processes. In *Evolution of Phys. Oceanography*, Cambridge, Mass., 264-291.

Newton, I., 1776: Mathematical Principles of Natural Philosophy, translated by R. Thorp, M.A.. *ed. W. Strahan, London. reprinted by Dawsons of Pall Mall, London*, 1969.

Paduan, J., R. A. de Szoeke, and R. A Weller, 1989: Inertial Oscillations in the Upper Ocean During the Mixed Layer Dynamics of the Upper Ocean Experiment. *J. Geophys. Res.*, **94**, C4, 4835-4842.

Perkins, H. T., 1970: Inertial Oscillations in the Meditteranean. *PhD Thesis*, M.I.T.-W.H.O.I.

Pollard, R. T., 1970: On the Generation by Winds of Inertial Waves in the Ocean. *Deep-Sea Res.*, **17**, 795-812.

Pollard, R. T., 1980: Properties of near-surface inertial oscillations. *J. Phys. Oceanogr.*, **10**, 385-398.

Pollard, R. T. and R. C. Millard, 1970: Comparison Between Observed and Simulated Wind-Generated Inertial Oscillations. *Deep Sea Research*, **17**, 813-821.

Price, J. G., 1983: Internal Wave Wake of a Moving Storm. *J. Phys. Oceanogr.*, **13**, 949-965.

Qi, H., 1993: *Personal Communication*

Rubenstein, D. M., 1983: Vertical Dispersion of Inertial Waves in the Upper Ocean. *J. Geophys. Res.*, **88**, 4368-4380.

Saelen, O. H., 1963: Studies in the Norwegian Atlantic Current, Part II. *Geofys. Publr.*, **23**,1-82.

Sanford, T. B., 1975: Observations of the vertical structure of internal waves. *J. Geophys. Res.*, **80**, 3861-3871.

Shay, L., K., and R. L. Elsberry, 1987: Near-Inertial Ocean Current Response to Hurricane Frederic. *J. Phys. Oceanogr.*, **17**, 1249-1269.

Shay, L., K., R. L. Elsberry and P. G. Black, 1989: Vertical Structure of the Ocean Current Response to a Hurricane. *J. Phys. Oceanogr.*, **19**, 649-669.

Smith, S. D., 1988: Coefficients for Sea Surface Wind Stress, Heat Flux, and Wind Profiles as a Function of Wind Speed and Temperature. *J. Geophys. Res.*, **93**, C12, 15,467-15,472.

Tabata, S., L. A. F. Spearing, R. H. Bigham, B. G. Minkley, J. Love, D. Yelland, J. Linguanti, P. M. Kimber, 1988: STP / Hydrographic Observations along Line P, Line R and Associated Lines and in the "OCEAN STORMS" Area: Cruise I - 22 September - 16 October, 1987-- Cruise III -24 November - 9 December, 1987. *Canadian Data Report of Hydrographic and Ocean Sciences,***No 70**, Institute of Ocean Sciences, Department of Fisheries and Oceans, Sidney, B.C. V8L 4B2.

Wang, D. P., 1991: Generation and Propagation of inertial waves in the subtropical front. *J. Mar. Res.*, **49**, 619-633.

Webster F., 1968: Observations of inertial-period motions in the deep-sea. *Rev. Geophys.*, **6**, 473-490.

APPENDIX

Orthogonality and energetics for the modes.

From equations (10) and (11) of chapter II, we can retrieve the orthogonality conditions for the vertical modes of the horizontal and vertical components of velocity respectively. For the horizontal component modes ϕ_n, we get

$$\int_{-H}^{0} \phi_n(z)\,\phi_m(z)\,dz = 0$$

while, for the vertical velocity modes ψ_n we get

$$\int_{-H}^{0} N^2(z)\,\psi_n(z)\,\psi_m(z)\,dz = 0$$

Using the orthogonality conditions for the horizontal velocity, and the initial velocity profile (13) from chapter II, we can retrieve the formula describing the contribution $\sigma_n$of each mode to the initial velocity profile:

$$\sigma_n = \frac{\int_{-H}^{0} S(z)\,\phi_n(z)\,dz}{\int_{-H}^{0} \phi_n^2(z)\,dz} = \frac{H_{mix}}{\int_{-H}^{0} \phi_n^2(z)\,dz}$$

G84 has showed that σ_n also describes the contribution of each mode to the energy of the whole water column. The contribution of each mode to the mixed-layer initial energy however, is given by

$$\bar{\sigma}_n = \left[\sum_{j=1}^{\infty} \sigma_j \phi_j(z)\right]^2 - \left[\sum_{j=1}^{\infty} \sigma_j \phi_j(z)\, \delta(j-n)\right]^2$$
$$= 1 - \left[\sum_{j=1}^{\infty} \sigma_j \delta(j-n)\right]^2 = \sigma_n(2-\sigma_n)$$

since $\phi_j(z) = 1$, for $-H_{mix} < z < 0$. These estimates allow us to calculate the decay of mixed-layer energy due to modal "beating" and compare it to the decay due to modal "departure".

For example, when mode 1 "beats" with the high modes at time t_1, the normalized velocity amplitude in the mixed-layer is $1-2\sigma_1$, and the mixed-layer energy is $(1-2\sigma_1)^2$ (Gill, 1984). On the contrary, if at time τ_1^{NS} or τ_1^{EW} mode 1 leaves the area before beating, the mixed-layer energy becomes $1-\sigma_1(2-\sigma_1)$. Note that the mixed-layer energy decays faster due to modal interference than due to modal departure.